

INTERFACIAL ADHESION OF DENTAL CERAMIC-RESIN SYSTEMS

By

ALVARO DELLA BONA

A DISSERTATION PRESENTED TO THE GRADUATE SCHOOL
OF THE UNIVERSITY OF FLORIDA IN PARTIAL FULFILLMENT
OF THE REQUIREMENTS FOR THE DEGREE OF
DOCTOR OF PHILOSOPHY

UNIVERSITY OF FLORIDA

2001

Copyright 2001

by

Alvaro Della Bona

To my loving family, Carla and Izadora, with particular appreciation to my lovely
parents, Carlos and Zelima Pasetti Della Bona

ACKNOWLEDGMENTS

I wish to express my sincere gratitude to the faculty and staff in Dental Biomaterials and Materials Science and Engineering who have assisted me on my journey through the Ph.D. program.

My most sincere thanks go to my advisors, Dr. Kenneth J. Anusavice and Dr. John J. Mecholsky Jr. They provided me numerous hours of guidance, wise advice, and thought-provoking discussion. They have always had my very best interest at heart, supporting and encouraging me throughout my graduate studies. Their enthusiasm, honesty, research ethics, high quality of knowledge, supervising ability, and dedication to education and research will inspire my conduct for life. They will always have my admiration, respect, and friendship.

My best regards also go to the other members of my committee: Dr. Chiayi Shen, Dr. Robert DeHoff, Dr. Mark C. Yang, and Dr. Paul DeHoff, all of whom contributed to this work.

I am very grateful to the faculty and staff of the Department of Dental Biomaterials for all their help and assistance. My special thanks go for Dr. Chiayi Shen, Dr. Karl Söderholm, and Ms. Allyson Barrett for their support and friendship. Very special thanks go to Mr. Robert Ben Lee for his assistance and technical support.

I would like to express my gratitude to Dr. Luisa Amelia Dempere and Mr. Wayne Acree for their assistance at the Major Analytical Instrumentation Center.

I also would like to thank Dr. James B. Summitt at the University of Texas Health Science Center at San Antonio, Dr. Richard van Noort at the University of Sheffield, England, and Dr. James A. A. Hood at Otago University, New Zealand, my advisors from previous graduate programs. Their guidance and contributions have influenced the development of both my professional career and personal life.

I want to thank my fellow graduate students, especially Tom Hill, for their help and friendship. It is my wish that they achieve all the success they deserve.

I am grateful to my friends Allyson, Tom, Nicola, Bill, Kallaya, Soraya, Don, Ed, and their families, for the friendship and support. Family love is very important for the ones living way from home.

Finally, all my love and dedication goes to my parents, Carlos and Zelima, my wife, Carla, and the most rewarding gift of my life, my daughter, Izadora. Words will never be enough to express all my gratitude, admiration for their encouragement, love, understanding, support, and endless patience. My life would have no meaning without them.

TABLE OF CONTENTS

| | <u>page</u> |
|---|-------------|
| ACKNOWLEDGMENTS | iv |
| LIST OF TABLES | viii |
| LIST OF FIGURES | x |
| ABSTRACT..... | xiv |
| CHAPTERS | |
| 1. INTRODUCTION | 1 |
| 2. CHARACTERIZATION OF THE MICROSTRUCTURE, COMPOSITION, MECHANICAL PROPERTIES, AND PHYSICAL PROPERTIES OF LEUCITE- BASED AND LITHIA-DISILICATE-BASED CERAMICS | 4 |
| 2.1. Materials and Methods..... | 5 |
| 2.1.1. Ceramic Specimen Fabrication | 5 |
| 2.1.2. Quantitative and Qualitative Analyses..... | 6 |
| 2.1.2.1. Scanning electron microscopy (SEM) | 6 |
| 2.1.2.2. Backscattered imaging (BSI), and electron dispersive spectroscopy (EDS) | 7 |
| 2.1.2.3. X-ray diffraction (XRD) | 7 |
| 2.1.2.4. Fourier-transform infrared reflection spectroscopy (FTIR)..... | 8 |
| 2.1.3. Stereology | 8 |
| 2.1.4. Physical and Mechanical Properties | 9 |
| 2.2. Results..... | 10 |
| 2.3. Discussion..... | 13 |
| 3. FLEXURAL STRENGTH OF MONOLITHIC AND MULTILAYER CERAMIC STRUCTURES | 17 |
| 3.1. Materials and Methods..... | 18 |
| 3.1.1. Single- and Multilayer Specimen Preparation | 19 |
| 3.1.2. Four-point Flexural Strength Test..... | 20 |
| 3.1.3. Maximum Tensile Stress Calculation from Four-point Flexural Strength Test..... | 21 |
| 3.1.4. Fracture Surface Preparation for Fractography Analysis..... | 23 |
| 3.1.5. Statistical Analyses | 23 |
| 3.2. Results..... | 24 |

| | |
|---|-------------|
| 3.3. Discussion | 27 |
| 4. FRACTURE TOUGHNESS OF A GLASS VENEER, A LEUCITE-BASED CERAMIC, AND TWO LITHIA DISILICATE-BASED CERAMICS DETERMINED BY FRACTOGRAPHY AND FRACTAL ANALYSES | .32 |
| 4.1. Materials and Methods..... | 35 |
| 4.1.1. Fractography Approach for Fracture Toughness Determination | 35 |
| 4.1.2. Fractal Approach for Fracture Toughness Determination | 37 |
| 4.2. Results..... | 40 |
| 4.3. Discussion | 44 |
| 5. EFFECT OF SURFACE TREATMENT ON THE CONTACT ANGLE AND WORK OF ADHESION OF A LITHIA DISILICATE-BASED CERAMIC | .49 |
| 5.1. Materials and Methods..... | 52 |
| 5.1.1. Specimen preparation for Dynamic Contact Angle (DCA) analysis | 52 |
| 5.1.2. Dynamic Contact Angle (DCA) Analysis..... | 54 |
| 5.1.3. Statistical Analysis..... | 55 |
| 5.2. Results..... | 56 |
| 5.3. Discussion | 60 |
| 6. TENSILE BOND STRENGTH AND APPARENT INTERFACIAL FRACTURE TOUGHNESS OF THE ADHESION ZONE OF CERAMIC-RESIN SYSTEMS | .66 |
| 6.1. Materials and Methods..... | 69 |
| 6.1.1. Resin Composite Characterization..... | 70 |
| 6.1.2. Specimen Preparation for Microtensile Bond Strength Test | 70 |
| 6.1.3. Interface Indentation | 73 |
| 6.1.4. Microtensile Bond Strength Test | 75 |
| 6.2. Results..... | 76 |
| 6.3. Discussion | 86 |
| 7. CONCLUSIONS..... | .91 |
| APPENDICES | |
| A. FLEXURAL STRENGTH DATA (CHAPTER 3)..... | .97 |
| B. FRACTURE TOUGHNESS DATA (CHAPTER 4)..... | .101 |
| C. DYNAMIC CONTACT ANGLE (DCA) DATA (CHAPTER 5) | .103 |
| D. MICROTENSILE BOND STRENGTH AND APPARENT INTERFACIAL FRACTURE TOUGHNESS (CHAPTER 6)..... | .104 |
| LIST OF REFERENCES..... | .110 |
| BIOGRAPHICAL SKETCH | .121 |

LIST OF TABLES

| <u>Table</u> | <u>Page</u> |
|---|-------------|
| 2.1. Dental ceramics and firing procedures used in this study..... | 6 |
| 2.2. Mean values of stereological parameters, mechanical properties, and physical properties of Empress® ceramics | 10 |
| 2.3. Elemental concentration of IPS Empress2® glass veneer phases (Fig. 2.1) obtained by EDS analysis | 11 |
| 3.1. Mean flexural strength (σ) and standard deviation (SD), standard error (SE), Tukey's grouping ($\alpha = 0.05$), coefficient of variation (CV), characteristic strength (σ_{no}), Weibull modulus (m), and fracture origins for the 4-point flexure loading of single and multilayer hot-pressed ceramic bars (ISO Standard 6872)..... | 24 |
| 4.1. Fractal dimensional increment (D^*) using slit island analysis (SIA) and atomic force microscope [AFM], characteristic fracture length (a_0) range, and fracture toughness (K_{IC}) using equation (8) and equation (9) with values from D^*_{SIA} and D^*_{AFM} | 40 |
| 5.1. Materials used in this study..... | 53 |
| 5.2. Mean work of adhesion (WA) and mean values and standard deviation (SD) of advancing and receding contact angles (θ_a and θ_r) for all experimental groups..... | 58 |
| 6.1. Mean bonding area (A) and standard deviation (SD), mean tensile bond strength (σ) values and SD, Tukey's test subsets ($\alpha = 0.05$), characteristic strength (σ_{no}), and Weibull modulus (m) values for E1 and E2 ceramics bonded to resin..... | 78 |
| 6.2. Mean critical flaw size (c) and SD, crack origin, modes of failure, K_A ($MPa \cdot m^{1/2}$) and SD, and Tukey's test subsets ($\alpha = 0.05$) for E1 and E2 ceramics bonded to resin..... | 79 |
| 7.1. Mean values of the properties of a hot-pressed leucite-based ceramic (IPS Empress® - E1), two hot-pressed lithia disilicate-based ceramic | |

| | |
|---|----|
| (IPS Empress2® - E2, and experimental - ES), and a glass veneer (IPS Empress2® - GV) | 91 |
| 7.2. Mean values of advancing contact angle (θ_a), work of adhesion (W_A), tensile bond strength (σ), Weibull modulus (m), critical crack size (c), and apparent interfacial fracture toughness (K_A) for a hot-pressed leucite- based ceramic (IPS Empress® - E1) and a hot-pressed lithia disilicate-based ceramic (IPS Empress2® - E2) treated with hydrofluoric acid (HF), acidulated phosphate fluoride (APF), and/or silane coupling agent (S) | 94 |

LIST OF FIGURES

| <u>Figure</u> | | <u>Page</u> |
|---------------|--|-------------|
| 2.1. | SEM and BSI micrographs of lightly etched IPS Empress2® glass veneer. Compositions of (A) light glass phase, (B) dark glass phase, and white phase (white arrows) are presented below (Table 2.3). | 11 |
| 2.2. | SEM micrographs of IPS Empress® core ceramic (E1) etched with 2% HF for 10 s (A), and etched with 9.5% HF for 1 min (B). XRD analysis showed the presence of leucite crystals (*) in a glassy phase..... | 12 |
| 2.3. | SEM micrographs of IPS Empress2® core ceramic (E2) etched with 2% HF for 10 s (A), and etched with 9.5% HF for 1 min (B). XRD analysis showed the presence of lithia disilicate crystals (*) in a glassy phase (5,000x). | 12 |
| 2.4. | SEM micrographs of an experimental lithia disilicate-based core ceramic (ES) etched with 2% HF for 10 s (A), and etched with 9.5% HF for 1 min (B). XRD analysis showed the presence of lithia disilicate crystals (*) in a glassy phase (5,000x). | 13 |
| 3.1. | Schematic illustration of specimens: (A) dimensions for specimens in Groups 1-4 and 7 (monolithic specimen); (B) dimensions for the bilayer specimens in Group 5; (C) dimensions for the trilayer specimens in Group 6. | 19 |
| 3.2. | (A) Schematic representation of the four-point flexure test arrangement. The outer span length (L) is 20 mm, and the inner span is L/3. (B) Four-point flexural loading arrangement in 37°C distilled water (top right) controlled by the Isotemp immersion circulator (bottom left). | 21 |
| 3.3. | SEM images of representative fracture origins. (A) Void representing a surface flaw (SF) in the fracture surface of a specimen from Group 1; (B) crack (defect) representing a surface flaw (probably a processing defect) in the fracture surface of a specimen from Group 1; (C) void at the corner of fracture surface of a specimen from Group 1; and (D) flaw at the corner (CF) of the fracture surface of a specimen from Group 3. | 25 |
| 3.4. | SEM images of fracture surfaces of multilayer ceramic specimens. (A) bilayer specimen from Group 5 with fracture origin shown in the white | |

| | |
|---|----|
| box area; (B) enlarged view of white box area of A in which the fracture origin is the surface flaw in the ES ceramic indicated by the white arrows (350x); (C) trilayer specimen (Group 6) with a corner crack as the fracture origin (white box). The fracture plane changed after crossing the ES-GV interface by branching, producing small fracture fragments (chipping). Note the fracture “tails” (in the white circles) from pores (dark ellipses) on the GV layer pointing to the corner flaw origin; (D) enlarged view of white box area of C; corner flaw in the ES ceramic is indicated by the white arrows (350x)..... | 26 |
| 4.1. Diagram of the typical fracture surface features occurring in brittle materials. The regions are not drawn to scale. Adapted from Mecholsky (1993)..... | 33 |
| 4.2. Richardson technique used to measure collage coastline. | 37 |
| 4.3. SEM micrographs of ceramic fracture surfaces showing representative critical flaws outlined by white arrows. (A) Fracture surface of E1; line from flaw corner, $c = 84 \mu\text{m}$ (500x). (B) Fracture surface of E2; measured line represents the semi-minor axis, $a = 44 \mu\text{m}$ (500x). (C) Fracture surface of ES; measured line represents the semi-minor axis, $a = 35 \mu\text{m}$ (600x). (D) Fracture surface of GV; note the tailed fracture markings (top right) pointing to crack origin; measured line represents the semi-minor axis, $a = 55 \mu\text{m}$ (500x)..... | 41 |
| 4.4. Representative optical microscopy images of E1, E2, ES, and GV specimen replicas, from top (A) to bottom (D), respectively. The Richardson technique was applied to measure the contour lines (coastline collage) and to calculate D^* (400x). | 42 |
| 4.5. Atomic force micrographs of fracture surfaces of E1, E2, ES, and GV specimens, from top A to D, respectively. (Area = $25 \mu\text{m}^2$). | 43 |
| 4.6. Fracture toughness (KIC) versus fractal dimensional increment (D^*) for material classes including ceramic materials used in this dissertation (E1– star, E2– cross, ES– square, and GV– diamond). | 46 |
| 5.1. Schematic illustration of a liquid drop on a solid surface with energy vectors and contact angle (θ) as defined by equations 13-15..... | 50 |
| 5.2. Typical tensiogram of dynamic contact angle measurement. This is the result of a HF treated specimen being immersed in resin medium. | 55 |
| 5.3. SEM photomicrographs of IPS Empress2®. (A) Etching pattern produced by HF; the lithia disilicate crystals are clearly seen (also shown in Fig. 2.3B). (B) Etching pattern produced by APF; lithia disilicate crystals and some islands of the glass phase (darker areas) can be seen (2000x)..... | 59 |

| | | |
|------|--|----|
| 5.4. | SEM photomicrographs of IPS Empress2®. (A) HF-etched ceramic surface after silane coating; the silane completely fills the surface porosity created by HF producing an amorphous surface (500x). (B) Polished ceramic surface after silane coating; silane “beads up” on treated surface (200x) | 59 |
| 6.1. | Schematic illustration of specimen preparation sequence for microtensile test. (A) First set of cuts slices the composite/ceramic block to obtain slabs of about 1.0 mm in thickness. (B) The second set of cuts produces bars that were examined for flaws and stored in air environment for 7 days before performing the test. (C) Each bar was fixed to the flat “grips” of a Bencor Multi-T device and loaded to failure in tension. (D) Close-up schematic view of the adhesion zone (adapted from Della Bona <i>et al.</i> , 2000)..... | 72 |
| 6.2. | Micrographs of Vickers indentation at interface of (A) HF-treated E1 ceramic bonded to the resin composite, RC (Group 1), and (B) HF-treated E2 ceramic bonded to RC (Group 4). The adhesive resin (AR) layer varies in thickness (200x) | 74 |
| 6.3. | Schematic representation (side view) of the modes of failure for the microtensile bond strength test of ceramic bonded to resin composite. Mode 1: Adhesive separation at the ceramic-adhesive resin interface. Mode 2: Failure starts at the ceramic-adhesive interface, progresses into the adhesive resin and returns to the interface. Mode 3: Failure originates from an internal flaw (penny-shape internal crack). Mode 4: Failure starts at the ceramic-adhesive interface and propagates through the adhesive resin. Mode 5: Failure starts at the ceramic-adhesive interface, propagates through the adhesive resin to reach the resin composite- adhesive interface..... | 77 |
| 6.4. | SEM image (top) and X-ray elemental maps of fracture surface of Group 1. The label at the top of X-ray maps indicates the elements and their intensity. Note the adhesion zone fracture starting along the ceramic/adhesive interface by crack formation within the remaining glassy phase that was weakened by the etching process (Failure Mode 4). | 81 |
| 6.5. | SEM image (top) and X-ray elemental maps of fracture surface of Group 2. The label at the top of X-ray maps indicates the elements and their intensity..... | 82 |
| 6.6. | SEM image (top) and X-ray elemental maps of fracture surface of Group 8. The label at the top of X-ray maps indicates the elements and their intensity. Note that the fracture pattern is similar to that in Fig. 6.5 (Failure Mode 5). | 83 |
| 6.7. | Representative SEM micrographs of the modes of failure found in this study and schematically illustrated in Fig. 6.3. (A) semicircular flaw is the crack origin (in the white box); the adhesive resin island in | |

| | |
|--|----|
| the middle of the fracture surface represents what has been characterized as Failure Mode 2 (80x). (B) Enlargement of the white box area of (A) showing the measurement of the crack semi-minor axis ($a = 76 \mu\text{m}$) (300x). (C) Internal flaw is the crack origin characterizing Failure Mode 3 (80x). (D) Enlargement of the white box area of (C) showing the measurement of the flaw minor axis ($2b = 175 \mu\text{m}$) (250x). | 84 |
| 6.8. SEM micrographs of the modes of failure found in this study and schematically illustrated in Fig 6.3. (A) Failure starts at the ceramic-adhesive interface as a corner flaw (in the white box) and propagates through the adhesive resin (mode 4) (80x). (B) Enlargement of white box area of (A) showing the measurement of "c" ($55 \mu\text{m}$) (750x). (C) Failure starts at the ceramic-adhesive interface (white box), propagates through the adhesive resin to reach the resin composite-adhesive interface (left), characterizing Failure Mode 5 (80x). (D) Enlargement of white box area of (C) showing a semicircular crack resulting from indentation (white arrows); measurement line is "a" ($44 \mu\text{m}$) (370x). | 85 |
| 7.1. The apparent interfacial fracture toughness (K_A) versus the work of adhesion (W_A) of an adhesive resin to a lithia disilicate-based ceramic (E2) and a leucite-based ceramic (E1) treated with hydrofluoric acid (HF) and/or silane coupling agent (S). | 95 |

Abstract of Dissertation Presented to the Graduate School
of the University of Florida in Partial Fulfillment of the
Requirements for the Degree of Doctor of Philosophy

INTERFACIAL ADHESION OF DENTAL CERAMIC-RESIN SYSTEMS

By

Alvaro Della Bona

August 2001

Chairman: Dr. Kenneth J. Anusavice

Major Department: Materials Science and Engineering

The clinical success of resin bonding procedures for indirect ceramic restorations and ceramic repairs depends on the quality and durability of the bond between the ceramic and the resin. The quality of this bond will depend upon the bonding mechanisms that are controlled in part by the surface treatment that promotes micromechanical and/or chemical bonding to the substrate. The objective of this study is to correlate interfacial toughness (K_A) with fracture surface morphological parameters of the dental ceramic-resin systems as a function of ceramic surface treatment. The analytical procedures focused on characterizing the microstructure and fracture properties of Empress® ceramics (a leucite-based core ceramic, two lithia disilicate-based core ceramics, and a glass veneer) and determining the ceramic-resin adhesion zone bond strength characteristics.

Microstructure and composition are controlling factors in the development of micromechanical retention produced by etching. Silane treated ceramics negated the

effect of surface roughening produced by etching, inducing lower surface energy of the ceramic and, reduced bonding effectiveness. There was a positive correlation between W_A , tensile bond strength (σ), and K_A , *i.e.*, higher mean W_A value, and higher mean σ and K_A values.

This study suggests that (1) the σ and K_A values for ceramic bonded to resin are affected by the ceramic microstructure and the ceramic surface treatments; (2) the definition of the adhesion zone is essential to classify the modes of failure, which should be an integral component of all failure analyses; (3) the microtensile test may be preferable to conventional shear or flexural tests as an indicator of composite-ceramic bond quality; and (4) careful microscopic analysis of fracture surfaces and an x-ray dot map can produce a more consistent and complete description of the fracture process and interpretation of the modes of failure. The mode of failure and fractographic analyses provide important a more comprehensive assessment of mechanisms that control the survival times of dental adhesive systems. Thus, the quality of the bond should not be assessed based on bond strength data alone.

CHAPTER 1 INTRODUCTION

The discovery that most dental ceramics could be acid etched to create a micromechanical bond to resin has led to the development of acid-etched and bonded ceramic restorations (Hussain *et al.*, 1979; Horn, 1983). This concept was extended to include the repair of fractured dental ceramic restorations in the mouth. Fracture of ceramic restorations leads to increased cost, discomfort, time, and labor when a replacement is required (Anusavice and Lee, 1989). The repair of a fractured ceramic restoration is a challenging clinical situation and there is little documentation on the long-term clinical performance of the repaired restoration. Yet, repair is a more cost effective option, provided the final result is clinically acceptable.

Materials and procedures used either to repair fractured ceramic restorations with a resin composite or to bond indirect ceramic restorations to a resin cement are based on the results of bond strength tests that exhibit wide variability in test data and resulting fracture surface characteristics (Della Bona and van Noort, 1995; Pameijer *et al.*, 1996; Chadwick *et al.*, 1998; Leibrock *et al.*, 1999).

In the search for a method that produces a uniform stress distribution across the interface, investigators have evaluated similar adhesive systems under different bond test configurations (Della Bona and van Noort, 1995; Kitasako *et al.*, 1995; Cardoso *et al.*, 1998; Schreiner *et al.*, 1998). These studies suggest that a tensile bond strength test may be more appropriate to evaluate the bond strength of adhesive interfaces because of more

uniform interfacial stresses. However, tensile tests require careful alignment of the specimens to minimize the risk of flexure.

The physical contribution to the adhesion process is dependent on the surface topography of the substrate and can be characterized by its surface energy (Phoenix and Shen, 1995). Dynamic contact angle (DCA) analysis has been used to evaluate the surface energy of treated ceramic surfaces and their work of adhesion (W_A) to resin. In principle, the work of adhesion can be related to the apparent interface toughness (Anokye, 1989).

Fracture mechanics allows quantification of the relationships between material properties such as toughness, stress level, the presence of crack-producing flaws, and crack propagation mechanisms. Another way to assess the integrity of the bond is to estimate the apparent interfacial fracture toughness of the adhesion zone by promoting crack initiation within this zone. The apparent fracture toughness value (K_A) reflects the ability of a material to resist unstable crack propagation (Mecholsky and Barker, 1984; Tam and Pillar, 1993).

Fractography has been used to quantitatively relate the stress at failure, the nature of the stress state, and the amount of residual stress relative to the sizes of the initial crack and surrounding topography (Mandelbrot *et al.*, 1984). Quantitative fractographic analysis of brittle fracture surfaces shows that there are characteristic markings on the surfaces that are self-similar and scale invariant, implying that fractal analysis is a reasonable approach to analyze these surfaces (West *et al.*, 1999).

The objective of this study is to correlate apparent interfacial toughness with fracture surface morphological parameters of the dental ceramic-resin systems as a

function of ceramic surface treatment. This analysis is designed to identify mechanisms that promote adhesion of these ceramic-resin systems and an appropriate bond test method to yield relevant adhesion performance data.

The specific aims of this study were as follows: (1) to characterize the microstructure, composition, mechanical properties, and physical properties of Empress® dental ceramics; (2) to evaluate the flexural strength of monolithic and multi-layered ceramic bar specimens; and (3) to test the following hypotheses: (a) that the Weibull modulus of a multi-layered ceramic is controlled primarily by the structural reliability of the core; (b) that there is a positive correlation between the fractal dimensional increment (D^*) and the fracture toughness of these dental ceramics; (c) that the ceramic etching pattern is governed not only by the type of etchant but also by the ceramic microstructure and ceramic composition; (d) that the chemical etching and the application of silane coupling agent increase the work of adhesion (W_A) of the dental ceramic to adhesive resin; and (e) that the microtensile bond strength of Empress® ceramics to resin composite is controlled by the ceramic microstructure and the ceramic surface treatment.

This study presents some unique approaches to evaluate the interfacial adhesion of dental ceramic-resin systems: (1) the first application of the microtensile bond strength test to produce controlled failures within the adhesion zone; (2) the use of a liquid resin to perform dynamic contact angle (DCA) measurements to calculate the work of adhesion (W_A) for treated ceramic surfaces; and (3) the use of fracture mechanics and fractographic principles to determine the apparent fracture toughness (K_A) of interfacial zones.

CHAPTER 2

CHARACTERIZATION OF THE MICROSTRUCTURE, COMPOSITION, MECHANICAL PROPERTIES, AND PHYSICAL PROPERTIES OF LEUCITE- BASED AND LITHIA-DISILICATE-BASED CERAMICS

Quantifying microstructural parameters is important to develop structure/property relationships. Quantitative microstructural analysis provides an association among the constitution, physical properties, and structural characteristics of materials. Stereology describes the relationship between measurements made on the two-dimensional plane of polished surfaces and the three-dimensional microstructural features to be sampled.

There are several mechanical and physical properties that are used to characterize the behavior of ceramics: elastic modulus, Poisson's ratio, hardness and density. These properties will be discussed in this chapter. Fracture strength and toughness will be discussed later. The elastic or Young's modulus (E) is a measure of the stiffness, or the material's resistance to elastic deformation. The greater the modulus, the stiffer the material, or the smaller the elastic strain that results from the application of a given stress. The modulus is an important design parameter used for computing elastic deflections. Poisson's ratio (ν) is the ratio of the lateral to axial strain. Typically, ν value for isotropic materials is 0.25, but the maximum may be as high as 0.50. It is related to the shear modulus (G) and elastic modulus [$E = 2G(1 + \nu)$]. Hardness is a measure of material's resistance to plastic deformation. In a hardness test a load is placed on an indenter that is driven into the surface of the specimen. The degree to which the indenter penetrates the sample is a measure of the material's ability to resist plastic deformation. Some material

properties such as tensile strength, wear resistance, and fatigue resistance have been predicted from hardness data (Callister, 2000).

The volume of crystalline materials and their changes with temperature are closely related to the crystal structures. The density is directly determined by the crystal structure, that is, the efficiency of atomic packing. The density, as usually measured (g/cm^3), depends on the number of atoms per cubic centimeter and on the atomic weight of the constituents. The volume of a glass is largely determined by the nature of the vitreous network. The density is a minimum value for the pure network former and increases as modifier ions are added (Kingery *et al.*, 1976).

The objective of this chapter is to characterize the microstructure, composition, and some physical and mechanical properties of the leucite- and the lithia-disilicate-based ceramics used in this study. The results are necessary to calculate relevant mechanical properties and to support further arguments on fracture and bonding phenomena.

2.1. Materials and Methods

2.1.1. Ceramic Specimen Fabrication

The dental ceramics (Ivoclar AG, Schaan, Liechtenstein) and the firing procedures used in this study are presented in Table 2.1. The glass veneer (GV) IPS Empress2® body (batch #A14836), and the IPS Empress2® glaze (batch #C06631) specimens were fabricated using a metal mold and fired according to manufacturer's instructions (Table 2.1). The hot-pressed leucite-based core ceramic (IPS Empress®, batch #919788) and the two lithia-disilicate-based core ceramics (IPS Empress2®, batch #A11099; and experimental, batch #A09398) specimens were obtained using the lost-wax technique (Anusavice, 1996). After removal of the cast ceramic from the investment,

the interaction layer was removed from the specimen surface by grit blasting with 80 μm glass beads. The bar specimens were cleaned in 1% hydrofluoric acid for 30 min, grit blasted with 100 μm Al_2O_3 , and polished from 240 grit SiC abrasive through 1 μm alumina abrasive (Mark V Laboratory, East Granby, CT, U.S.A.). The specimens were ultrasonically cleaned in distilled water for 10 min.

Table 2.1. Dental ceramics and firing procedures used in this study

| Dental Ceramics | Starting T ($^{\circ}\text{C}$) | Heating rate ($^{\circ}\text{C}/\text{min}$) | Firing T ($^{\circ}\text{C}$) | Holding t (min) | Vacuum T on – off ($^{\circ}\text{C}$) |
|------------------------|-----------------------------------|--|---------------------------------|-----------------|--|
| E1- IPS Empress® core | 700 | 60 | 1180 | 20 | 500 - 1180 |
| E2- IPS Empress2® core | 700 | 60 | 920 | 20 | 500 - 920 |
| GV- IPS Empress2® body | 403 | 60 | 800 | 2 | 450 - 799 |
| ES- Experimental core | 700 | 60 | 910 | 15 | 500 - 910 |
| G- IPS Empress2® glaze | 403 | 60 | 760 | 2 | 450 - 759 |

T = Temperature

t = time

2.1.2. Quantitative and Qualitative Analyses

Quantitative and qualitative analyses of the ceramic microstructure were performed using scanning electron microscopy (SEM), backscattered imaging (BSI), electron dispersive spectroscopy (EDS), X-ray diffraction (XRD), and Fourier-transform infrared reflection spectroscopy (FTIR).

2.1.2.1. Scanning electron microscopy (SEM)

To enhance the observation of microstructural features, e.g., grains and grain boundaries, the ceramic specimens were etched with 2% aqueous hydrofluoric acid (HF)

for 10 s, rinsed in running water for 30 s, and air dried. Ceramic specimens were also etched with 9.5% HF (Ultradent Products Inc., South Jordan, UT, USA) for 1 min to create a typical clinical etching pattern.

The specimens were mounted on aluminum stubs using carbon coating paste for better conductivity and sputter-coated with gold-palladium for 3 min in a Hummer II Sputter Coater (21020, Technics Inc., Alexandria, VA, USA) at a current of 10 mA, and vacuum of 130 mTorr. Surface topography was examined using a scanning electron microscope (JSM 6400, Jeol Ltd., Tokyo, Japan).

2.1.2.2. Backscattered imaging (BSI), and electron dispersive spectroscopy (EDS)

As-polished and lightly etched ceramic specimens were carbon coated in a vacuum evaporation system (Ion Equipment Co., Santa Clara, CA, USA). The thickness of the carbon layer will be approximately 250 Å. The surface composition of each ceramic phase was determined by EDS using an electron microprobe X-ray analyzer (Jeol Superprobe 6400, Jeol LTD., Tokyo, Japan) and the ZAF correction method. The following parameters were used: accelerating voltage of 15 kV, current of 20 nA, and a spot size of 1-2 µm. Each ceramic phase was analyzed three times at different locations and average values of composition were determined. Compositional element concentration above 1 wt% was recorded.

2.1.2.3. X-ray diffraction (XRD)

Ceramic samples were ground down to powder, mixed with an adhesive (1:7 collodian – amyl acetate), and placed on a glass slide sample area. To identify the ceramic crystal phases, XRD was performed by a 3720 Phillips room temperature diffractometer (serial #1470, Phillips, Netherlands), and PW1877 automated powder diffraction software. A copper tube anode in a continuous scan from 3.01° to 89.97° ($\sim 3^{\circ}$ -

90⁰) with step size of 0.02⁰ every 0.4 s was used at a voltage of 40 kV, and a current of 20 nA. A slow scan from 10⁰ to 40⁰ was also used.

2.1.2.4. Fourier-transform infrared reflection spectroscopy (FTIR)

The IPS Empress2® glass veneer (GV) was analyzed for any crystal phase using a DRIFT (Diffuse Reflectance Infrared Fourier Transform, Spectra Tech Inc., Shelton, CT, USA) analyzer with a Gemini Stage (Nicolet Magna 760, Nicolet Inc., Madison, WI, USA) and OMNIC 4.1b software (Nicolet Inc., Madison, WI, USA). The following four powder samples were analyzed: (1) 0.5 g of KBr powder (Spectra Tech Inc., Shelton, CT, USA) for the background control; (2) 0.5 g of KBr powder mixed with 0.025 g of unfired incisal GV powder; (3) 0.5 g of KBr powder mixed with 0.025 g of unfired dentin GV powder; (4) 0.5 g of KBr powder mixed with 0.025 g of fired dentin GV powder. Analysis was performed in 64 scans for four wavenumber resolutions. The data was corrected for H₂O and CO₂ interferences.

2.1.3. Stereology

The crystalline volume fraction (V_v) was estimated by point counting (ASTM E562). Clear plastic grids with a number of systematically spaced points (88 and 187) were placed on a photomicrograph and the number of grid points lying on the crystals (P_a) was counted and divided by the total number of grid points (P_T). A point lying on a boundary was counted as half. This procedure was repeated on four fields from different sections selected without bias (Howard and Reed, 1998). The point fraction (P_P) was given by: P_P = P_a/P_T. Studies have shown that P_P is equal to the area fraction (A_A) and to the volume fraction, V_v, (P_P = A_A = V_v). The average area of the crystals (\bar{A}) was

calculated by dividing the crystal volume, V_v , by the number of crystals within a given measurement area (N_A) [$\bar{A} = V_v/N_A$] (DeHoff and Rhines, 1968; Boyer and Gall, 1992).

The volume fraction of the crystalline phases (V_v) was estimated using four BSI photomicrographs of randomly selected areas of the polished ceramic specimens under two different grids. The crystal V_v of E1, E2, and ES were calculated as the average of eight readings.

2.1.4. Physical and Mechanical Properties

The elastic modulus (E) and Poisson's ratio (ν) were determined by means of ultrasonic waves and a computer program (ECALC and Sigview-F software, Nuson Inc., Boalsburg, PA, USA) based on a set of equations that uses the time of flight, density (ρ), and thickness (t).

Ceramic disk specimens of each material used in the study (Table 2.1) were fabricated and polished through 1 μm alumina abrasive. The specimen thickness was measured using a caliper (Digimatic caliper, Mitutoyo Co., Kawasaki, Japan) and the weight (W) was obtained using an analytical balance (Mettler H31, Mettler Instrument Corp., Hightstown, NJ, USA). The density was obtained using a Helium Pycnometer (Accupyc 1330, Micromeritics Instrument Co., Norcross, GA, USA) after calculating the volume (V). Piezoelectric transducers (Ultran Laboratories Inc., Boalsburg, PA, USA) and an ultrasonic pulse apparatus (Ultima 5100, Nuson Inc., Boalsburg, PA, USA) were used to determine the time of flight through the ceramic specimens. Longitudinal and shear (transverse) time of flight values were obtained and used to calculate the ν and E of the materials.

A microhardness tester (Model MO Tukon Microhardness Tester, Wilson Instruments Inc., Binghamton, NY, USA) with a Vickers diamond was used to measure the hardness of the ceramic specimens that were fabricated and polished as described in section 2.1.1. Each specimen was indented in four different locations under a 9.8 N load. The dimensions of the indentation diagonals were measured using an optical microscope with a filar eyepiece. The hardness values were calculated according to the following equation:

$$H = [2P \sin(\theta/2)] / (\bar{a})^2 \quad (1)$$

where P is the indentation load, θ is the angle between opposite diamond faces (136^0), and \bar{a} is the mean diagonal length of the indentation.

2.2. Results

The calculations for crystalline volume fraction (V_V), average area of crystals (\bar{A}), density (ρ), elastic modulus (E), Poisson's ratio (ν), and Vickers hardness (H) yielded the results summarized in Table 2.2.

Table 2.2. Mean values of stereological parameters, mechanical properties, and physical properties of Empress® ceramics

| Material Properties | E1 | E2 | ES | GV |
|---------------------------------|-----------------------|-----------------------|-----------------------|-----------------------|
| Volume fraction (V_V) | 0.44 | 0.58 | 0.52 | |
| Area of particles (\bar{A}) | $18.12 \mu\text{m}^2$ | $0.42 \mu\text{m}^2$ | $0.20 \mu\text{m}^2$ | |
| Density (ρ) | 2.47 g/cm^3 | 2.51 g/cm^3 | 2.56 g/cm^3 | 2.53 g/cm^3 |
| Elastic modulus (E) | 86 GPa | 96 GPa | 96 GPa | 65 GPa |
| Poisson's ratio (ν) | 0.27 | 0.26 | 0.24 | 0.23 |
| Vickers hardness (H) | 5.9 GPa | 6.3 GPa | 6.3 GPa | 5.4 GPa |

Representative SEM and BSI micrographs of the microstructure, and the elemental concentration of IPS Empress2® glass veneer phases are presented in Fig. 2.1 and Table 2.3, respectively. A typical amorphous glass plot was produced by XRD analysis. The absence of any crystal phase was confirmed by FTIR analysis.

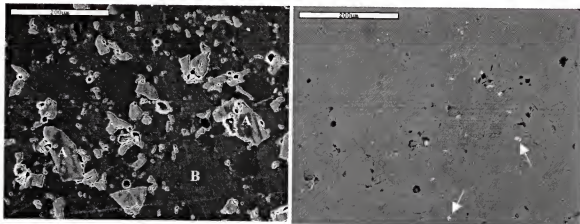


Fig. 2.1. SEM and BSI micrographs of lightly etched IPS Empress2® glass veneer. Compositions of (A) light glass phase, (B) dark glass phase, and white phase (white arrows) are presented below (Table 2.3).

Table 2.3. Elemental concentration of IPS Empress2® glass veneer phases (Fig. 2.1) obtained by EDS analysis

| Elements | (A) Light glass phase | (B) Dark glass phase | White phase |
|----------|-----------------------|----------------------|-------------|
| O | 30.84% | 32.48 % | 19.61% |
| Na | 3.88% | 4.93% | --- |
| Al | 9.87% | 4.69% | --- |
| Si | 29.22% | 35.05% | 8.86% |
| K | 7.04% | 5.90% | --- |
| Ca | 3.23% | 3.78% | --- |
| Zr | 5.54% | 3.78% | --- |
| Pd | 10.38% | 9.39% | 11.22% |
| Y | --- | --- | 60.31% |

XRD analyses showed that leucite ($K_2O \bullet Al_2O_3 \bullet 4SiO_2$) is the crystal phase in the IPS Empress® core ceramic (E1), and lithia disilicate ($Li_2O \bullet 2SiO_2$) is the crystal phase in the IPS Empress2® (E2) and experimental (ES) core ceramics. These crystal phases are shown in Figs. 2.2, 2.3, and 2.4. The length of the elongated $Li_2Si_2O_5$ crystals ranged from 0.5 μm to 4 μm for E2 and from 0.5 μm to 2 μm for ES.

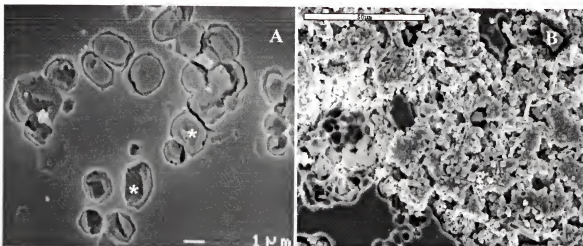


Fig. 2.2. SEM micrographs of IPS Empress® core ceramic (E1) etched with 2% HF for 10 s (A), and etched with 9.5% HF for 1 min (B). XRD analysis showed the presence of leucite crystals (*) in a glassy phase.

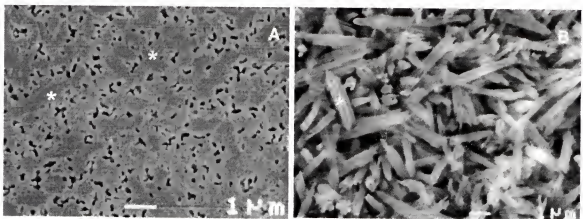


Fig. 2.3. SEM micrographs of IPS Empress2® core ceramic (E2) etched with 2% HF for 10 s (A), and etched with 9.5% HF for 1 min (B). XRD analysis showed the presence of lithia disilicate crystals (*) in a glassy phase (5,000x).

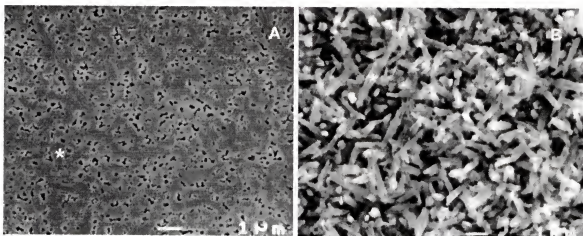


Fig. 2.4. SEM micrographs of an experimental lithia disilicate-based core ceramic (ES) etched with 2% HF for 10 s (A), and etched with 9.5% HF for 1 min (B). XRD analysis showed the presence of lithia disilicate crystals (*) in a glassy phase (5,000x).

2.3. Discussion

Microscopic examination is useful for the study and characterization of materials. Examination of microstructures is often related to material properties and the information is used to predict properties and improve the design of new materials.

There are important relationships between chemical composition, atomic structure, fabrication process, microstructure, and properties of polycrystalline ceramics. The role of the fabrication process, for example, is to produce microstructures with desired chemical characteristics and properties. Each processing step has the potential for producing undesirable microstructural flaws in the ceramic body that can limit its properties and reliability. Thus, the microstructure, which refers to the nature, size, shape, quantity, and distribution of the structural elements or phases in the ceramics, has a profound effect on physical properties (Rahaman, 1995).

The structure of each phase in dental ceramics depends greatly upon the firing conditions such as pre-heating temperature, heating rate, final firing temperature, hold-time at final temperature, atmosphere in firing oven, and the cooling rate (Table 2.1). The coefficient of thermal expansion, strength values, chemical solubility, transparency, and appearance are some of the properties that show some dependency on the degree and manner to which the structure is fired.

Some studies reported the chemical composition of certain dental ceramics using wavelength dispersive spectroscopy (WDS) or electron dispersive spectroscopy (EDS), X-ray photoelectron spectroscopy (XPS), and XRD (Mackert *et al.*, 1986; Claus, 1989; Anusavice, 1992; Roulet *et al.*, 1995; Della Bona and van Noort, 1998; Hooshmand *et al.*, 2001). Others reported the composition of specific crystal phases, *e.g.*, leucite (Mackert and Evans, 1991; Piche *et al.*, 1994; Denry *et al.*, 1996). Analyses of surface and bulk composition of five commercially available leucite-reinforced feldspathic ceramics (IPS Empress®, Optec HSP®, Vita VMK68®, Mirage®, and Mirage Fortress®) using XPS have shown the presence of a silica-rich surface layer due to a reduction in K and Na relative to the bulk composition. However, the surface composition and chemical states of the five ceramics were found to be virtually indistinguishable (Hooshmand *et al.*, 2001). This supports the compositional analysis protocol used in this study, which collects the information up to 1 μm from the specimen surface (EDS).

The microstructure of some dental ceramics has also been studied and related to physical properties (Denry *et al.*, 1996, 1998; Cattell *et al.*, 1997). The high-expanding mineral, leucite ($\text{K}_2\text{O} \bullet \text{Al}_2\text{O}_3 \bullet 4\text{SiO}_2$), is often associated with microcracks that result

from a thermal expansion mismatch between leucite and the surrounding glass matrix. This type of microcracking can be minimized by reducing the leucite particle size and by obtaining a homogeneous distribution of these particles throughout the ceramic (Mackert and Williams, 1996). Previous research has also shown that the fracture energy first increases with increasing grain size because of increased cracking, then decreases because of more pre-existing microcracks (Wu *et al.*, 1978). These microcracks were rarely observed in the leucite-based ceramic (E1) examined in this study (Fig. 2.2). This is probably a consequence of the hot-pressed fabrication process.

The crystal size and volume fraction of E1 and E2 correspond to the results presented in another study (Höland *et al.*, 2000). Although ES has smaller crystals and a lower V_v than E2, their physical properties are almost identical. Since there are no previous data for the physical and mechanical properties of ES, it is not possible to compare and contrast the present results with those from other studies.

Previous study reported on the effect of lithia disilicate crystallization as a toughening mechanism for glass-ceramics (Freiman and Hench, 1972). The crystal morphology makes crack propagation more difficult by requiring more energy, thereby increasing toughness. Combination of toughening techniques can be microstructurally designed to optimize the toughness and strength of glass-ceramics (Mecholsky, 1981).

The microstructural properties such as volume fraction and crystal size, reported in this study, are important for further interpretation of fracture processes. Previous research has shown that the grain size and the crystal structure are correlated with the crack phenomena regardless of processing or composition (Wu *et al.*, 1978). When the grain size of the material becomes large with respect to flaw size, the crack does not

encompass enough grains for the full polycrystalline toughness to apply. This results in a reduction in both fracture toughness and fracture strength. Yet, the dominant damage mode in any given material is dictated by the microstructure. Fine microstructures with minimal internal weakness tend to exhibit macroscopic cracks, and coarse microstructures with enhanced internal flaws tend to exhibit quasi-plastic zones. Both cracks and quasi-plasticity can lead to degradation of properties, and ultimately compromise the useful lifetimes of restorative structures, in different ways (Peterson *et al.*, 1998a, b; Lawn *et al.*, 1998). The two modes may be interactive: the quasi-plasticity can enhance or inhibit fracture by redistributing tensile stresses.

CHAPTER 3

FLEXURAL STRENGTH OF MONOLITHIC AND MULTILAYER CERAMIC STRUCTURES

Structural reliability of dental ceramics is a major factor in the clinical success of ceramic restorations. Complex stress distributions are present in most practical conditions and strength data alone cannot be directly extrapolated to predict structural performance (Kelly, 1995).

Failure predictions for ceramics depend on the experimental parameters that define the strength distribution and time dependency of strength. These parameters can be determined by measuring strength as a function of stressing rate in a test environment that simulates the service environment. Thus, well designed experiments coupled with a reliability analysis can optimize rational design decisions that ensure the successful use of ceramics in demanding structural applications (Ritter, 1995a).

Flexural strength is generally considered as a meaningful mechanical property for brittle materials that are much weaker in tension than in compression. The four-point flexure test is one method of assessing this property. This test method has been used for strength evaluation of single-component brittle materials (Ban and Anusavice, 1990; Giordano *et al.*, 1995; White *et al.*, 1996) and bilayered structures such as glass veneer on core ceramic specimens (White *et al.*, 1996; Thompson, 2000) and metal-ceramic structures (DeHoff *et al.*, 1982; Coffey *et al.*, 1988).

The failure strength of a brittle material is statistically distributed as a function of the homogeneity of the material. One commonly used statistic for the description of this parameter is the Weibull distribution. Higher values of Weibull modulus (m) correspond to a higher level of structural integrity of the material. Most ceramics have m values in the range of 5 to 15, whereas metals, which produce ductile failures, have m values ranging from 30 to 100 (Johnson, 1983). This analytical method based on statistical concepts is easily applied when reasonable numbers of samples are tested, and it enables fracture probability to be calculated as a function of applied stress (McCabe and Carrick, 1986). Yet, Weibull analysis has some limitations that challenge its ability to predict failure of components having complex geometries, especially when they are subjected to a multi-axial stress state. This may play an important role when dental restorations are analyzed (Ban and Anusavice, 1990). In the present study, the failure probability of monolithic and laminated ceramic structures was calculated from the results of the four-point flexure test.

The objective of this study was to test the hypothesis that Weibull moduli of single- and multilayer ceramics are controlled primarily by the structural reliability of the core ceramic.

3.1. Materials and Methods

The ceramic materials and firing procedures used in this study are presented in Table 2.1. Seven groups of 20 ceramic bar specimens were fabricated following the manufacturer's instructions (Ivoclar AG, Schaan, Liechtenstein) and ISO standard 6872 (1995). The specimen groups were as follows:

Group 1: a hot-pressed leucite-based core ceramic (E1);

Group 2: a hot-pressed lithia-based core ceramic (E2);

Group 3: a hot-pressed smaller grain lithia-based core ceramic (ES);

Group 4: a glass veneer (GV);

Group 5: a 1.1-mm-thick layer of ES plus a 0.1-mm-thick layer of glaze (G);

Group 6: a 0.8-mm-thick layer of ES, plus a 0.3-mm-thick layer of GV and a 0.1-mm-thick layer of G.

Group 7: same as for Group 3, except tested dry.

The total thickness of all the specimens was 1.2 mm (Fig. 3.1).

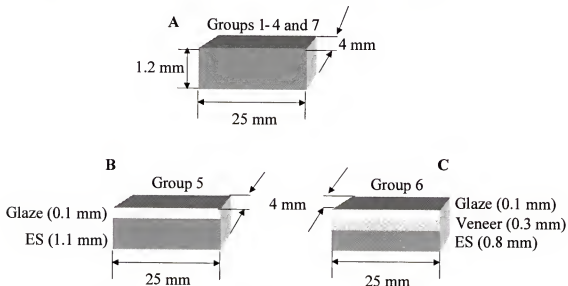


Fig. 3.1. Schematic illustration of specimens: (A) dimensions for specimens in Groups 1-4 and 7 (monolithic specimen); (B) dimensions for the bilayer specimens in Group 5; (C) dimensions for the trilayer specimens in Group 6.

3.1.1. Single- and Multilayer Specimen Preparation

Specimens in Group 4 were fabricated using a metal mold and the green-body GV bars were fired according to manufacturer's instructions (Table 2.1). The hot-pressed core ceramic bars (Groups 1-3 and 5-7) were obtained using the lost-wax technique. After

removal of the cast ceramic from the investment, the interaction layer was removed from the specimen surface by grit blasting with 80 μm glass beads. The bar specimens were cleaned in 1% hydrofluoric acid (HF) for 30 min, grit blasted with 100 μm Al_2O_3 , and polished through 1200 grit SiC metallographic paper to a thickness of 1.2 mm. Specimens in Groups 5 and 6 were further polished to obtain bars that were either 1.1-mm-thick or 0.8-mm-thick. To obtain the bilayer specimens in Group 5, a 0.1-mm-thick layer of glaze was applied and fired on the 1.1-mm-thick ES ceramic bar (Fig. 3.1). The trilayer specimens in Group 6 were obtained by applying and firing a 0.3-mm-thick layer of GV and a subsequent 0.1-mm-thick layer of glaze on the 0.8-mm-thick ES ceramic bar (Fig. 3.1).

All specimens were finished with 1 μm polishing alumina (Mark V Laboratory, East Granby, CT, U.S.A.) to the final dimensions (25 x 4 x 1.2 mm). They were ultrasonically and steam cleaned using distilled water and examined for flaws using light microscopy (microscope model SCW30L, Fisher Scientific, Thailand). Specimens in Groups 1-6 were stored for 48 h in distilled water at 37°C before testing. Specimens from Group 7 were stored for 24 h in a vacuum chamber filled with N_2 .

3.1.2. Four-point Flexural Strength Test

Except for specimens in Group 7 that were tested in a dry environment, each specimen was subjected to four-point flexure loading (Fig. 3.2A) at a cross-head speed of 0.5 mm/min in a universal testing machine (Model 1125, Instron Corp., Canton, MA, USA) while immersed in distilled water at 37°C (Fig. 3.2B). An Isotemp Immersion Circulator (Model 730, Fisher Scientific, Pittsburgh, PA, USA), connected to the testing chamber, was used to maintain the water at 37°C (Fig. 3.2B). The ceramic core surface

was placed under tensile stress during the flexural testing of multilayer structures (Groups 5 and 6). Failure loads were recorded and the flexural strength values were calculated.

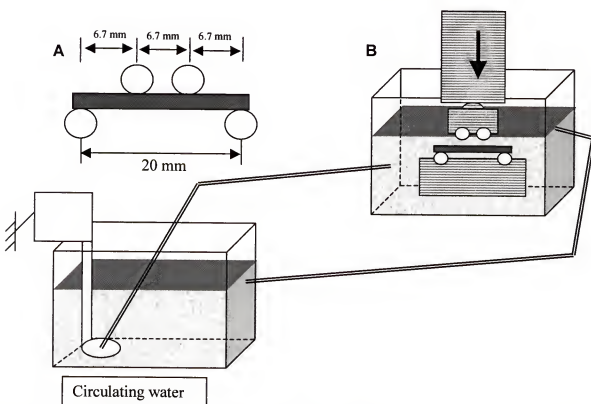


Fig. 3.2. (A) Schematic representation of the four-point flexure test arrangement. The outer span length (L) is 20 mm, and the inner span is $L/3$. (B) Four-point flexural loading arrangement in 37°C distilled water (top right) controlled by the Isotemp immersion circulator (bottom left).

3.1.3. Maximum Tensile Stress Calculation from Four-point Flexural Strength Test

The maximum tensile stress (σ) can be calculated using the following equation:

$$\sigma = MY / I \quad (2)$$

where M is the moment of the load, Y is the distance from the neutral axis to the outermost fiber, and I is the moment of inertia of the cross-section about the central axis.

For the four-point flexural strength test of monolithic material structures, which is the case for specimens in Groups 1-4 and 7: $M = PL / 6$, $Y = t / 2$, and $I = wt^3 / 12$. By substituting into equation (2), the following equation is developed:

$$\sigma = PL / wt^2 \quad (3)$$

where P is the applied load at failure, L is the length of the outer (total) span, w is the width of the specimen, and t is the thickness of the specimen (Ban and Anusavice, 1990).

For composite structures such as in Groups 5 and 6, equation (2) still applies but new values of Y and I (Y' and I_{TOT}) need to be calculated as follows:

$$Y' = [(t_c^2 / 2) + E_v / E_c ((t_v^2 / 2) + t_c t_v) + E_g / E_c ((t_g^2 / 2) + t_g t_v + t_g t_c)] / [t_c + (E_v / E_c) t_v + (E_g / E_c) t_g] \quad (4)$$

where t_c , t_v , and t_g are the thickness of the core, veneer and glaze ceramic layers, respectively, and E_c , E_v , and E_g are the elastic modulus (E) of the core, veneer, and glaze ceramic materials, respectively.

The total moment of inertia (I_{TOT}) for the specimens in Groups 5 and 6 is

$$I_{TOT} = \{ [(1 / 12) (E_g / E_c) w t_g^3] + [(E_g / E_c) w t_g (t_c + t_v + (t_g / 2) - Y')^2] + [(1 / 12) (E_v / E_c) w t_v^3] + [(E_v / E_c) w t_v (t_c + (t_v / 2) - Y')^2] + [(1 / 12) w t_c^3] + [w t_c ((t_c / 2) - Y')^2] \} \quad (5)$$

Therefore, the maximum tensile stress for the specimens in groups 5 and 6 was calculated using

$$\sigma = P L Y' / 6 I_{TOT} \quad (6)$$

The elastic modulus (E) and Poisson's ratio (ν) were determined as described in section 2.1.4.

3.1.4. Fracture Surface Preparation for Fractography Analysis

Fracture surfaces were examined using light microscopy (light microscope, Olympus Vanox, Tokyo, Japan) and scanning electron microscopy (SEM) to determine the mode of failure based on the fracture origin and fractographic principles (Rice, 1984; Fréchette, 1990; Mecholsky, 1995a). In preparation for SEM examination (JSM 6400, Jeol Ltd., Tokyo, Japan), the specimen fracture surfaces were sputter-coated with gold-palladium for 3 min in a Hummer II Sputter Coater (21020, Technics Inc., Alexandria, VA, USA) at a current of 10 mA, and a vacuum of 130 mTorr (Healey and Mecholsky, 1984).

3.1.5. Statistical Analyses

One-way ANOVA and Tukey's HSD (SAS program) were used to determine whether differences in group means were statistically significant. Weibull regression analysis was performed on the strength data as previously described (Ban and Anusavice, 1990). The description of the Weibull distribution is given by

$$P_f = 1 - \exp [- (\sigma/\sigma_{no})^m] \quad (7)$$

where P_f is the fracture probability, defined by the relation $P_f = \kappa/(N + 1)$, κ is the rank in strength from least to greatest, N denotes the total number of specimens in the sample, m is the shape parameter (Weibull modulus), and σ_{no} is the scale parameter or characteristic strength. The Weibull modulus, characteristic strength, and the strength at a predicted failure level of 5% were obtained through the use of a computer program designed to perform the Weibull analysis from the fracture data.

3.2. Results

The elastic modulus (E) and Poisson's ratio (ν) values are summarized in Table 2.2. The E value for glaze was assumed to be equal to that of the glass veneer.

Mean flexural strength values (σ) and standard deviations (SD), standard errors of the mean (SE), Tukey's grouping ($\alpha=0.05$), coefficient of variation (CV), characteristic strength (σ_{no}), Weibull modulus (m), and fracture origins for the 4-point flexure loading of single- and multilayer ceramic structures are summarized in Table 3.1.

Table 3.1. Mean flexural strength (σ) and standard deviation (SD), standard error (SE), Tukey's grouping ($\alpha = 0.05$), coefficient of variation (CV), characteristic strength (σ_{no}), Weibull modulus (m), and fracture origins for the 4-point flexure loading of single and multilayer hot-pressed ceramic bars (ISO Standard 6872)

| Groups - (material) | n | σ (SD) (MPa) | SE | Tukey's subsets | CV (%) | σ_{no} (MPa) | m | Fracture origin** |
|------------------------|----|------------------------|-----|--------------------|-----------|------------------------|-----|----------------------|
| 1- (E1) | 20 | 84.5 (14.6) | 3.3 | C | 17.3 | 91.3 | 5.2 | SF (14); CF (6) |
| 2- (E2) | 20 | 215 (40.1) | 8.9 | B | 18.6 | 231 | 5.4 | SF (14); CF (6) |
| 3- (ES) | 20 | 239 (36.3) | 8.1 | B | 15.2 | 252 | 7.2 | SF (16); CF (4) |
| 4- (GV) | 20 | 63.8 (5.8) | 1.3 | C | 9.1 | 65.7 | 14 | SF (16); CF (4) |
| 5- (ES-G) | 20 | 231 (45.0) | 10 | B | 19.5 | 248 | 5.0 | SF (16); CF (4) |
| 6- (ES-GV-G) | 20 | 238 (40.5) | 9.1 | B | 17.0 | 257 | 6.1 | SF (14); CF (6) |
| 7- (ES)* | 20 | 285 (48.9) | 11 | A | 17.1 | 300 | 6.2 | SF (15); CF (5) |

Specimens in Groups 1-6 were stored for 48 h in distilled water at 37°C before testing in distilled water at 37°C. *Specimens in Group 7 were stored for 24 h in a vacuumed chamber filled with N₂ and tested in dry environment. ** Type of fracture origins:
SF = surface flaw (void or crack); CF = corner flaw (void or crack).

No significant differences were found between the mean flexural strength values of Groups 2, 3, 5, and 6 as well as between Groups 1 and 4 ($p > 0.05$). However, significant differences were found between groups in a dry environment (Group 7) and wet (Groups 1-6) testing conditions. A 0.1-mm-thick layer of glaze on the ES ceramic (Group 5) or on the glass veneer (Group 6) had no significant effect on the flexural strength (σ) or Weibull modulus (m). The mean flexural strength and Weibull modulus of ES (Group 3) were similar to those of the two veneered ES groups (Table 3.1).

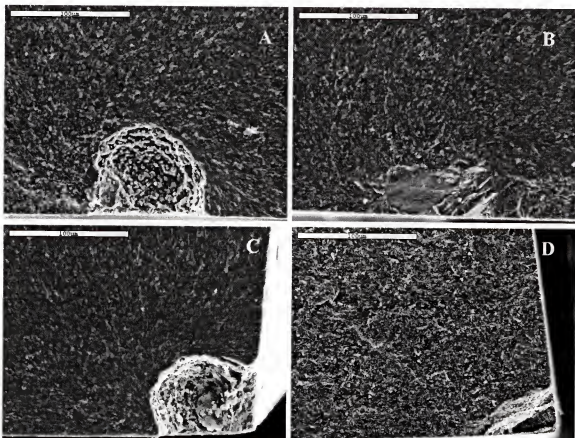


Fig. 3.3. SEM images of representative fracture origins. (A) Void representing a surface flaw (SF) in the fracture surface of a specimen from Group 1; (B) crack (defect) representing a surface flaw (probably a processing defect) in the fracture surface of a specimen from Group 1; (C) void at the corner of fracture surface of a specimen from Group 1; and (D) flaw at the corner (CF) of the fracture surface of a specimen from Group 3.

All fractures initiated at the tensile surface between the inner load points. Corner flaws, either cracks or voids, were identified as the fracture origin in about 25% of the specimens (Fig. 3.3). Some failures in Group 6 produced small chips within the glass veneer layer (Fig. 3.4).

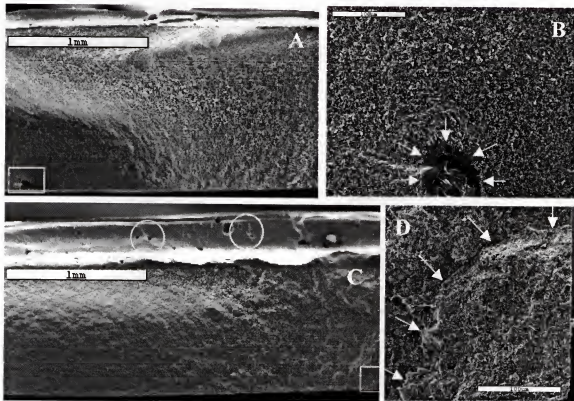


Fig. 3.4. SEM images of fracture surfaces of multilayer ceramic specimens. (A) bilayer specimen from Group 5 with fracture origin shown in the white box area; (B) enlarged view of white box area of A in which the fracture origin is the surface flaw in the ES ceramic indicated by the white arrows (350x); (C) trilayer specimen (Group 6) with a corner crack as the fracture origin (white box). The fracture plane changed after crossing the ES-GV interface by branching, producing small fracture fragments (chipping). Note the fracture "tails" (in the white circles) from pores (dark ellipses) on the GV layer pointing to the corner flaw origin; (D) enlarged view of white box area of C; corner flaw in the ES ceramic is indicated by the white arrows (350x).

3.3. Discussion

Mechanical failure occurs when the applied stress becomes greater than the strength of the material. The strength of a material is dependent on the size of the initiating crack present in a particular sample or component (Mecholsky, 1995b). The large number of pre-existing ceramic cracks, coupled with a low fracture toughness, limit the strength of ceramics and cause a large variability in strength and time-dependency. Variability in strength is a consequence of the distribution in crack sizes, and the time dependency of strength results from the slow growth of these flaws to dimensions critical for catastrophic failure (Ritter, 1995b).

Surface cracks can be induced by machining or grinding. Usually, failure of the ceramic originates from the most severe flaw. The size and spatial distribution of flaws justify the necessity of a statistical approach to failure analysis (Weibull, 1939). Thus, the reliability of ceramics under flexural loading can be based on Weibull analysis.

The flexural strength is generally considered a meaningful mechanical property. However, only the control of flaw distribution can validate this approach. Although the “strength” is used as a measure of reliability, toughness is a more meaningful property. The four-point flexure test is a valid method to assess the strength distribution found in components. Previous studies employed this test method for strength evaluation of monolithic specimens (Ban and Anusavice, 1990; Giordano *et al.*, 1995; White *et al.*, 1996) and bilayered structures (DeHoff *et al.*, 1982; Coffey *et al.*, 1988; White *et al.*, 1996; Thompson, 2000).

However, for the strength test to accurately reflect the variability and time-dependency of a ceramic component in service, the test environment must be similar to the service environment, and the strength-controlling flaw population must be the same

as that responsible for failure in service (Ritter, 1995a). These factors are the basis for the selection of methodology in this study, using a distribution of flexural strengths to evaluate the performance of ceramic structures in a wet environment. The distribution of strength is a measure of the distribution of the effective flaw sizes leading to failure.

Investigations of clinically failed all-ceramic restorations have shown that the fracture origin is typically located at the internal (tensile) surface of the crowns (Kelly *et al.*, 1989; Kelly *et al.*, 1990; Thompson *et al.*, 1994). These results justified placement of the ceramic core surface at the tensile side for flexural testing of multi-layer structures (Groups 5 and 6).

Evaluation of the damage modes in bilayer ceramic structures using an Hertzian contact test has shown that the substrate has a profound influence on the evolution damage from initiation to ultimate failure in the bilayer systems (Tsai *et al.*, 1998; Jung *et al.*, 1999). Nevertheless, crack initiation tends to occur at the top surface in systems having a strong bonded interface and a small elastic-plastic mismatch (glass / glass-ceramic); whereas in systems with a large mismatch, crack initiation tends to occur at the internal interface (Wuttiphhan *et al.*, 1996). However, the core/veneer thickness ratio (t_c/t_v) appears to be the dominant factor that controls the failure initiation site in bilayer ceramic structures (Wakabayashi and Anusavice, 2000; Thompson, 2000). The crack initiation site shifts from veneer to core as the t_c/t_v ratio increases. However, an increase in the elastic modulus of the supporting substrate did not affect the crack initiation site (Wakabayashi and Anusavice, 2000).

The results of this study are consistent with those of Luthy *et al.* (1993) who found no difference in the strength of IPS Empress core ceramic or Empress coated with

surface stain and glazed or veneered with unglazed porcelain. Glazing of either the experimental core ceramic (Group 5) or the glass veneer (Group 6) had no significant effect on the flexural strength or Weibull modulus ($p > 0.05$). The m value for E1 agrees with the value reported in previous research (Cattell *et al.*, 1997). This finding is in agreement with similar results reported for feldspathic porcelain (Fairhurst *et al.*, 1992).

Previous studies revealed that the mean flexural strength is about 30% higher than the values presented in this study for the monolithic ceramic materials (Cattell *et al.*, 1997; Höland *et al.*, 2000). However, these investigators used a three-point flexural strength test at room atmosphere, which is expected to produce higher mean flexural strength values of this magnitude. Significant differences in strength were attributed to the difference in testing environments for ES ceramic (Groups 3 and 7). Storing and testing the specimens in water (Group 3) produced statistically significant ($p \leq 0.05$) differences in mean strength compared with those stored and tested in dry environment (Group 7).

Fracture surface analysis (fractography) is well-established as a means of failure analysis in the field of glasses and ceramics. It has been recognized as a powerful analytical tool in dentistry (Kelly *et al.*, 1989; Thompson *et al.*, 1994). The application of fractography is based on the principle that the entire history of the fracture process is encoded on the fracture surface of brittle materials (Mecholsky, 1995a).

Fracture in glass occurs when preexisting cracks propagate under excessive tensile stresses. These cracks can be induced by mechanical means (e.g., grinding or polishing), by processing, or by intrinsic defects (e.g., imperfections in the structure). Most evidence shows that crack propagation is determined by varying levels of stress

intensity or energy and, because of these relationships, much information is contained within the fracture surface (Mecholsky, 1993). In the present study, fractography confirmed the presence of characteristic markings of the fracture process (Figs. 3.3 and 3.4) and the change in direction of crack propagation (branching) leading to chipping (Fig. 3.4C).

Ceramic specimens tested in bending are very sensitive to edge or surface machining damage (Ritter, 1995a). Fractographic analysis has shown that all failures started from either a surface (Figs. 3.3A, 3.3B, 3.4A, and 3.4B) or from a corner flaw (Figs. 3.3C, 3.3D, 3.4C, and 3.4D) located along the tensile surface of the specimens (Table 3.1). These results are consistent with those of Thompson (2000) who found surface failures starting only at the tensile side of specimens tested in four-point bending. However, the number of fracture origins from corner flaws (25%) determined in this study may suggest rounding specimen edges as a revision of ISO 6872, the specimen preparation standard for dental ceramics.

The Weibull modulus (m) is a measure of the distribution of critical flaws. As the Weibull moduli are similar in most cases (except for Group 4), a crack size difference cannot explain the strength differences. Thus, the differences in strength can be explained by the differences in toughness that, in turn, are related to the way the materials are processed.

The mean flexural strength and Weibull modulus of the ES ceramic (Group 3) were similar to those of the two veneered ES groups (Groups 5 and 6). Fracture analysis also showed similar results for these three groups. Therefore, we conclude that the structural reliability of veneered core ceramic is controlled primarily by that of the core

ceramic. Additional study is needed to determine the critical core/veneer thickness ratio below which strength and structural reliability become significantly reduced. This information will improve our ability to design ceramic-based prostheses with a sufficiently high margin of safety.

CHAPTER 4

FRACTURE TOUGHNESS OF A GLASS VENEER, A LEUCITE-BASED CERAMIC,
AND TWO LITHIA DISILICATE-BASED CERAMICS DETERMINED BY
FRACTOGRAPHY AND FRACTAL ANALYSES

The appeal of ceramics as structural dental materials is based on their, biocompatibility, low density, high hardness values, chemical inertness, and anticipated unique tribological characteristics. A major goal of current ceramic research and development is to produce tough, strong ceramics that can provide reliable performance in dental applications.

Brittle fracture represents a complex process (Griffith, 1920; West *et al.*, 1999). The fracture process creates at least two new surfaces with distinct topography and texture that can be characterized using principles of fractography. Quantitative fractographic analysis applies the principles of fracture mechanics to the topography observed on the fracture surface of brittle materials. There is specific, quantitative information to be obtained from the fracture surface including: (1) the identification of the size and location of the fracture initiating crack or defect, (2) the stress state at failure, (3) the effect of stress corrosion, (4) knowledge of local processing anomalies that affect the fracture process (see also discussion in section 3.3), and (5) the calculation of the fracture toughness (Mecholsky, 1995a).

Fracture toughness values are used extensively to characterize the fracture resistance of brittle materials (Anstis *et al.*, 1981; Chantikul *et al.*, 1981; Kelly, 1995; Scherrer *et al.*, 1998; Scherrer *et al.*, 1999). The fracture toughness of brittle ceramics is usually controlled by fracture in Mode I (opening mode, tensile load). Irwin (1957)

defined failure at the point when the Mode I stress intensity (K_I) reaches a critical value ($K_I \geq K_{IC}$). The critical stress intensity factor (K_{IC}) is in many cases a material constant and is one measure of the toughness of the material, *i.e.*, the resistance to crack propagation. Therefore, the fracture toughness or critical stress intensity factor (K_{IC}) can often be determined using the Griffith-Irwin equation:

$$K_{IC} = Y \sigma_a c^{1/2} \quad (8)$$

where Y is a geometrical factor that accounts for the location and geometry of the crack and loading (Randall, 1966), σ_a is the applied stress, and c is the radius of an equivalent semi-circular crack for a semi-elliptical crack of semi-minor axis "a" and semi-major axis "b" (Fig. 4.1) (Mecholsky *et al.*, 1978; and Mecholsky, 1995b).

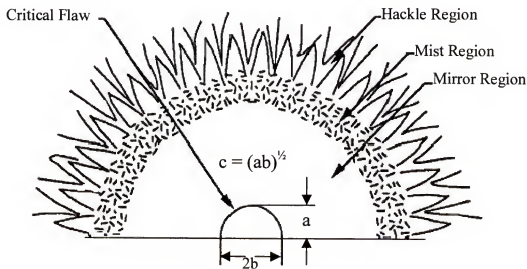


Fig. 4.1. Diagram of the typical fracture surface features occurring in brittle materials. The regions are not drawn to scale. Adapted from Mecholsky (1993).

Quantitative fractographic analysis of brittle fracture surfaces shows that there are characteristic markings on the surfaces that are self-similar and scale invariant, implying

that fractal analysis is a reasonable approach to analyzing these surfaces (West *et al.*, 1999). Fractal geometry is a non-Euclidean geometry that can quantitatively define irregular shapes and surfaces. Fractals are geometrical objects that are self-similar (or self-affine) and scale invariant and are characterized by non-integer dimensions. A self-similar object is one in which the length scaling is isotropic and remains invariant under the transformation (x, y, z) to (ax, ay, az) where "a" is a scalar constant. A self-affine object is one that remains invariant under the transformation (x, y, z) to (ax, ay, az^R) where R is called the roughness exponent. A scale invariant object is one in which the geometric surface will not be statistically different at any magnification scale (Bouchaud *et al.*, 1993).

The use of fractal dimension (D) measurements to characterize rough surfaces, e.g., fracture surfaces, has become popular since Mandelbrot (1982) re-introduced the concept of fractal geometry. Several authors have used fractal geometry to quantitatively describe irregular fracture surfaces (Mandelbrot *et al.*, 1984; Mecholsky *et al.*, 1989; Alexander, 1990; Mecholsky and Plaia, 1992; Chen *et al.*, 1997). The larger the value of D, the more tortuous the surface. Thus, a fracture surface may have a fractal dimension of 2.3 where 2 is the topological dimension and 0.3 is the fractal dimensional increment, D^* .

Fractography also has been used to relate the flaw/mirror size ratio and the fracture toughness, which, in turn, is related to the elastic modulus. The combination of these relationships show that the D^* is directly related to the flaw/mirror size ratio. This implies that there is a linear scaling law between the energy of crack initiation and the

energy of microbranching at fracture and this relationship is reflected in the features on the fracture surface (Mecholsky, 1996; Mecholsky and Freiman, 1991).

It has been shown that D^* is correlated to K_{IC} for many brittle materials using the equation (Mecholsky *et al.*, 1988):

$$K_{IC} = E a_0^{1/2} D^{*1/2} \quad (9)$$

where E is the elastic modulus, and a_0 is the characteristic fracture length on the atomic scale. The a_0 value is the slope of a graph of fracture energy (γ) versus ED^* ($a_0 = 2\gamma / ED^*$) (Mecholsky *et al.*, 1989).

The objective of this study was to test the hypothesis that there is a positive correlation between the fractal dimensional increment (D^*) and the fracture toughness of a glass veneer, a leucite-based ceramic, and two lithia disilicate-based ceramics.

4.1. Materials and Methods

The fracture surfaces used in this study were produced from loading monolithic bar specimens to failure in four-point flexural strength tests as described in section 3.1.2. The ceramic materials (E1, E2, ES, and GV) and firing procedures used for the specimens are presented in Table 2.1, and the specimen preparation described in section 3.1.1. Mean fracture toughness data were analyzed statistically using one-way ANOVA and Tukey's multiple range test.

4.1.1. Fractography Approach for Fracture Toughness Determination

Fracture surfaces were prepared for fractographic analysis as described in section 3.1.4. The critical crack was located and its size (c) was determined using fractographic principles described above (Fig. 4.1). As noted in section 3.2, corner flaws were found in

addition to surface flaws. For corner cracks, the critical size (c) is calculated using the same equation as for the equivalent semicircular surface crack [$c = (ab)^{1/2}$] (Fig. 4.1). However, “ a ” is the length of one side of the corner crack and “ b ” is the length of the other side of the corner crack. So, in this case, (c) corresponds to the distance from the crack corner to the critical flaw-mirror region limit (Figs. 4.3A and 6.8B). For internal flaws (Figs. 6.7C and 6.7D), “ c ” is also calculated by [$c = (ab)^{1/2}$]. However, “ a ” is half of the crack major axis and “ b ” is half of the crack minor axis.

The critical crack size (c) and strength (σ) values were used to calculate the fracture toughness (K_{IC}) using equation 8. The geometrical factor (Y) was calculated based on Randall’s (1966) interpretation of Irwin’s (1957) work:

$$Y = [0.515 Q^{1/2}]^{-1} \quad (10)$$

The factor Q depends primarily on the ratio of crack depth-to-length ratio and secondarily on a correction term for plastic strains near the crack boundary. Neglecting the latter, Q ranges in value from 1.00 for long, shallow cracks ($Y=1.94$) to 2.46 for semi-circular cracks ($Y=1.24$). For the penny-shape, internal flaw, $Y=1.12$. Since a corner crack lies along two free surfaces, the Y factor can be approximated by

$$Y = (1.12)^2 2/(\pi)^{1/2} \quad (11)$$

where $(1.12)^2$ represents two surface flaw corrections and $2/(\pi)^{1/2}$ represents the correction for a penny-shaped embedded crack (Hertzberg, 1996). Thus, $Y = 1.4$ for corner cracks.

The correction factors suggested for K_{IC} are proper, but no claim can be made that they will give a constant value of K_{IC} for a given material, independent of crack size. Yet, the basic reason for use of a K_{IC} value to characterize fracture toughness is that it permits the correlation of stress to flaw size (Randall, 1966).

4.1.2. Fractal Approach for Fracture Toughness Determination

The conceptual simplicity of the fractal dimension for a surface is not matched by ease of measurement. Many researchers (Mandelbrot *et al.*, 1984; Mecholsky and Plaia, 1992; Chen *et al.*, 1997; Hill *et al.*, 2001; Della Bona *et al.*, 2001) have used slit-island analysis (SIA) to obtain fracture surface (horizontal) contours, along with the Richardson technique for fractal dimension determination. In this technique the length (L) of a coastline is measured repeatably using different ruler units (S). The slope of L vs. S is related to the fractal dimension (Fig. 4.2).

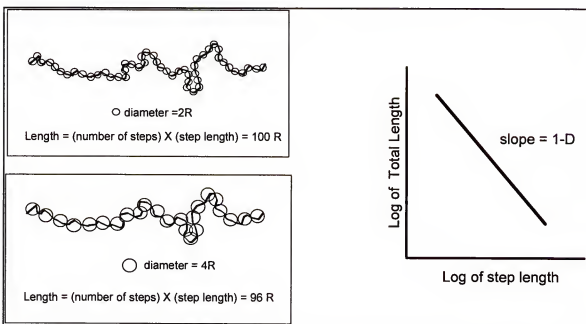


Fig. 4.2. Richardson technique used to measure collage coastline.

Fractal analysis was performed to obtain the fractal dimensional increment (D^*) using the slit island technique and the Richardson's procedure (plot in Fig. 4.2) to measure the D^* of boundary lines (Russ, 1994). The fracture toughness was calculated using equation 9. The elastic modulus (E) was determined as described in section 2.1.4. The characteristic fracture length (a_0) was assumed to be 20-80 Å for the ceramic

materials (E1, E2, ES) and 10-20 Å for the glass veneer (GV) (Mecholsky *et al.*, 1988; West *et al.*, 1999).

A comprehensive literature review and the technique used for fractal analysis of brittle materials used in this study have been reported in previous work (Hill *et al.*, 2001; Della Bona *et al.*, 2001). In summary, this technique consists of the following procedures: (1) replicate the fracture surface using high resolution impression material; (2) use a thin and high contrast coating; (3) polish through the fracture surface to produce “slit island” profiles; (4) take photographs of boundary at appropriate magnification, *e.g.*, 400x, using an optical microscope; and (5) measure the “coastline collage” using the Richardson technique described above.

Slit island analysis (SIA) has been successfully used to measure the fractal dimensional increment (D^*) of fracture surfaces. The fracture toughness in brittle ceramics is related to the fractal dimensional increment as described in section 4.1.2. However, the measurement technique may affect the determined D^* values (Hill *et al.*, 2001; Della Bona *et al.*, 2001). There is general agreement that a fracture surface can be a self-affine object, not a self-similar one (Bouchaud *et al.*, 1993; Mandelbrot *et al.*, 1984; Russ, 1994). This means that as long as a zero-set plane is created through the fracture surface in the (x, y) plane, the values are valid for the surface using any technique to determine the fractal dimension. Thus, a fracture surface is self-similar in a plane parallel to the surface. Some measurement techniques of the fractal dimension account for the self-affinity of an object or surface while other techniques do not produce valid results. In theory, the Richardson technique does not give an accurate fractal dimension unless the plane in which the measurement is being taken is in the zero-set

plane (Russ, 1994). Previous research has confirmed this analysis, showing that the SIA technique is sensitive to the contour angle since D^* decreases with increasing contour angle (Della Bona *et al.*, 2001). Therefore, the recommended protocol for fractal analysis was followed carefully in this study (Hill *et al.*, 2001).

Three fracture surfaces from each group were also examined by an atomic force microscope (Nanoscope III, Model MMAFM-2, Digital Instruments, Santa Barbara, CA, USA) using contact mode and a long, vertical scanner to determine D^* . The contact mode is indicated for harder surfaces, *e.g.*, ceramics. The contact mode works by scanning the tip over the surface in direct contact by holding the deflection of the tip constant. The repulsive force is measured and a surface image is derived from the information. The scanner used was capable of 125 μm maximum lateral resolution and 5.5 μm maximum vertical resolution. This scanner was used because of its ability to move the tip accurately over large distances and still acquire images with no distortion. All scans taken for purposes of quantitative measurements were 5 μm^2 scans. This size was chosen because it allowed the best compromise between capturing details of the smallest features and imaging the largest features.

Prior to quantitative measurements, all of the images taken with the Nanoscope were processed through two software filters. The images were first flattened to remove the arcing effect inherent in the piezoelectric scanner that the Nanoscope utilizes. The images were then fit in the x and y planes. The effect of this filter is to remove the slope from the image. This is done by performing a linear two-dimensional fit to the height data in the image. The slope is then removed from the fitted plane in the x and y directions, resulting in an image of zero median slope. Both of the filters were used to ensure that the

images taken were a true representation of the surface and that all quantitative data taken from them was accurate.

4.2. Results

The elastic modulus (E) and the mean flexural strength values (σ) of the ceramics used in this study are presented in Table 2.2 and Table 3.1, respectively.

The fracture toughness (K_{IC}) values calculated using equations 8 and 9, the range of characteristic fracture length (a_0) values, and the fractal dimensional increment (D^*) determined using either the slit island analysis (D^*_{SIA}) or the atomic force microscope (D^*_{AFM}), for the ceramic materials used in this study are summarized in Table 4.1.

Table 4.1. Fractal dimensional increment (D^*) using slit island analysis (SIA) and atomic force microscope [AFM], characteristic fracture length (a_0) range, and fracture toughness (K_{IC}) using equation (8) and equation (9) with values from D^*_{SIA} and D^*_{AFM}

| Groups | D^*_{SIA} and D^*_{AFM} | a_0 (Å) | K_{IC} (MPa \cdot m $^{1/2}$) Using E ($a_0 D^*$) $^{1/2}$ equation (9) | K_{IC} (MPa \cdot m $^{1/2}$) Using Y $\sigma_f c^{1/2}$ equation (8) | K_{IC} (MPa \cdot m $^{1/2}$) Using SENB [#] |
|--------|--------------------------------|-----------|--|--|---|
| E1 | 0.06 \pm 0.01 SIA | 20-80 | 1.0 – 1.9 SIA | 1.3 \pm 0.3 | 1.3 \pm 0.1 [†] |
| | 0.08 \pm 0.02 AFM | | 1.1 – 2.1 AFM | | 1.2 \pm 0.2 [‡] |
| E2 | 0.11 \pm 0.02 SIA | 20-80 | 1.4 – 2.9 SIA | 3.4 \pm 0.6 | 3.3 \pm 0.3 [†] |
| | 0.17 \pm 0.03 AFM | | 1.8 – 3.6 AFM | | |
| ES | 0.12 \pm 0.02 SIA | 20-80 | 1.5 – 3.0 SIA | 3.1 \pm 0.4 | --- |
| | 0.19 \pm 0.02 AFM | | 1.9 – 3.7 AFM | | |
| GV | 0.09 \pm 0.005 SIA | 10-20 | 0.6 – 0.9 SIA | 0.77 \pm 0.09 | --- |
| | 0.09 \pm 0.01 AFM | | 0.6 – 0.9 AFM | | |

[#] Results from Höland *et al.* (2000)[†], and Drummond *et al.* (2000)[‡], using single edge notched beam (SENB) method.

Representative SEM micrographs of the fracture surfaces are presented in Figs 3.3 and 4.3. Representative optical microscopy images of the specimen replicas showing the contour lines (coastline collage) for the Richardson technique to calculate D^* are shown in Fig 4.4. Representative atomic force micrographs of the fracture surfaces of E1, E2, ES, and GV materials are shown in Fig 4.5.

One-way ANOVA and Tukey's test subsets showed no significant statistical differences between Groups 2 and 3 tested using equation 8 ($p \leq 0.05$).

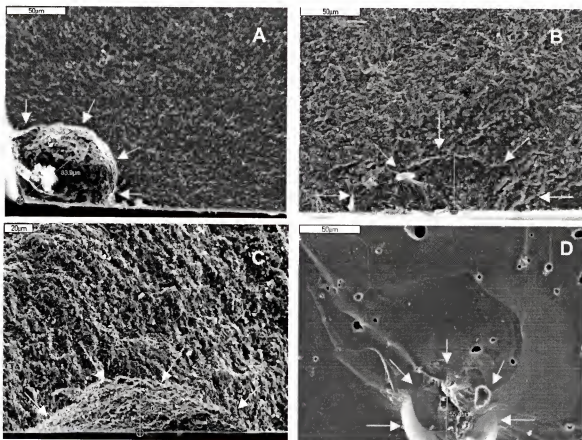


Fig. 4.3. SEM micrographs of ceramic fracture surfaces showing representative critical flaws outlined by white arrows. (A) Fracture surface of E1; line from flaw corner, $c = 84 \mu\text{m}$ (500x). (B) Fracture surface of E2; measured line represents the semi-minor axis, $a = 44 \mu\text{m}$ (500x). (C) Fracture surface of ES; measured line represents the semi-minor axis, $a = 35 \mu\text{m}$ (600x). (D) Fracture surface of GV; note the tailed fracture markings (top right) pointing to crack origin; measured line represents the semi-minor axis, $a = 55 \mu\text{m}$ (500x).

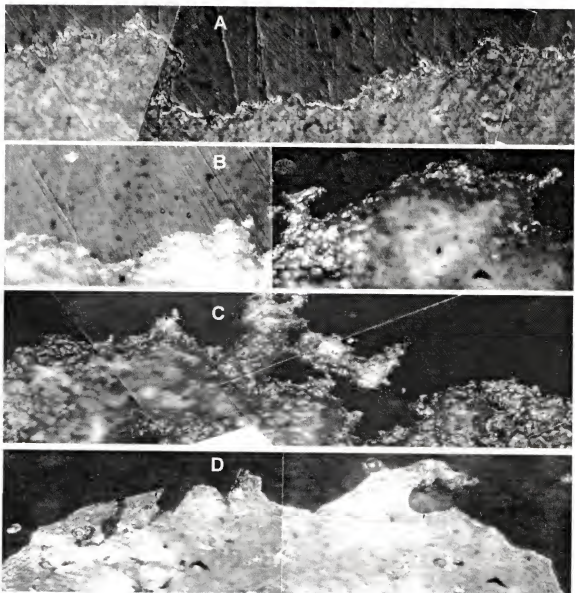


Fig. 4.4. Representative optical microscopy images of E1, E2, ES, and GV specimen replicas, from top (A) to bottom (D), respectively. The Richardson technique was applied to measure the contour lines (coastline collage) and to calculate D^* (400x).

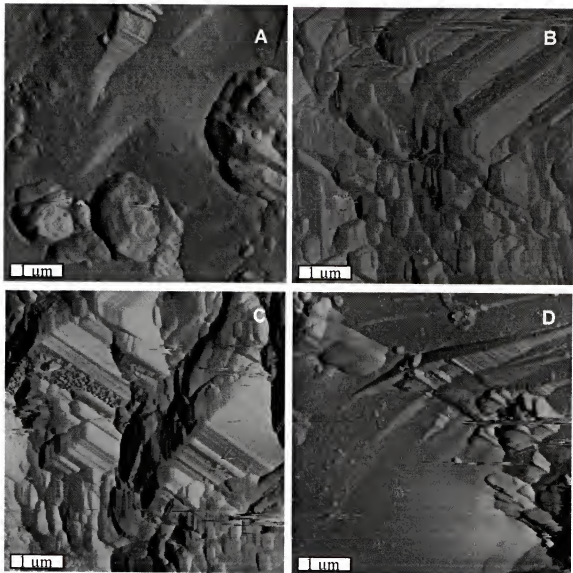


Fig 4.5. Atomic force micrographs of fracture surfaces of E1, E2, ES, and GV specimens, from top A to D, respectively. (Area = 25 μm^2).

4.3. Discussion

Most fracture surface observations yield substantial information about the fracture process and allow calculation of the fracture toughness of the material. In addition, the roughness of the fracture surface gives qualitative information on the extent of crack deflection (Rice, 1984; Faber and Evans, 1983), or other toughening mechanisms (Hill *et al.*, 2000).

The mean K_{IC} values (Table 4.1) were significantly different between E1 and GV ($p \leq 0.05$). However, there were no statistically significant differences in the mean K_{IC} values of the two lithia disilicate-based core ceramics (E2 and ES) ($p \leq 0.05$). These results are in agreement with the mean flexural strength values (Table 3.1), and show a positive relationship with (1) the physical properties, mainly the elastic modulus (Table 2.2); (2) the assumed a_0 values; and (3) the D^* values summarized in Table 4.1.

It is difficult to directly measure the flaw-initiating site, especially in very high-strength, fine-grained ceramics, which is the case for ES and E2, and in cases where failure is caused by poor machining practices. However, where the flaw itself cannot be measured, the region from which the failure occurred can be determined by observing the patterns on the fracture surface (Rice, 1988). This was the case for some multi-layer specimens presented in Chapter 3.

Under certain service and/or environmental conditions, stable crack extension or slow crack growth can occur at stress intensities that are less than the critical value, K_{IC} . Under such conditions, K_I becomes dependent on the crack growth rate (crack velocity V) and, hence, the characteristics of the system. The calculation of K_{IC} in environmental

conditions that promote slow crack growth can lead to erroneous values of K_{IC} because of an incorrect assumption of initial versus final crack size. Nevertheless, the actual value of K_{IC} should not change due to loading rate or test geometry. If the environment degrades the entire material, then the degraded material is essentially a different material. If the environment degrades the local crack, then the crack usually grows and the component is weaker, *i.e.*, it is lower in strength and has a larger final crack size, so the toughness of the unaffected region is still the same. In this study all fracture surfaces were produced inside 37°C distilled water, which could have had some effect on the results. Although the specimens were tested in water, the fast loading rate used during testing prevented any slow crack growth. In addition, previous reports on the fracture toughness using the single edge notched beam (SENB) method performed at room conditions showed comparable results to the ones presented in this study (Höland *et al.*, 2000; Drummond *et al.*, 2000).

Fractal geometry has been used to characterize a number of phenomena, including brittle fracture, since its rediscovery and popularization by Benoit Mandelbrot (1982). The fracture surfaces of both monolithic and granular materials have been shown to have fractal characteristics (Mecholsky, 1989; Tsai and Mecholsky, 1991). The study of fracture surfaces using fractal geometry has led to the observation that tougher materials tend to form more complex, irregular fracture surfaces. In many cases, fractal geometry allows for the complexity of the surface features to be quantified by a single value, the fractal dimension (Mandelbrot *et al.*, 1984; Mecholsky, 1989).

Many different brittle materials have been studied using equation 9 (Mandelbrot *et al.*, 1984; Mecholsky *et al.*, 1989; Bouchaud *et al.*, 1993; Russ, 1994). The K_{IC} versus

$(D^*)^{1/2}$ relationship has been graphed to show that materials from the same class fall on the same straight line (Mecholsky, 1996; Russ, 1994; Hill *et al.*, 2001). This relationship holds for the values obtained in this study (Fig. 4.6).

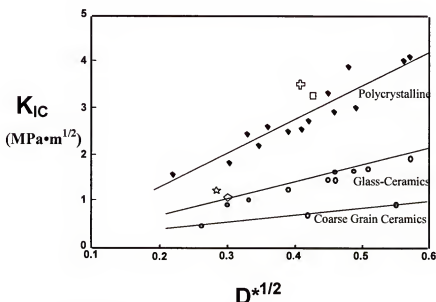


Fig. 4.6. Fracture toughness (K_{IC}) versus fractal dimensional increment (D^*) for material classes including ceramic materials used in this dissertation (E1—star, E2—cross, ES—square, and GV—diamond).

The ceramic, E1, and the glass veneer, GV, lie on the glass-ceramic class of materials, as expected. The other two ceramics are glass-crystal composites and would be expected to behave differently than glass-ceramics. Thus, their positions on the graph can be explained by their behavior being similar to polycrystalline ceramics and composites.

The mean K_{IC} values for E1 and GV agree using both methods of calculation, *i.e.* equations (8) and (9). The mean K_{IC} values of E2 and ES calculated using the fractographic method (equation 8) did not fall into the range of mean K_{IC} values calculated using the fractal approach along with SIA (equation 9). This difference may be

explained by the fine microstructure of these lithia disilicate-based ceramics (Table 2.2, Figs. 2.3 and 2.4) that produce a tortuous coastline on a smaller scale than can be observed using the SIA method to measure D^* . This can be confirmed by using the AFM technique to determine the values for D^* (Fig 4.5 and Table 4.1). The D^* values determined for E2 and ES are in agreement with that ($D^*_{AFM} = 0.17$) obtained in a previous study in which similar microstructures of lithia disilicate-based ceramics were imaged using the atomic force microscope (Thompson, 1995). If the D^*_{AFM} value is used in equation 9 to calculate the K_{IC} of E2 and ES, the resulting mean value range would agree with the mean K_{IC} values calculated using equation 8. These findings also confirmed the recommendation that appropriate scales should be selected to measure D^* (Hill *et al.*, 2001).

The quantity a_0 is a measure of the change in geometry at the crack tip under applied strain. The a_0 value has been shown to be a function of the atomic bonding distances for monolithic materials, and is usually consistent with the reconfiguration of atomic bonds because of applied strain in the material (Mecholsky *et al.*, 1988; Kulawansa *et al.*, 1994). Substituting the relationship for plane stress conditions, $K_{IC} = (2E\gamma)^{1/2}$, into equation 9 gives

$$\gamma = E a_0 D^* / 2 \quad (12)$$

where γ is the fracture energy. It is then possible to relate the macroscopic fracture energy (γ) to the atomic measure of energy per unit volume (E) through the geometry of the fracture surface ($a_0 D^*$). It is hypothesized through the relationship between a_0 and γ that the complex process of bond reconfiguration that occurs during the breaking of atomic bonds in single crystals is the controlling process of brittle fracture and can be

characterized by a_0 (Mecholsky *et al.*, 1988). This is the basis for the assumptions on the a_0 values presented in this study and previous research (Mecholsky *et al.*, 1988; West *et al.*, 1999).

The results of this study confirm the formulated hypothesis that there is a positive correlation between D^* and K_{IC} values. In addition, calculation of fracture toughness using fractal analysis at the appropriate measurement scale is consistent with other techniques. Although fractal analysis can be useful in failure analysis as one of many tools, it is not recommended to use fractal analysis alone as a standard technique for measuring toughness. However, the measurement of D^* on fracture surfaces of failed crowns or bridges can be potentially used to differentiate between processing defects and overload conditions.

Future research should focus on modeling real fracture surfaces using the benefits of high technological imaging, like atomic force microscopy, to verify the observations made in this study at all length scales for other dental materials. It is also important to correlate molecular dynamics (MD) and molecular orbital (MO) modeling with experimental results for calculation of a_0 (West *et al.*, 1999).

CHAPTER 5
EFFECT OF SURFACE TREATMENT ON THE CONTACT ANGLE AND WORK OF
ADHESION OF A LITHIA DISILICATE-BASED CERAMIC

The technology of organosilane coating of inorganic filler particles has improved their bonding to matrix resins. This technology also improves the chemical adhesion of ceramic bonded restorations and resin-bonded ceramic repairs (Bowen, 1963). Several studies have shown the effects of silane coupling agents on ceramic repair effectiveness (Bailey, 1989; Diaz-Arnold and Aquilino, 1989; Pratt *et al.*, 1989; Kupiec *et al.*, 1996; Bouschlicher *et al.*, 1997; Chen *et al.*, 1998b) and on the adhesion to resin cements (Kato *et al.*, 1996; Kamada *et al.*, 1998; Sato *et al.*, 1999). However, the stability of the adhesive bond using silane coupling agents has been challenged (Diaz-Arnold and Aquilino, 1989; Pratt *et al.*, 1989; Kato *et al.*, 1996; Eikenberg and Shurtleff, 1996; Berry *et al.*, 1999).

The adhesion between dental ceramics and resin-based composites is the result of a physico-chemical interaction across the interface between the resin (adhesive) and the ceramic (substrate). The physical contribution to the adhesion process is dependent on the surface topography of the substrate and can be characterized by its surface energy. Alteration of the surface topography, *e.g.*, etching, will result in changes on the surface area and on the wettability of the substrate (Phoenix and Shen, 1995). This may also change the surface energy and the adhesive potential (Jardel *et al.*, 1999b; Panighi and G'Sell, 1993; Attal *et al.*, 1990).

The wetting behavior (wettability) of the resin on the treated ceramic substrate can be characterized using contact angle measurements and surface energy calculations. The wettability of a solid surface by a liquid, *e.g.*, an adhesive, can be characterized by Young's equation (Fig. 5.1):

$$\gamma_{SL} = \gamma_{SV} - \gamma_{LV} \cos\theta \quad (13)$$

where γ_{SV} is the free energy per unit area of the solid surface in equilibrium with vapor, γ_{LV} is the surface tension of liquid balanced with its vapor tension, γ_{SL} is the interfacial energy, and θ is the contact angle. The work of adhesion (W_A) of the liquid drop on a substrate can be expressed by Dupré's equation:

$$W_A = \gamma_{SV} + \gamma_{LV} - \gamma_{SL} \quad (14)$$

Combining equations (13) and (14) yields the Young-Dupré equation:

$$W_A = \gamma_{LV} (1 + \cos\theta) \quad (15)$$

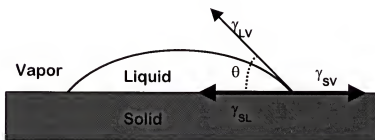


Fig. 5.1. Schematic illustration of a liquid drop on a solid surface with energy vectors and contact angle (θ) as defined by equations 13-15.

An increase in the ceramic surface energy may improve the bond strength between ceramic and resin composite. Contact angle values can be used as an indicator of total surface energy and wettability (Zisman, 1964). Phoenix and Shen (1995) used

dynamic contact angle (DCA) analysis and high-performance liquid chromatography (HPLC) grade water as the probing liquid to quantify the influence of surface treatments on advancing and receding contact angles (θ_a and θ_r) of a feldspathic dental porcelain. They found that chemical and mechanical treatment of porcelain surfaces yield increased total surface areas and increased total surface energies. The use of high purity water as a probing medium is valid for analyzing differences between substrates, such as the effect of etching on dental ceramic surfaces. According to equation 15, W_A is dependent on the surface tension of the liquid, *e.g.*, an adhesive, and its contact angle on the substrate. Thus, the values obtained using water as a probing liquid are not useful to calculate the W_A of resin bonded to ceramic. Instead, an adhesive-equivalent fluid resin should be used as the probing medium to characterize the changes in the wetting behavior of dental ceramics caused by acid etching and silane coating.

The bond strength between resin and ceramic increases with increasing ceramic surface roughness caused by acid etching (al Edris *et al.*, 1990; Della Bona and van Noort, 1995, 1998; Jardel *et al.*, 1999a; Della Bona *et al.*, 2000). Previous studies have shown that etching feldspathic porcelains with hydrofluoric acid increased the surface roughness and the surface area, decreasing the contact angle between porcelain and water (Phoenix and Shen, 1995; Jardel *et al.*, 1999b). Della Bona *et al.* (2000) concluded that the bond strength of ceramic to resin-based composite is affected by the ceramic microstructure as well as the ceramic surface treatment. In addition, a silane coating improved the bond strength values regardless of the ceramic composition or the preceding ceramic surface treatment. Kupiec *et al.* (1996) and Chen *et al.* (1998b) suggested that this improvement in bond strength was caused by the interfacial chemical

bonding between ceramic/silane/resin. Lu *et al.* (1992) suggested that one of the mechanisms through which silane improves bond strength of resin-ceramic systems is by increasing the ceramic surface wettability, thereby improving resin flow. Yet, no scientific evidence was presented to support such an increase in the ceramic surface energy after silane treatment.

The objectives of this study were (1) to test the hypothesis that chemical etching and silane coating of the ceramic surface increase the total surface energy, and (2) to correlate the ceramic surface topography changes to the surface wettability by means of scanning electron microscopy (SEM) and dynamic contact angle (DCA) analysis.

5.1. Materials and Methods

A lithia disilicate-based ceramic, IPS Empress2® (E2), was used in this study (Table 2.1). A description of the etchants, silane and probing liquids used in this study is presented in Table 5.1.

5.1.1. Specimen preparation for Dynamic Contact Angle (DCA) analysis

Eighty flat ceramic plates (8 x 15 x 1.5 mm) were prepared according to manufacturer's directions (Table 2.1, and section 2.1.1.) and polished through 1200 grit SiC paper. They were randomly divided into eight groups of ten specimens each and two experimental procedures were performed. The first experiment comprised Groups 1 - 4 and investigated the effect of probing medium on the contact angle. The second experiment comprised Groups 3-8 and investigated the effect of etching and silane coating on the contact angles using a liquid resin as probing medium. All specimens were rinsed in distilled water and ultrasonically cleaned in ethyl alcohol for 10 min before

surface treatment. The surface treatment and probing medium used for each group are described in Table 5.2. After etching, specimens were rinsed in distilled water for 30 s, and dried with oil-free air before testing or additional surface treatment. Silane was applied with a brush and solvent was allowed to evaporate before any remaining excess was air-blown away.

Normally, the specimens would have to be passed through natural gas flame to burn off organic debris. However, this burn off process is not possible for clinical ceramic specimens and was excluded from this study.

Table 5.1. Materials used in this study

| Material | Description (application time) | Manufacturer |
|--|--|---|
| Ultradent Porcelain Etch (HF etchant) | 9.5% hydrofluoric acid (1 min) | Ultradent Products Inc., South Jordan, UT, USA |
| Porcelain Etchant (APF etchant) | 4% acidulated phosphate fluoride (2 min) | Mirage Dental Products Inc., Kansas City, KS, USA |
| Ultradent Silane | Coupling agent coat applied on ceramic surface | Ultradent Products Inc., South Jordan, UT, USA |
| HPLC water ($\gamma=72.6 \text{ mJ/m}^2$) | High-performance liquid chromatography grade water | Fisher Chemicals, Fair Lawn, NJ, USA |
| Fluid resin ($\gamma=39.7 \text{ mJ/m}^2$) | 65% Bis-GMA 35% TEGDMA | Esschem Inc., Linwood, PA, USA; Aldrich Chemical Company Inc., Milwaukee, WI, USA. |

5.1.2. Dynamic Contact Angle (DCA) Analysis

Changes in the wetting behavior of dental ceramics caused by acid etching and silane coating were studied using the CAHN Dynamic Contact Angle Analyzer (DCA-312, Cahn Instruments, Inc., Cerritos, CA, USA) based on the Wilhelmy Plate Technique. This technique provides values for the advancing and receding contact angles (θ_a and θ_r). The procedure has been described by Phoenix and Shen (1995). Briefly, a specimen is suspended from the balance portion of the instrument while a vertical traveling platform containing a vessel with the probing liquid moves up to immerse the specimen in the liquid. Simultaneously, the balance records weight changes of the specimen as the medium is drawn upward, forming a meniscus. The interfacial surface energy (γ_{SL}) produces a net increase in weight that is recorded by the balance. After an initial increase in weight, the net weight decreases as the specimen continues to travel into the medium, because of the upward force exerted by the probing liquid (buoyancy). Since the square plate specimen has four corners and uniform thickness, the net decrease in weight should be linear with respect to the depth of immersion. This linear relationship allows the computer software to determine the interfacial force at the beginning of immersion. Figure 5.2 shows a typical tensiogram of an HF etched Empress2 specimen as it is being immersed in resin medium and retrieved.

The advancing and receding contact angles (θ_a and θ_r) were calculated by DCA Analyzer based on the following equation:

$$F = \gamma P \cos\theta \quad (16)$$

where F is the specimen force at zero immersion depth (mN), γ is the surface tension

(mJ/m^2), P is the perimeter of the specimen at the liquid-solid interface (m), and θ is the contact angle.

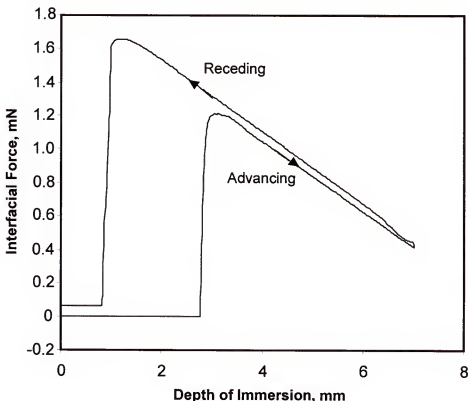


Fig. 5.2. Typical tensiogram of dynamic contact angle measurement. This is the result of a HF treated specimen being immersed in resin medium.

Since small variations in specimen perimeter are critical, but difficult to avoid, each specimen was accurately measured before testing using a digital micrometer (Max-Cal, NSK, Tokyo, Japan) and values were entered in the computer program as specimen parameters in all relevant analyses.

5.1.3. Statistical Analysis

The Student t-test was used to examine the statistical differences between mean values of the advancing and receding contact angles (θ_a and θ_r). One-way ANOVA was

used to examine the interaction between silane coating and etching treatments (APF and HF). Two-way ANOVA was used to examine the effect of probing medium and HF etching on contact angles for Groups 1-4. Two-way ANOVA was also performed for Groups 3-8, for which resin was used as the probing liquid, to determine the effect of etchants and silane, and any interactions between them.

Representative ceramic specimens from Groups 1, 2, 5, and 7 were mounted and coated for SEM examination of the surface topography as described in section 2.1.2.1.

5.2. Results

The surface tension of the prepared liquid resin (Table 5.1) has not been reported previously in the literature. It was observed from 30 specimens that the resin wetted the silane free surface completely on the receding mode, which allowed the calculation of the resin surface tension; the mean value was $39.7 \pm 0.5 \text{ mJ/m}^2$.

Summarized in Table 5.2 are the mean values and standard deviations (SD) of advancing and receding angles (θ_a and θ_r) for all groups tested. Also listed in Table 5.2 are the mean work of adhesion values (mJ/m^2) calculated using equation 15 and the mean θ_a values.

The results of the Student t-test showed that mean θ_a values are consistently higher than values of θ_r ($p \leq 0.0001$) for all groups, except for Group 2 where θ_r is higher than θ_a ($p=0.0528$). Two-way ANOVA was used to analyze the effect of surface treatment (as-polished or etched by HF), and probing medium (water or resin) among Groups 1, 2, 3 and 4. The results show that HF etching produced a significant increase in θ_a ($p \leq 0.001$), but it had no significant effect on θ_r ($p=0.4823$). On the other hand, the

medium exhibited a statistically significant influence on θ_r ($p \leq 0.001$), but not on θ_a ($p = 0.0593$). There were no interactions between the two variables.

Two-way ANOVA was also used to analyze the effect of etching and silanization on the contact angles among Groups 3, 4, 5, 6, 7 and 8, when resin was used as the probing liquid. The results show that etching had a statistically significant influence on θ_a ($p \leq 0.001$), but not on θ_r ($p = 0.5963$). Silanization had a statistically significant influence on both θ_a ($p \leq 0.001$) and θ_r ($p \leq 0.0001$). The analysis also showed that there is a strong interaction between the effects of etching and silanization on θ_a ($p \leq 0.001$).

A series of one-way ANOVA analyses were performed to investigate differences in mean contact angles associated with silanization for each ceramic surface treatment, and the effect of etching for silanization and no silanization. The results showed that without a silane coating (Groups 3-5) each surface treatment consistently yielded lower θ_a and θ_r values ($p \leq 0.0001$) wherein HF etching yielded the lowest θ_a value followed by APF etching and as-polished. Complete wetting on θ_r was observed for all three surface treatments. When a silane coating was applied (Groups 6-8), no significant differences were found between θ_a ($p = 0.2653$) and θ_r ($p = 0.5992$) for all three groups. This means that, after silane application, all surfaces yielded virtually the same surface contact angles that are higher than non-silanated surfaces.

Table 5.2. Mean work of adhesion (WA) and mean values and standard deviation (SD) of advancing and receding contact angles (θ_a and θ_r) for all experimental groups

| Group | Surface | Silane | Treatment | Medium | Work of Adhesion (mJ/m ²) | Contact Angle, Mean \pm SD | |
|-------|-------------|--------|------------|--------|--|------------------------------|-----------------------------|
| | | | | | | Advancing (θ_a) | Receding (θ_r) |
| 1 | As-Polished | No | HPLC water | 135 | 31.2 \pm 4.6 | A* -** | 16.1 \pm 6.3 A* -** |
| 2 | HF | No | HPLC water | 143 | 14.0 \pm 8.3 | B - | 18.3 \pm 7.1 A - |
| 3 | As-Polished | No | Resin | 73.3 | 32.1 \pm 3.0 | A b | 0 B b |
| 4 | HF | No | Resin | 77.4 | 18.5 \pm 2.0 | B c | 0 B b |
| 5 | APF | No | Resin | 76.6 | 21.5 \pm 3.5 | - c | 0 - b |
| 6 | As-Polished | Yes | Resin | 61.9 | 55.9 \pm 2.0 | - a | 44.4 \pm 1.2 - a |
| 7 | HF | Yes | Resin | 63.4 | 53.3 \pm 6.6 | - a | 42.1 \pm 8.6 - a |
| 8 | APF | Yes | Resin | 61.8 | 56.2 \pm 2.5 | - a | 43.7 \pm 2.3 - a |

Note: * Tukey's subsets for Groups 1-4 at $\alpha = 0.05$.

** Tukey's subsets for Groups 3-8 at $\alpha = 0.05$.

The ceramic surface topography analysis showed that HF has a more aggressive etching effect on IPS Empress²® ceramic than APF (Figs. 5.3A and 5.3B), which agrees with previous work (Della Bona *et al.*, 2000). Figure 5.4A depicts a ceramic surface treated with HF followed by silane coating. The chemically attacked surface shown in Fig. 5.3A is completely coated by silane.

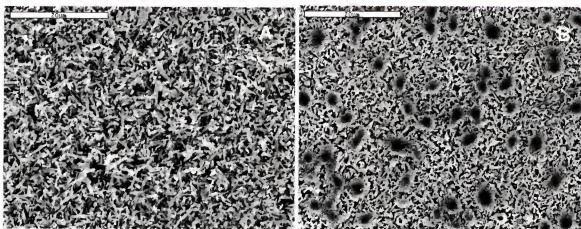


Fig. 5.3. SEM photomicrographs of IPS Empress2®. (A) Etching pattern produced by HF; the lithia disilicate crystals are clearly seen (also shown in Fig. 2.3B). (B) Etching pattern produced by APF; lithia disilicate crystals and some islands of the glass phase (darker areas) can be seen (2000x).

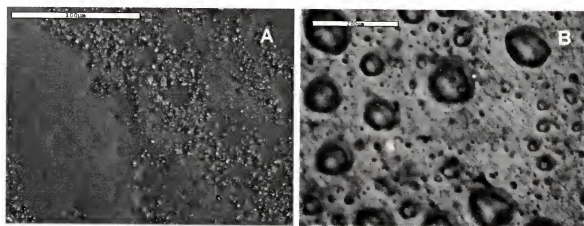


Fig. 5.4. SEM photomicrographs of IPS Empress2®. (A) HF-etched ceramic surface after silane coating; the silane completely fills the surface porosity created by HF producing an amorphous surface (500x). (B) Polished ceramic surface after silane coating; silane "beads up" on treated surface (200x).

5.3. Discussion

To derive Young's equation (13), an ideal solid must be assumed, *i.e.*, one that is chemically homogeneous, rigid and flat on an atomic scale, and does not chemically interact with or adsorb the liquid phase. When these conditions are met, there should be a single unique contact angle ($\theta_a = \theta_r$). One condition that deviates from ideality is the rough surface, which leads to $\theta_a > \theta_r$ (Wenzel, 1936). Since the specimens in this study had various degrees of surface roughness produced by polishing and etching, the differences between θ_a and θ_r were expected, except for Group 2. It has been shown that $\theta_r > \theta_a$ occurs when either the immersion rate is high or the solid surface deforms during the immersion process. Both situations are not likely to occur under the conditions of the present study. Thus, the reason for $\theta_r > \theta_a$ in Group 2 is not readily known without further investigation. For the purpose of this study, only θ_a is relevant in terms of W_A , and the exact reason for $\theta_r > \theta_a$ for Group 2 is beyond the scope of this discussion. Nonetheless, it is important to point out that θ_r values were useful to estimate the surface tension of the resin probing medium. It was observed that the specimen remained coated with resin as it emerged from the medium, which is considered complete wetting of the specimen by the probing medium. The surface tension of the liquid was calculated using equation 16, where $\cos \theta = 1$.

When a probing medium of lower surface tension is used, a lower contact angle should be expected on the same surfaces. However, this is not the case for Groups 1-4. In fact, there is no statistically significant difference between the mean contact angles of the two media used in this study. It is likely that the resin probing medium has a higher viscosity, which means more time is needed to establish equilibrium and it cannot

penetrate into the open porosity as well as HPLC water. In addition, there may be polar interaction between water and ceramic that can exert greater force at the liquid/solid interface. To study the W_A for clinical systems, resin of similar composition to that of the adhesive resin should be used. In this regard, the W_A values calculated for Groups 1 and 2 are not clinically relevant since water is not involved in ceramic-resin adhesion phenomena.

Ceramic surface topography changes produced by etchants exert significant effects on the formation and maintenance of mechanical bonds. Furthermore, the results from some studies suggest that ceramic surface treatments enhance wettability by low viscosity resins through an increase in surface area (al Edris *et al.*, 1990; Phoenix and Shen, 1995; Della Bona and van Noort, 1998; Jardel *et al.*, 1999a and 1999b; Della Bona *et al.*, 2000).

The clinical success of either a repaired ceramic restoration or a resin cemented ceramic restoration will depend on the quality and durability of the bond between the ceramic and the resin. The quality of this bond will depend upon the bonding mechanisms that are controlled in part by the specific surface treatment used to promote micromechanical and/or chemical retention by the substrate (Della Bona *et al.*, 2000). The ceramic surface changes produced by HF and APF (Figs. 5.3A and 5.3B) are similar to those observed in previous studies, where HF produced a rougher surface than APF on IPS Empress2® (Della Bona *et al.*, 2000; Höland *et al.*, 2000). These studies demonstrated that, based on microscopy and bond strength data analyses, treatment of the ceramic surface with APF alone produces an insufficient, inconsistent, micromechanically retentive surface and, as a consequence, yielded the lowest bond

strengths of resin-based composite to IPS Empress® and IPS Empress2®. Treating the ceramic surface with HF produced a substantial, consistent, surface roughness on both ceramics (Della Bona *et al.*, 2000). These ceramic surface changes are consistent with the advancing contact angle results between the ceramic and resin medium reported in this study.

DCA results using resin as the probing liquid showed that untreated specimens (Group 3) displayed a larger mean contact angle (θ_a) than the etched only specimens (Groups 4 and 5). An increase in surface area allows a solid to draw more medium onto its surface and exerts greater interfacial force on the specimen. Consequently, one would expect roughened surfaces to display smaller contact angles (equation 16). A good correlation can be observed between the amount of surface disruption and the resulting contact angle when silane is not used (Groups 1-2, and Groups 3-5). The greater the surface disruption, the lower the contact angle. These results indicate that etching of ceramic by HF and APF reduced the apparent dynamic contact angles caused by the increase in the surface area (Wenzel, 1936).

Silane has been used to enhance bonding between organic adhesives and ceramics or metals in various industries since the 1940's (Plueddemann, 1991). Its use in dentistry has been equally successful in improving the bond strength of ceramic to resin composite and it appears to be the dominant control factor in the chemical bonding of repaired ceramics (Kupiec *et al.*, 1996; Chen *et al.*, 1998b; Jardel *et al.*, 1999a; Della Bona *et al.*, 2000). Silane is known to be hydrophobic, which is the property believed to reduce hydrolytic degradation of the bond. It also may improve wetting of the ceramic surface by the adhesive, since the silane-coated surface is organophilic to the adhesive. However,

the contact angle measurements have proven otherwise. The advancing contact angles increased for all three surface treatments after silane coating (Groups 6-8). This should have been expected since it has been observed that the adhesive resin often "beads up" on a silane treated surface, similar to what is shown in Fig. 5.4B. This phenomenon indicates that the silane treated surface has a lower surface energy than the resin medium. To obtain complete wetting of a surface, the adhesive must initially be of low viscosity and have a surface tension lower than the critical surface tension of the mineral surface (Plueddemann, 1991). Lee (1975) reported that the surface energy of glass surfaces treated with the same silane coupling agent was 36.7 mJ/m^2 and the critical surface energy was 28.0 mJ/m^2 at 20°C . Both values are lower than the surface tension of the resin medium (39.7 mJ/m^2). This explains the high θ_a values observed in this study.

Silane-treated specimens (Groups 6-8) negate the surface roughening effect produced by the two etchants (Groups 4-5). The boiling point of the methacryloxy propyl trimethoxy silane used in this study is $78-81^\circ\text{C}$. It is likely that the silane does not simply coat the surface at the molecular level (silane monolayer), but fills the pores of the roughened etched surfaces (Fig. 5.4A). When this happens, one should expect no apparent differences in the contact angle values. It has been reported that heat treatment of silane coated ceramic surfaces improves the bond strength to resin. This has been attributed to the elimination of water and other contaminants, driving the silane-silica surface condensation reaction toward completion by increasing the number of bond sites available for the reaction, thereby promoting covalent bond formation (Roulet *et al.*, 1995).

For the receding contact angle of Groups 6-8, some residual resin remained on the surface as the specimens emerged from the resin medium yielding low contact angle values. This phenomenon is known as hysteresis.

Silane coating induces lower surface energy of the ceramic and should not enhance bonding by work of adhesion. Several studies have shown that differences in ceramic microstructure and ceramic composition are controlling factors in the development of micromechanical retention produced by etchants, but are not critical for silane bond enhancement (Sheth *et al.*, 1988; Della Bona and van Noort, 1998; Jardel *et al.*, 1999a; Della Bona *et al.*, 2000). These studies have also shown that the silane coating is less evident on rougher ceramic surfaces, *i.e.*, etched leucite-based ceramics. The same silane coating may completely infiltrate more shallow etching patterns in the ceramic, as was the case for E2 in this study. This etching pattern (Fig. 5.3) is produced because the lithia disilicate-based ceramic microstructure has a small crystal size and a volume fraction of about 58% (Table 2.2). However, silane coupling agents bond to Si-OH on ceramic surfaces by condensation reactions and methyl methacrylate double bonds provide bonding to the adhesive. As long as there are adequate Si-OH sites on the ceramic surface, satisfactory bonding should be achieved. Therefore, if the goal is to obtain a thinner silane coating on any ceramic surface, the silane protocol should be based on the ceramic microstructure, silane type, and mechanisms responsible for reducing the silane coating thickness, *i.e.*, heat treatment.

Roughening the ceramic surface by HF etching and silane coating still yields the highest bond strength values (Della Bona *et al.*, 2000) despite the fact that the ceramic has a similar surface energy compared with the other two treatments. This suggests that

the silane might have filled in the ceramic surface irregularities, but it polymerizes along with the adhesive resin providing mechanical retention with the formation of resin tags. It is also possible that the silane and the adhesive resin are miscible because of the similar functional groups involved, which means that the resin would eventually penetrate into the roughened ceramic surface, thereby establishing the mechanical bond. This should be confirmed by examination of resin tag formation on etched and silane treated surfaces. Therefore, the role of silane in promoting adhesion between ceramics and resins is through chemical bonding, while the micromechanical retention is still a major component of the bond.

CHAPTER 6

TENSILE BOND STRENGTH AND APPARENT INTERFACIAL FRACTURE TOUGHNESS OF THE ADHESION ZONE OF CERAMIC-RESIN SYSTEMS

Materials and procedures used to repair fractured ceramic restorations with resin composite or to bond indirect ceramic restorations using resin cement are based on the results of bond strength tests that exhibit wide variability in fracture patterns (Pameijer *et al.*, 1996; Chadwick *et al.*, 1998; Leibrock *et al.*, 1999). The commonly used shear bond test often produces fracture at a distance from the resin-ceramic adhesion zone that may lead to erroneous conclusions on bond quality (Della Bona and Northeast, 1994; Della Bona and van Noort, 1995; Versluis *et al.*, 1997; Chadwick *et al.*, 1998; Della Bona and van Noort, 1998).

To test the integrity of bonded interfaces one can subject a bonded assembly to a variety of loading conditions to control the crack path along the interface or within the interfacial region. Analyses of bond tests have revealed several problems associated with most common test arrangements and suggest a lack of reliability of such measurements in assessing the adhesive behavior of bonded dental materials (Anusavice *et al.*, 1980; Anusavice, 1983; van Noort *et al.*, 1989; Ban and Anusavice, 1990; Della Bona and van Noort, 1995; DeHoff *et al.*, 1995; Versluis *et al.*, 1997).

In the search for a method that produces uniform stress distribution across the interface, investigators have evaluated similar adhesive systems under different bond test configurations (Cardoso *et al.*, 1998; Della Bona and van Noort, 1995; Kitasako *et al.*,

1995; Schreiner *et al.*, 1998). These studies suggested that a tensile bond strength test may be more appropriate to evaluate the bond integrity of adhesive interfaces because of more uniform interfacial stresses. The microtensile test, a tensile bond test with a reduced testing area, was developed as an attempt to eliminate the nonuniform stress distribution at the adhesive interface and to minimize the influence of interfacial defects. This test has been used to measure the bond strength of composite to dental tissues (Sano *et al.*, 1994; Pashley *et al.*, 1995; Schreiner *et al.*, 1998; Phrukanon *et al.*, 1998a; Cardoso *et al.*, 1998; Shono *et al.*, 1999; Pashley *et al.*, 1999) and to ceramics (Della Bona *et al.*, 2000).

The mode of failure is another important aspect of bond strength tests, although this parameter is not commonly reported. A detailed inspection of the fractured surfaces can indicate the failure mode of a bonded assembly. The fracture behavior of adhesive interfaces will depend on the stress level, the flaw distribution, material properties, and environmental effects. Therefore, fracture surface characterization combined with analyses of fracture mechanics parameters are of great importance to understand and predict bonded interface reliability (Chen and Mecholsky, 1993).

A careful interpretation of the failure mode is required to prevent inappropriate conclusions about the utility of the microtensile test and the adhesion zone phenomena. Several dentin bond strength studies using the microtensile test have reported the modes of failure based on SEM observations (Armstrong *et al.*, 1998; Phrukanon *et al.*, 1998a, 1999; Sano *et al.*, 1999; Shono *et al.*, 1999a, 1999b; Yoshikawa *et al.*, 1999; Tunamiharja *et al.*, 2000; Nakajima *et al.*, 2000). These investigators based the failure classification on the substrate location where the fracture occurred. Yet, an understanding of the

fracture mechanics concepts and the analysis of fracture events on the basis of fractography will reduce the risk for data misinterpretation such as the inference that the bond strength must exceed the cohesive strength of the porcelain when the fracture initiates away from the interface. Therefore, the classification of the failure modes based on principles of fractography presented in this study (Fig. 6.3) should assist researchers to correctly interpret the fracture phenomena.

As demonstrated by finite element stress analyses (FEA), the non-uniformity of the interfacial stress distribution generated during conventional tensile and shear bond strength testing may lead to fracture initiation from flaws at the interface or within the substrate at areas of high localized stress (van Noort *et al.*, 1989, 1991; Della Bona and van Noort, 1995). To promote crack initiation within the interfacial zone, an interfacial toughness test can be used.

A previous study of the microtensile bond strength of ceramic to composite required fractography to identify the initial critical flaw and suggested that the interfacial fracture toughness, a more meaningful property than bond strength, could be assessed by applying fracture mechanics principles (Della Bona *et al.*, 2000).

Fracture toughness (K_{IC}) reflects the ability of a material to resist unstable crack propagation. Extensive literature exists on the various techniques used for measuring the fracture toughness of ceramics (Hertzberg, 1996).

Fracture mechanics allows quantification of the relationships between material properties, stress level, the presence of crack-producing flaws, and crack propagation mechanisms. Another way to assess the strength of the bond is to estimate the apparent interfacial fracture toughness (K_A) of the adhesion zone by promoting crack initiation

within the bonding interface. Strictly speaking, measurement of the toughness at the interface using K_{IC} is undefined. However, we can perform tensile tests in which a crack or defect is the source of failure. Therefore, the apparent fracture toughness of the interface can be calculated from the size of the defect and the strength with the appropriate geometric factor. In fact, it is possible to introduce a controlled crack using the indentation technique (Anstis *et al.*, 1981). The apparent fracture toughness value (K_A) reflects the ability of a material to resist unstable crack propagation at the interface (Mecholsky and Barker, 1984; Tam and Pillar, 1993).

The main goals of this part of the overall investigation of interfacial failure were (1) to determine the apparent interfacial fracture toughness (K_A) of the adhesion zone of resin/ceramic systems, and (2) to classify the mode of failure of resin composite bonded to ceramic specimens after microtensile bond strength testing. The specific aims of the present part of this study were (1) to test the hypothesis that the microtensile bond strength of hot-pressed ceramics to composite is controlled by the ceramic microstructure and the ceramic surface treatment, and (2) to test the hypothesis that the bond test design can produce variable fracture surface morphology and fracture origins for the same adhesive interfaces.

6.1. Materials and Methods

A hot-pressed leucite-based ceramic (E1) and a hot-pressed lithia disilicate-based ceramic (E2) were selected for the study (Table 2.1). Fifteen ceramic blocks each of E1 and E2 ceramics were fabricated (Table 2.1, and section 2.1.1.) and polished from 240 through 1200 grit SiC abrasive-coated paper and finished with 1 μm polishing alumina

(Mark V Laboratory, East Granby, CT, U.S.A.). All ceramic blocks were ultrasonically cleaned in distilled water for 10 min after polishing.

The microstructure, composition, some mechanical and physical properties, and the HF-treated ceramic topography of E1 and E2 are described in section 2.2, Table 2.2, and Figs. 2.2, 2.3, and 5.3A.

6.1.1. Resin Composite Characterization

The information reported in this section about the resin composite (Z100) used in this study was provided by the manufacturer (3M Dental Products, St Paul, MN, USA). Z100 is a radiopaque, visible light-cure resin composite restorative material. The filler is not prepared from melted glass, or a mined mineral. It is a synthetic mineral composed of zirconia and silica. The resin consists of a bisphenol-A glycidylmethacrylate (bis-GMA) and triethylene glycol dimethacrylate (TEGDMA). Polymerization of the material is initiated by exposure to visible light (400-500 nm band of the visible spectrum). The average particle size is 0.6 μm , ranging from 0.04 μm to 3.5 μm . The particles are nearly spherical with 66% volume without silane (filler loading weight 84.5 %). The material density is 2.08 gm/cm^3 , and the coefficient of thermal expansion is $17 \times 10^{-6} /^\circ\text{C}$. The material has a reported transverse/flexure strength of 162 MPa, a compressive strength of 448 MPa, and a fracture toughness of $1.03 \text{ MPa}\cdot\text{m}^{1/2}$.

6.1.2. Specimen Preparation for Microtensile Bond Strength Test

The silane and the 9.5% hydrofluoric acid (HF) used in this study are described in Table 5.1. The following ceramic surface treatments were applied to three ceramic blocks of E1 and E2:

Group 1 (E1: HF): HF applied for 1 min, rinsed for 30 s, and dried with oil-free air.

Group 2 (E1: S): a silane coating was applied on the surface, allowed to evaporate for 5 min, and air dried.

Group 3 (E1: HF+S): HF applied for 1 min, rinsed for 30 s, air dried, followed by application of a silane coating.

Group 4 (E2: HF): HF was applied as for Group 1.

Group 5 (E2: S): a silane coating was applied as for Group 2.

Group 6 (E2: HF+S): HF and silane were applied as for Group 3.

A rubber mold (vinyl polysiloxane impression material, Exaflex, GC America Inc., Chicago, IL, USA) was used to stabilize the ceramic block during application of the adhesive (Scotchbond Multi-Purpose Plus Dental Adhesive, lot # 19990323, 3M Dental Products, St. Paul, MN, USA) and resin composite (Z100 restorative resin composite, lot # 19990607, shade A3, 3M Dental Products, St. Paul, MN, USA) on the treated surfaces. The adhesive was applied on the treated ceramic surface and light cured for 10 s. The composite was applied in 2-mm-thick layers and light cured for 40 s. A Coltene Coltolux-4 light curing unit (model C-7915 Coltene/Whaledent Inc., Mahwah, NJ, USA) with light intensity of 430 mW/cm² was used throughout the procedure.

A slow-speed diamond wheel saw (model 650, South Bay Technology Inc., San Clemente, CA, USA) was used to cut the composite/ceramic blocks as shown in Fig. 6.1. The first cut (Fig. 6.1A) through the composite/ceramic block produced slabs of about 1.0 mm in thickness. The sliced block was rotated 90° and a second set of cuts was made to produce the testing bars (Fig. 6.1B). The specimens in the periphery of the ceramic-resin

block were discarded. The bar specimens were examined for flaws using an optical microscope (Model SCW30L, Fisher Scientific, Thailand).

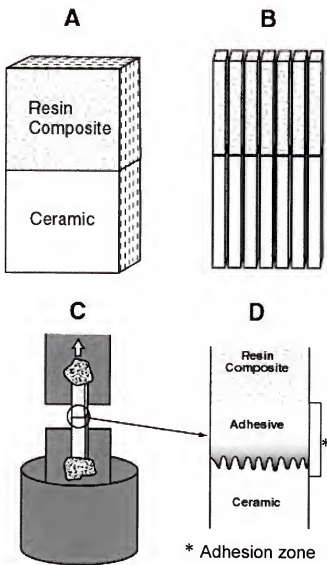


Fig. 6.1. Schematic illustration of specimen preparation sequence for microtensile test. (A) First set of cuts slices the composite/ceramic block to obtain slabs of about 1.0 mm in thickness. (B) The second set of cuts produces bars that were examined for flaws and stored in air environment for 7 days before performing the test. (C) Each bar was fixed to the flat "grips" of a Bencor Multi-T device and loaded to failure in tension. (D) Close-up schematic view of the adhesion zone (adapted from Della Bona *et al.*, 2000).

The specimen rejection criteria included the presence of any flaw or specimen debonding before testing. The specimens were not trimmed after fabrication and cutting. The non-trimming method apparently places less stress on the adhesive zone, since previous microtensile studies using this method were able to measure relatively low bond strengths (Pashley *et al.*, 1999).

Twenty bar specimens for each group were selected at random and stored in air at 23°C and 50% humidity (Hygro-thermometer, Model HT-2106, Interstate Electric, Instrument Division, Lynbrook, NY, USA) for 7 days before indentation and tensile testing. Microhardness indentations were placed to induce controlled cracks into the specimen at the point of the interfacial region in a manner similar to that introduced by Marshall and Lawn (1985).

6.1.3. Interface Indentation

A preliminary study was performed to determine the indentation load (P) necessary to induce controlled cracks. A microhardness tester (Model MO Tukon Microhardness Tester, Wilson Instruments Inc., Binghamton, NY, USA) with a Vickers diamond was used to indent the ceramic/resin interface of specimens prepared as described above (Groups 1-6). Indentation loads ranged from 4.9 N to 29.4 N (Fig 6.2). A 9.8 N indentation load was selected based on the results plotted as $P/c_0^{3/2}$ vs P, where c_0 is the dimension of the radial/median crack (Anstis *et al.*, 1981). In addition, some interfaces (Groups 2 and 5) consistently debonded during the microindentation procedure when loads higher than 9.8 N were used.

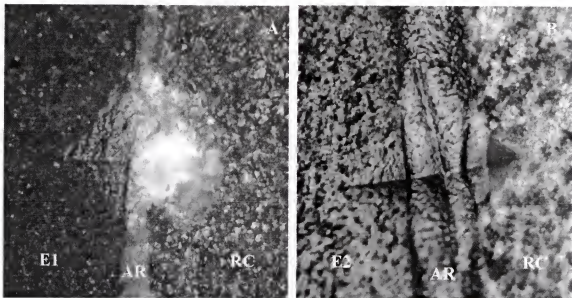


Fig 6.2. Micrographs of Vickers indentation at interface of (A) HF-treated E1 ceramic bonded to the resin composite, RC (Group 1), and (B) HF-treated E2 ceramic bonded to RC (Group 4). The adhesive resin (AR) layer varies in thickness (200x).

Evaluation of K_C , or K_A in this case, requires knowledge of the E / H ratio (Anstis *et al.*, 1981). The elastic modulus (E) and hardness (H) of E1 and E2 are summarized in Table 2.2. The E and H of the adhesive resin (AR) and the resin composite (RC) were determined as described in section 2.1.4., and are as follows: E = 5.9 GPa, and H = 0.3 GPa for the AR; and E = 21 GPa, and H = 1.2 GPa for the RC. It is possible to determine K_C for any well-behaved material to within 30 to 40%. In this context, uncertainties in the value of E / H are relatively unimportant; indeed, since this ratio varies only between 10 and 50 for most ceramics, replacement of the "calibration" constant $\eta(E/H)^{1/8}$ by an averaged quantity $\eta = 0.59$ $[(E/H)^{1/8}] = 0.88$ would add no more than 10% to the error in the K_A evaluation for a material whose elastic/plastic parameters are totally unknown (Chantikul *et al.*, 1981). In the case of this study, the calibration constant for all materials were in agreement with the above value: $\eta_{E1} = 0.83$; $\eta_{E2} = 0.83$; $\eta_{AR} = 0.86$; and $\eta_{RC} = 0.85$.

6.1.4. Microtensile Bond Strength Test

The indentation crack was allowed to grow and stabilize for 24 h in air at 23°C and 50% humidity before testing. Each specimen was attached to the flat grips of the Bencor Multi-T device (Danville Engineering, San Ramon, CA, USA) using cyanoacrylate adhesive (Zapit, Dental Ventures of America Inc., Corona, CA, USA) and loaded to failure in tension at a crosshead speed of 0.5 mm/min using an Instron testing machine (Model 1125, Instron Corp., Canton, MA, USA) (Fig. 6.1C). Because of their small size, the specimen bars could not be “gripped” in the classic sense. They were glued to the Bencor testing apparatus with fast-setting cyanoacrylate that covered the entire surfaces of both ends of the bar to increase the surface bonding area with the stainless steel “grip” (Cardoso *et al.*, 1998; Shono *et al.*, 1999; Della Bona *et al.*, 2000).

The bonding area of all specimens was measured individually immediately after testing (Digimatic caliper, Mitutoyo Co., Kawasaki, Japan) and was used to calculate the bond strength. The size of the bonded cross-sectional area can affect the calculated bond strength. A linear regression analysis was performed to determine if such a relationship exists for the experimental data of this study.

Tensile bond strength data were analyzed statistically using one-way ANOVA and Tukey's HSD test. Weibull analysis was also performed to evaluate the structural integrity of the adhesion zone (refer to section 3.1.5. for Weibull analysis).

Fracture surfaces were examined using optical microscopy and scanning electron microscopy (SEM) to determine the mode of failure, which was confirmed using X-ray dot mapping. Two-dimensional scanning using X-ray dot mapping involves taking the output of the single-channel analyzer and using it to modulate the brightness of the cathode ray tube (CRT) during normal secondary-electron raster scanning. Each X-ray

photon detected appears as a dot on the CRT, with regions of high concentration characterized by a high dot density.

Quantitative fracture surface analysis (fractography) was used to determine the critical crack size (refer to section 4.1.1.) and the fractographic approach (equation 8) was used to calculate the apparent interfacial fracture toughness (K_A). Fractographic principles were also used to determine and classify the mode of failure. The K_A data and the critical crack size values were analyzed statistically using one-way ANOVA and Tukey's HSD test.

6.2. Results

The microstructure, composition, and the etching pattern of E1 and E2 are presented in section 2.2, Table 2.2, and Figs. 2.2, 2.3, and 5.3A. The mean bonding area for all specimens was $1.00 \pm 0.02 \text{ mm}^2$. Linear regression analysis showed that the tensile bond strength values were statistically independent of the size of the bonding area. One-way ANOVA also showed no statistically significant differences in bonding area among the different groups.

The mean tensile strength (σ), standard deviation (SD), mean bonding area (A) and SD, Tukey's test subsets ($\alpha = 0.05$), characteristic strength (σ_{no}), and Weibull modulus (m) values for E1 and E2 ceramics bonded to resin composite are summarized in Table 6.1. The Weibull modulus gives an indication of the reliability of the bond strength, with higher values indicating narrower distribution of the bond strength. Ceramics treated with a silane coating only (Groups 2 and 5) showed the lowest m value for both E1 and E2. Group 1 has the highest m value of all tested groups.

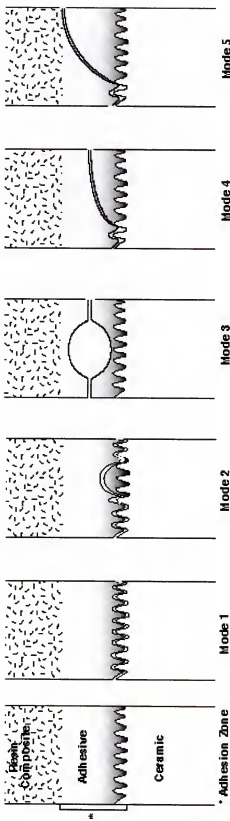


Fig. 6.3. Schematic representation (side view) of the modes of failure for the microtensile bond strength test of ceramic bonded to resin composite. **Mode 1:** Adhesive separation at the ceramic-adhesive resin interface. **Mode 2:** Failure starts at the ceramic-adhesive interface, progresses into the adhesive resin and returns to the interface. **Mode 3:** Failure originates from an internal flaw (penny-shape internal crack). **Mode 4:** Failure starts at the ceramic-adhesive interface and propagates through the adhesive resin. **Mode 5:** Failure starts at the ceramic-adhesive interface, propagates through the adhesive resin to reach the resin composite-adhesive interface.

Table 6.1. Mean bonding area (A) and standard deviation (SD), mean tensile bond strength (σ) values and SD, Tukey's test subsets ($\alpha = 0.05$), characteristic strength (σ_{no}), and Weibull modulus (m) values for E1 and E2 ceramics bonded to resin

| Groups | A \pm SD (mm ²) | $\sigma \pm$ SD (MPa) | Tukey subsets | σ_{no} (MPa) | m |
|--------------|-------------------------------|-----------------------|---------------|---------------------|-----|
| (1) E1: HF | 1.01 \pm 0.02 | 26.4 \pm 5.0 | B | 27.3 | 7.8 |
| (2) E1: S | 1.01 \pm 0.02 | 21.4 \pm 7.6 | C | 24.1 | 2.6 |
| (3) E1: HF+S | 1.00 \pm 0.01 | 24.0 \pm 5.0 | B C | 25.9 | 4.9 |
| (4) E2: HF | 1.01 \pm 0.02 | 31.9 \pm 8.6 | A | 35.7 | 4.0 |
| (5) E2: S | 1.00 \pm 0.01 | 11.4 \pm 6.4 | D | 13.5 | 1.4 |
| (6) E2: HF+S | 0.99 \pm 0.02 | 28.1 \pm 5.4 | A B | 29.9 | 5.2 |

Two-way ANOVA showed that similar surface treatments were associated with significantly different bond strengths for E1 and E2 ceramics ($p \leq 0.0001$). For each surface treatment, the mean tensile bond strength was higher for the lithia-based ceramic (E2) than for the leucite-based ceramic (E1), except for the groups treated only with a silane coating (Groups 2 and 5). The application of silane weakened the bond strength of the etched ceramics. The silane-treated specimens (Groups 2 and 5) showed the lowest mean tensile bond strength and the highest standard deviations. In addition, some specimens treated only with a silane coating debonded during the specimen preparation procedure. Thus, they satisfied the rejection criteria and were not considered for the random selection process of specimens for Groups 2 and 5.

Table 6.2. Mean critical flaw size (c) and SD, crack origin, modes of failure, K_A ($\text{MPa} \cdot \text{m}^{1/2}$) and SD, and Tukey's test subsets ($\alpha = 0.05$) for E1 and E2 ceramics bonded to resin

| Groups | $c \pm \text{SD}$ (μm) | c origin (%) | Failure Mode (%) | $K_A \pm \text{SD}$ ($\text{MPa} \cdot \text{m}^{1/2}$) | Tukey subsets |
|--------------|--|------------------------------------|------------------------|--|------------------|
| (1) E1: HF | 83 ± 27 | SC(50); SCI(40); CF(10) | 4(60); 2(30); 5(10) | 0.30 ± 0.07 | B |
| (2) E1: S | 79 ± 23 | SC(70); CF(10); SCI(10); IF(10) | 5(60); 4(30); 3(10) | 0.24 ± 0.06 | C |
| (3) E1: HF+S | 77 ± 21 | SC(70); SCI(30) | 4(60); 2(40) | 0.26 ± 0.07 | B C |
| (4) E2: HF | 122 ± 82 | SC(50); SCI(40); CF(10) | 5(60); 4(30); 2(10) | 0.40 ± 0.08 | A |
| (5) E2: S | 113 ± 110 | SC(90); CF(10) | 4(60); 2(40) | 0.13 ± 0.07 | D |
| (6) E2: HF+S | 62 ± 10 | SC(100) | 4(60); 5(40) | 0.27 ± 0.06 | B C |

Modes of failure correspond to Fig. 6.3.

Crack origin: SC: semicircular crack; SCI: indentation semicircular crack;
IF: internal flaw; CF: corner flaw

The mean critical flaw size (c) and SD, crack origin, modes of failure, K_A ($\text{MPa} \cdot \text{m}^{1/2}$) and SD, and Tukey's test subsets ($\alpha = 0.05$) for E1 and E2 ceramics bonded to resin are summarized in Table 6.2. The mean critical flaw size varied from 62 μm (Group 6) to 122 μm (Group 4). The mean "c" value was not significantly different for Groups 1, 2, 3, and 5. Semicircular cracks were the crack origins in 100% of Group 6 specimens and 90% of Group 5 specimens. Semicircular cracks that originated from the indentation were found to be the critical flaw for 40% of the specimens in Groups 1 and 4, 30% in Group 3, and 10% of specimens in Group 2.

SEM analysis, complemented by x-ray dot mapping, revealed that all fractures occurred within the adhesion zone (Figs. 6.4, 6.5, and 6.6). The “adhesion zone” is defined as “the region in which the adhesive interacts with the two substrates to promote bonding” (Della Bona *et al.*, 2000). More specifically, the adhesion zone in this study consists of the following: (1) the interfacial region between the adhesive and the resin composite within which molecular interaction and chemical bonding occur between the two materials; (2) the adhesive; and (3) the interfacial region between the adhesive and the dental ceramic, including the surface region treated with the etchant and/or coated with silane such that micromechanical and/or chemical bonding occurs (Fig. 6.1D).

Examination of the fracture surfaces showed no bulk fracture of either the resin composite or the dental ceramics. X-ray dot maps of these surfaces confirmed that they contained elements from the adhesive/ceramic interface (Fig 6.4) and from both adhesive interfaces of the adhesion zone (Figs 6.5 and 6.6), characterizing fracture mode 5.

The mode of failure was determined using fractographic principles and classified as shown in Fig. 6.3 and Table 6.2. Representative SEM micrographs of the modes of failure found in this study are shown in Figs. 6.7 and 6.8. The purely adhesive failure (Mode 1) was not found in this study. Mode 4 was the predominant (60%) type of failure in Groups 1, 3, 5, and 6 (Figs. 6.3, 6.8A, and 6.8B). Mode 5 was the dominant type of failure in 60% of the specimens in Groups 2 and 4 (Figs. 6.3, 6.8C, and 6.8D). Mode 3 (internal flaw) was the mode of failure in two specimens of Group 2 (Figs. 6.3, 6.7C, and 6.7D).

The mean interfacial fracture toughness (K_A) value for Group 4 was significantly higher than that for all the other groups ($p \leq 0.0001$). There were no significant

differences in mean K_A values among Groups 1, 3, and 6. The mean K_A values of Group 5 were significantly lower than those of all the other groups.

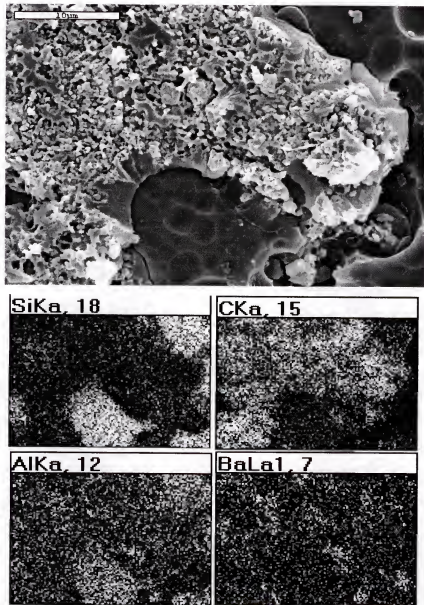


Fig. 6.4. SEM image (top) and X-ray elemental maps of fracture surface of Group 1. The label at the top of X-ray maps indicates the elements and their intensity. Note the adhesion zone fracture starting along the ceramic/adhesive interface by crack formation within the remaining glassy phase that was weakened by the etching process (Failure Mode 4).

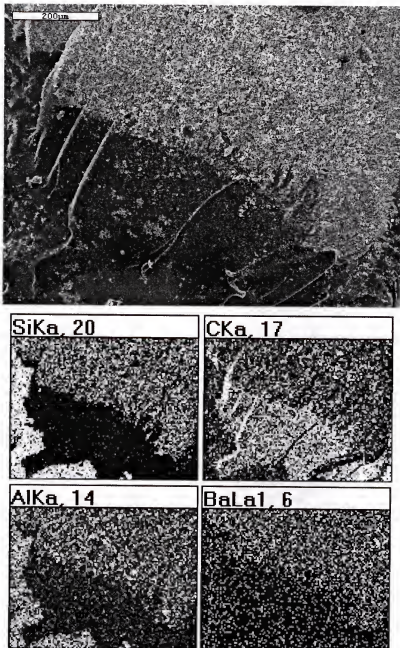


Fig. 6.5. SEM image (top) and X-ray elemental maps of fracture surface of Group 2. The label at the top of X-ray maps indicates the elements and their intensity.

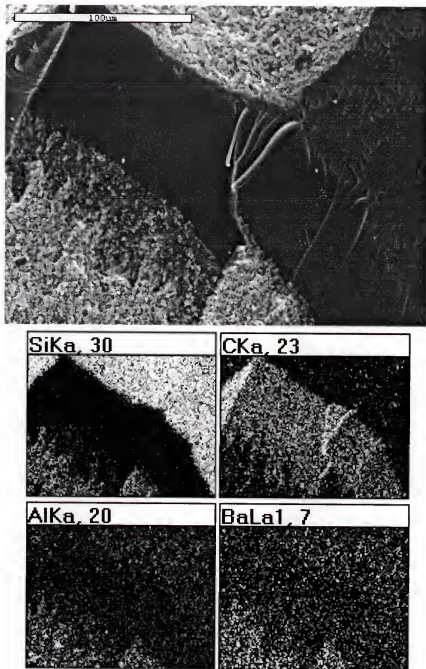


Fig. 6.6. SEM image (top) and X-ray elemental maps of fracture surface of Group 8. The label at the top of X-ray maps indicates the elements and their intensity. Note that the fracture pattern is similar to that in Fig. 6.5 (Failure Mode 5).

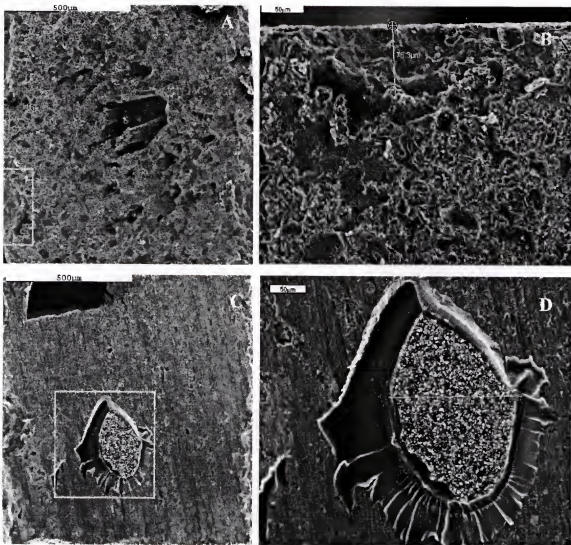


Fig. 6.7. Representative SEM micrographs of the modes of failure found in this study and schematically illustrated in Fig. 6.3. (A) semicircular flaw is the crack origin (in the white box); the adhesive resin island in the middle of the fracture surface represents what has been characterized as Failure Mode 2 (80x). (B) Enlargement of the white box area of (A) showing the measurement of the crack semi-minor axis ($a = 76 \mu\text{m}$) (300x). (C) Internal flaw is the crack origin characterizing Failure Mode 3 (80x). (D) Enlargement of the white box area of (C) showing the measurement of the flaw minor axis ($2b = 175 \mu\text{m}$) (250x).

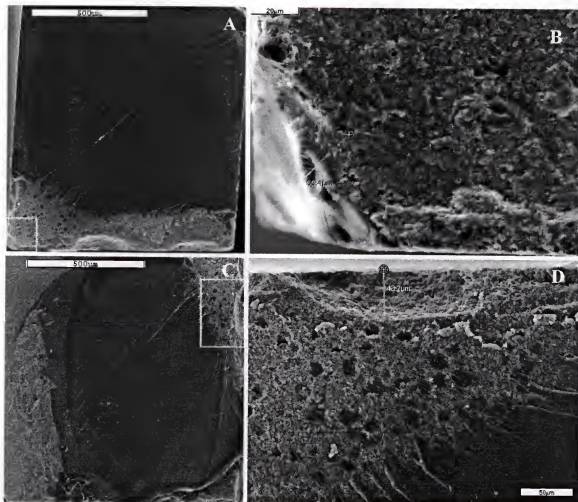


Fig 6.8. SEM micrographs of the modes of failure found in this study and schematically illustrated in Fig 6.3. (A) Failure starts at the ceramic-adhesive interface as a corner flaw (in the white box) and propagates through the adhesive resin (mode 4) (80x). (B) Enlargement of white box area of (A) showing the measurement of "c" (55 μm) (750x). (C) Failure starts at the ceramic-adhesive interface (white box), propagates through the adhesive resin to reach the resin composite-adhesive interface (left), characterizing Failure Mode 5 (80x). (D) Enlargement of white box area of (C) showing a semicircular crack resulting from indentation (white arrows); measurement line is "a" (44 μm) (370x).

6.3. Discussion

Conventional shear and tensile bond tests have generally been used to evaluate fractured ceramic restorations that were repaired with resin composite (Della Bona and van Noort, 1995; Pameijer *et al.*, 1996; Chadwick *et al.*, 1998; Leibrock *et al.*, 1999). However, the most commonly used shear bond test often produces fracture away from the adhesion zone (Della Bona and van Noort, 1995; Versluis *et al.*, 1997; Chadwick *et al.*, 1998). Such failures of the substrate prevent measurement of interfacial bond strength and limit further improvements in bonding systems.

Several studies have identified the nonuniform stress distributions along bonded interfaces. These variable stress patterns suggest that a standardized research protocol may address only a part of the problem (Anusavice *et al.*, 1980; van Noort *et al.*, 1989, 1991; DeHoff *et al.*, 1995; Della Bona and van Noort, 1995; Versluis *et al.*, 1997; Sudsangiam and van Noort, 1999). The nonuniform interfacial stress distribution generated for conventional tensile and shear bond strength tests initiates fractures from flaws at the interface or in the substrate in areas of high stress concentration.

The microtensile bond test was developed in an attempt to eliminate the nonuniform stress distribution within the adhesion zone by using the traditional dumbbell-shaped specimen design (Sano *et al.*, 1994). The reduction in the number and size of defects in the adhesive zone is thought to decrease bulk cohesive failures and increase the tensile bond strengths, regardless of the cross-sectional shape (Sano *et al.*, 1994; Pashley *et al.*, 1995, 1999; Phrukanon *et al.*, 1998b).

The non-trimming method to obtain specimens for the microtensile test used in this study places less stress on the adhesion zone (Pashley *et al.*, 1999). As no specimen

finishing is necessary, this method also avoids areas of stress concentration produced by polishing materials of different hardness values.

Effective etching of the ceramic surface is considered an essential step for the clinical success of indirect ceramic bonded restorations and direct repaired ceramic prostheses. Structural and surface analyses of etched ceramics have shown that different etching patterns are created according to the concentration, application time, and type of etchant (al Edris *et al.*, 1990; Kupiec *et al.*, 1996; Chen *et al.*, 1998a, 1998b; Della Bona and van Noort, 1998; Jardel *et al.*, 1999; Della Bona *et al.*, 2000).

The clinical success of a repaired ceramic restoration will depend on the quality and durability of the bond between the ceramic and the resin composite. The quality of this bond will depend upon the bonding mechanisms that are controlled in part by the specific surface treatment to promote micromechanical and/or chemical retention with the substrate. Similar ceramic surface changes produced by HF were also observed in previous studies (al Edris *et al.*, 1990; Chen *et al.*, 1998b; Della Bona and van Noort, 1998; Jardel *et al.*, 1999a). Treating the ceramic surface with HF produced a substantial, consistent, surface disruption of both E1 and E2 ceramics (Figs. 2.2B, 2.3B, and 5.3A). The use of silane weakened the bond strength for both ceramics. In addition, the silane treated only specimen groups showed a high standard deviation for the mean tensile bond strength values, and some silane treated interfaces debonded during the specimen preparation procedure. Therefore, these results suggest that differences in ceramic microstructure and ceramic composition are controlling factors in the development of micromechanical retention produced by etching.

For each surface treatment, the mean tensile bond strength was higher for the lithia-based ceramic (E2) than for the leucite-based ceramic (E1), except for the silane treated groups. Silane reduced the bond strength independent of the ceramic composition or the surface treatment (as-polished or HF). It has been shown (Fig. 5.4) that the Ultradent silane coupling agent “beads up” on ceramic surfaces. The internal flaw shown in Figs. 6.7C and 6.7D could be the result of a remaining silane agglomerate that prevented the adhesive resin from contacting the ceramic surface, creating a no-bond area at the interface.

The microstructural difference between etched E1 and E2 ceramics was a major controlling factor in the quality of adhesive bonding when HF was used. The structural integrity of the adhesion zone defined by Weibull parameters revealed the highest modulus for E1 ceramic specimens treated with HF, which is in agreement with the results of previous research (Della Bona *et al.*, 2000). The strength values obtained using the microtensile test can be a reliable indicator of the composite-ceramic bond quality since all fractures occurred within the adhesion zone. In addition, the microtensile test produced variable fracture surface morphology and fracture origins for the same adhesive interfaces within the adhesion zone. However, each ceramic surface treatment produced a trend for the failure modes (Table 6.2, Fig 6.3). Adhesive failures (mode 1) did not occur in this study. Yet, a previous study revealed that 100% of the E1 and E2 ceramic specimens treated with APF failed in mode 1 (Della Bona *et al.*, 2000). HF-treated specimens produced failures that started at the ceramic-adhesive interface and propagated through the adhesive (mode 4), then either reached the adhesive-composite interface (mode 5) or returned to the ceramic-adhesive interface (mode 2). Compared with optical

microscopy observations, a thorough SEM characterization of the fracture surfaces and compositional analysis through the use of X-ray dot maps can yield a more consistent and complete description of the fracture process and modes of failure.

It would be more appropriate to analyze the energy per unit crack surface area, G_{IC} , that is required for a crack to advance in the bond plane, rather than to compare the stress intensity factor (K_{IC}) with bond strength. Normally, in order to maintain equal compliances of the specimen halves, *i.e.* for the two halves to have equal strain energy, most of the interfacial fracture toughness tests require $E_1 d_1^3 = E_2 d_2^3$, where E_1 is the elastic modulus of the first specimen half (ceramic), d_1 is the depth of the ceramic rectangular segment, E_2 is the elastic modulus of the composite half, and d_2 is the depth of the composite rectangular segment (Mecholsky and Barker, 1984; Tam and Pilliar, 1993). Since a uniaxial tensile test (microtensile test) was used to assess the fracture toughness of the adhesive interface between the resin composite and ceramic, there was no need for preparing specimens with balanced compliance for the two materials.

The toughness relative to the strain energy release rate (G_{IC}) is an accurate measure of the resistance of the bond to fracture since G_{IC} represents the relative energy required to create the new surfaces. However, the fracture toughness in the form of the stress intensity factor is really a pseudocritical stress-intensity factor, *i.e.*, the apparent toughness, considering the fact that it is difficult to define a stress intensity at an interface and one must determine an effective modulus for the two systems (Mecholsky and Barker, 1984).

Nevertheless, a positive relationship was found between the mean tensile bond strength (σ) values and the mean K_A values. The mean σ and K_A values followed the

ranking for both ceramics (E1 and E2), that is, the values increased in the order, HF-treated > HF+S-treated > S-treated.

This study suggests that the tensile bond strength and the apparent interfacial fracture toughness of ceramic bonded to composite is affected by the ceramic microstructure and the ceramic surface treatments. The definition of the adhesion zone is critical to classify the modes of failure, which should be an integral component of all failure analyses. Since all fractures occurred within the adhesion zone, the microtensile test may be preferable to conventional shear or flexural tests as an indicator of composite-ceramic bond quality. A careful microscopic analysis of the fracture surfaces and X-ray dot maps can produce a more consistent and complete description of the fracture process and interpretation of the "mixed modes of failure". Thus, the quality of the bond should not be assessed based on bond strength data alone. The mode of failure and fractographic analyses should provide important information leading to predictions of clinical performance limits, which is the ultimate test of any adhesive system. Future studies should also focus on optimum surface treatment conditions because of the poor adhesion associated with silane coating ceramics, the most commonly used ceramic coupling agent.

CHAPTER 7 CONCLUSIONS

The mean values of the ceramic properties reported in this study are summarized in Table 7.1. The standard deviation and other statistical results of the mean values shown in Table 7.1 are included in previous tables (Tables 3.1 and 4.1).

Table 7.1. Mean values of the properties of a hot-pressed leucite-based ceramic (IPS Empress® - E1), two hot-pressed lithia disilicate-based ceramic (IPS Empress2® - E2, and experimental - ES), and a glass veneer (IPS Empress2® - GV)

| Material Properties | E1 | E2 | ES | GV |
|---|-----------------------|-----------------------|-----------------------|-----------------------|
| Volume fraction (V_v) | 0.44 | 0.58 | 0.52 | |
| Area of crystals (\bar{A}) | $18.12 \mu\text{m}^2$ | $0.42 \mu\text{m}^2$ | $0.20 \mu\text{m}^2$ | |
| Density (ρ) | 2.47 g/cm^3 | 2.51 g/cm^3 | 2.56 g/cm^3 | 2.53 g/cm^3 |
| Elastic modulus (E) | 86 GPa | 96 GPa | 96 GPa | 65 GPa |
| Poisson's ratio (ν) | 0.27 | 0.26 | 0.24 | 0.23 |
| Vickers hardness (H) | 5.9 GPa | 6.3 GPa | 6.3 GPa | 5.4 GPa |
| Flexure strength (σ) (4-point bend in water) | 84.5 MPa | 215 MPa | 239 MPa | 63.8 MPa |
| Characteristic strength (σ_{no}) | 91.3 MPa | 231 MPa | 252 MPa | 65.7 MPa |
| Weibull modulus (m) | 5.2 | 5.4 | 7.2 | 14.1 |
| Fractal Dimensional | 0.06 _{SIA} | 0.11 _{SIA} | 0.12 _{SIA} | 0.09 _{SIA} |
| Increment (D^*_{SIA} and D^*_{AFM}) | 0.08 _{AFM} | 0.17 _{AFM} | 0.19 _{AFM} | 0.09 _{AFM} |
| K_{IC} ($\text{MPa}\cdot\text{m}^{1/2}$) | (D^*_{SIA}) | $(1.0 - 1.9)$ | $(1.4 - 2.9)$ | $(1.5 - 3.0)$ |
| Using E ($a_0 D^*_{AFM}$) | $[D^*_{AFM}]$ | $[1.1 - 2.1]$ | $[1.8 - 3.6]$ | $[1.9 - 3.7]$ |
| K_{IC} ($\text{MPa}\cdot\text{m}^{1/2}$) Using $Y_{\sigma_f} c^{1/2}$ | | 1.3 | 3.4 | 3.1 |
| | | | | 0.77 |

As expected, there is a positive correlation between the elastic modulus (E), hardness (H), flexure strength (σ), and fracture toughness (K_{IC}) for the four ceramics studied (E1, E2, ES, and GV). This study also revealed a positive correlation between the microstructural features and the fracture patterns for the two lithia disilicate-based ceramics (E2 and ES), that is, the smaller the crystal area, the higher the fractal dimensional increment (D^*). In the case of E1, the leucite crystals agglomerate in clusters, which are responsible for the high thermal expansion, and cracks around these clusters are often observed (Fig. 2.2A) (Mackert *et al.*, 1986). The clusters act as crack propagation barriers; however, the existing cracks around them offer an easier path for crack propagation. As a result, the D^* and toughness values are lower for E1 than the two lithia disilicate-based ceramics (Figs. 4.4 and 4.5). These results agree with previous research that demonstrated the role of microstructure in toughening of glass-ceramics and ceramics (Mecholsky, 1981; Lawn, *et al.*, 1994).

A graph of fracture toughness (K_{IC}) versus fractal dimensional increment (D^*) (Fig. 4.6) shows that these materials lie on the lines corresponding to their material classes. The ceramic, E1, and glass veneer, GV, lie within the glass-ceramic class of materials, as expected. The other two ceramics are glass-crystal composites and would be expected to behave differently than glass-ceramics. Thus, their positions on the graph for polycrystalline ceramics can be explained by their behavior being similar to polycrystalline ceramics and particulate composites.

The Weibull modulus (m) is a measure of the distribution of critical flaws. As the Weibull moduli are similar in most cases (except for GV) and the experimental results show that the average crack sizes are the same, a crack size difference cannot explain the

strength differences. Thus, the differences in flexure strength can be attributed to the differences in toughness that, in turn, are related to the way the materials are processed.

The mean flexural strength and Weibull modulus of the ES ceramic (monolithic) are similar to those of the two veneered ES ceramic structures (multilayered specimens). Fracture analysis also showed similar results for these three structures. Therefore, one concludes that the structural reliability of veneered core ceramic is controlled primarily by the properties of the core ceramic.

The clinical success of either a repaired ceramic restoration or a resin cemented ceramic restoration will depend on the quality and durability of the bond between the ceramic and the resin. The quality of this bond will depend upon the bonding mechanisms that are controlled in part by the specific surface treatment used to promote micromechanical and/or chemical retention with the substrate (Della Bona *et al.*, 2000). The ceramic surface changes produced by HF and APF (Figs. 5.3A and 5.3B) are similar to those observed in previous studies, in which HF produced a rougher surface than APF (Della Bona *et al.*, 2000; Höland *et al.*, 2000). Based on microscopy and bond strength data analyses, treating the ceramic surface with APF alone produces an insufficient, inconsistent, micromechanical retentive surface and, as a consequence, produces the lowest bond strengths of resin bonded to ceramic. Treating the ceramic surface with HF produced a substantial, consistent, surface roughness on E1 and E2. The microstructural difference between etched E1 and E2 ceramics was a major controlling factor on the quality of adhesive bonding when HF was used. The evaluation of the structural integrity of the adhesion zone by Weibull analysis revealed the highest Weibull modulus for E1 ceramic specimens treated with HF, which is in agreement with the results of previous

research (Della Bona *et al.*, 2000). These results suggest that differences in ceramic microstructure and ceramic composition are controlling factors in the development of micromechanical retention produced by etching. These ceramic surface changes are consistent with the advancing contact angle results between the ceramic and resin medium reported in this study (Table 7.2).

The mean values of properties of the adhesion zone of E1 and E2 bonded to resin reported in this study are summarized in Table 7.2. The standard deviation and other statistical aspects of the mean values shown in Table 7.2 are included in previous Tables.

Table 7.2. Mean values of advancing contact angle (θ_a), work of adhesion (W_A), tensile bond strength (σ), Weibull modulus (m), critical crack size (c), and apparent interfacial fracture toughness (K_A) for a hot-pressed leucite-based ceramic (IPS Empress® - E1) and a hot-pressed lithia disilicate-based ceramic (IPS Empress2® - E2) treated with hydrofluoric acid (HF), acidulated phosphate fluoride (APF), and/or silane coupling agent (S)

| Ceramic: Treatment | θ_a (degrees) | W_A (mJ/m ²) | σ (MPa) | m | c (μ m) | K_A (MPa \cdot m ^{1/2}) |
|--------------------|-------------------------|-------------------------------|-------------------|-----|-------------------|--|
| E2: HF | 18.5 | 77.4 | 31.9 | 4.0 | 122 | 0.4 |
| E2: APF | 21.5 | 76.6 | - | - | - | - |
| E2: S | 55.9 | 61.9 | 11.4 | 1.4 | 113 | 0.13 |
| E2: HF+S | 53.3 | 63.4 | 28.1 | 5.2 | 62 | 0.27 |
| E2: APF+S | 56.2 | 61.8 | - | - | - | - |
| E1: HF | 33.7 | 72.6 | 26.4 | 7.8 | 83 | 0.3 |
| E1: S | 51.0 | 64.7 | 21.4 | 2.6 | 79 | 0.24 |
| E1: HF+S | 47.2 | 66.7 | 24.0 | 4.9 | 77 | 0.26 |

The strength values obtained using the microtensile test (chapter 6) can be a reliable indicator of the composite-ceramic bond quality since all fractures occurred within the adhesion zone. In addition, the microtensile test produced variable fracture

surface morphology and fracture origins for the same adhesive interfaces within the adhesion zone. However, each ceramic surface treatment produced a trend for the failure modes (Table 6.2, Fig 6.3).

Examining the contact angle data of the adhesive resin to ceramic, one concludes that silane treated specimens negated the surface roughening effect produced by the two etchants (HF and APF), inducing lower surface energy of the ceramic and, therefore, reducing bonding through work of adhesion.

There is a positive correlation between the work of adhesion (W_A), the tensile bond strength (σ), and the apparent interfacial fracture toughness (K_A), that is, the higher the mean W_A value, the higher the mean σ and K_A values. The relation between the W_A and K_A is shown in Fig. 7.1.

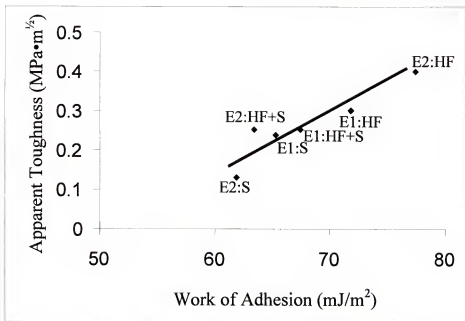


Fig. 7.1. The apparent interfacial fracture toughness (K_A) versus the work of adhesion (W_A) of an adhesive resin to a lithia disilicate-based ceramic (E2) and a leucite-based ceramic (E1) treated with hydrofluoric acid (HF) and/or silane coupling agent (S).

This study suggests that (1) the tensile bond strength and the apparent interfacial fracture toughness of ceramic bonded to resin are affected by the ceramic microstructure and the ceramic surface treatments; (2) the definition of the adhesion zone is critical to classify the modes of failure, which should be an integral component of all failure analyses; (3) the microtensile test may be preferable to conventional shear or flexural tests as an indicator of composite-ceramic bond quality, since all fractures occurred within the adhesion zone; and (4) a careful microscopic analysis of the fracture surfaces and a x-ray dot map can produce a more consistent and complete description of the fracture process and interpretation of the modes of failure.

The mode of failure and fractographic analyses should provide important information, *i.e.*, fracture origin, leading to predictions of relative survival times. Thus, the quality of the bond should not be assessed based on bond strength data alone. Future studies should also focus on optimum surface treatment conditions because of the poor adhesion associated with the silane coated ceramics, the most commonly used ceramic coupling agent. In addition, the W_A should also be determined using the sessile drop technique (Schrader, 1999) to compare with and validate the results obtained using the DCA Analyzer. In addition, the clinical relevance of failure controlling mechanisms must be validated through randomized, controlled clinical trials.

APPENDIX A
FLEXURAL STRENGTH DATA (CHAPTER 3)

Group 1 (E1)

| Specimen number | Load (N) | Flexural Strength (MPa) |
|-----------------|----------|-------------------------|
| 1 | 29.4 | 102.1 |
| 2 | 18.6 | 64.6 |
| 3 | 24.5 | 85.1 |
| 4 | 29.4 | 102.1 |
| 5 | 25.5 | 88.5 |
| 6 | 29.4 | 102.1 |
| 7 | 21.6 | 74.9 |
| 8 | 22.5 | 78.3 |
| 9 | 20.6 | 71.5 |
| 10 | 20.6 | 71.5 |
| 11 | 28.4 | 98.7 |
| 12 | 29.4 | 102.1 |
| 13 | 20.6 | 71.5 |
| 14 | 17.6 | 61.2 |
| 15 | 25.5 | 88.5 |
| 16 | 25.5 | 88.5 |
| 17 | 21.6 | 74.9 |
| 18 | 28.4 | 98.7 |
| 19 | 29.4 | 102.1 |
| 20 | 18.6 | 64.6 |

Group 2 (E2)

| Specimen number | Load (N) | Flexural Strength (MPa) |
|-----------------|----------|-------------------------|
| 1 | 56.8 | 197.4 |
| 2 | 70.6 | 245.0 |
| 3 | 65.7 | 228.0 |
| 4 | 56.8 | 197.4 |
| 5 | 64.7 | 224.6 |
| 6 | 67.6 | 234.8 |
| 7 | 80.4 | 279.0 |
| 8 | 43.1 | 149.7 |
| 9 | 53.9 | 187.1 |
| 10 | 80.4 | 279.0 |
| 11 | 44.1 | 153.1 |
| 12 | 77.4 | 268.8 |
| 13 | 74.5 | 258.6 |
| 14 | 44.1 | 153.1 |
| 15 | 56.8 | 197.4 |
| 16 | 60.8 | 211.0 |
| 17 | 48.0 | 166.7 |
| 18 | 63.7 | 221.2 |
| 19 | 62.7 | 217.8 |
| 20 | 64.7 | 224.6 |

Group 3 (ES)

| Specimen number | Load (N) | Flexural Strength (MPa) |
|-----------------|----------|-------------------------|
| 1 | 85.3 | 296.0 |
| 2 | 70.6 | 245.0 |
| 3 | 70.6 | 245.0 |
| 4 | 51.0 | 176.9 |
| 5 | 74.5 | 258.6 |
| 6 | 62.7 | 217.8 |
| 7 | 85.3 | 296.0 |
| 8 | 59.8 | 207.6 |
| 9 | 68.6 | 238.2 |
| 10 | 89.2 | 309.6 |
| 11 | 60.8 | 211.0 |
| 12 | 68.6 | 238.2 |
| 13 | 56.8 | 197.4 |
| 14 | 71.5 | 248.4 |
| 15 | 73.5 | 255.2 |
| 16 | 58.8 | 204.2 |
| 17 | 52.9 | 183.7 |
| 18 | 75.5 | 262.0 |
| 19 | 72.5 | 251.8 |
| 20 | 70.6 | 245.0 |

Group 4 (GV)

| Specimen number | Load (N) | Flexural Strength (MPa) |
|-----------------|----------|-------------------------|
| 1 | 21.6 | 74.9 |
| 2 | 21.6 | 74.9 |
| 3 | 19.6 | 68.1 |
| 4 | 18.6 | 64.6 |
| 5 | 18.6 | 64.6 |
| 6 | 17.6 | 61.2 |
| 7 | 19.6 | 68.1 |
| 8 | 17.6 | 61.2 |
| 9 | 19.6 | 68.1 |
| 10 | 16.7 | 57.8 |
| 11 | 18.6 | 64.6 |
| 12 | 16.7 | 57.8 |
| 13 | 14.7 | 51.0 |
| 14 | 18.6 | 64.6 |
| 15 | 18.6 | 64.6 |
| 16 | 18.6 | 64.6 |
| 17 | 18.6 | 64.6 |
| 18 | 15.7 | 54.4 |
| 19 | 18.6 | 64.6 |
| 20 | 17.6 | 61.2 |

Group 5 (ES - G)

| Specimen number | Load (N) | Flexural Strength (MPa) |
|-----------------|----------|-------------------------|
| 1 | 53.9 | 199.2 |
| 2 | 42.1 | 155.7 |
| 3 | 51.0 | 188.3 |
| 4 | 78.4 | 289.7 |
| 5 | 74.5 | 275.2 |
| 6 | 68.6 | 253.5 |
| 7 | 46.1 | 170.2 |
| 8 | 60.8 | 224.5 |
| 9 | 52.9 | 195.6 |
| 10 | 80.4 | 297.0 |
| 11 | 60.8 | 224.5 |
| 12 | 78.4 | 289.7 |
| 13 | 63.7 | 235.4 |
| 14 | 47.0 | 173.8 |
| 15 | 84.3 | 311.5 |
| 16 | 59.8 | 220.9 |
| 17 | 60.8 | 224.5 |
| 18 | 63.7 | 235.4 |
| 19 | 68.6 | 253.5 |
| 20 | 54.9 | 202.8 |

Group 6 (ES - GV - G)

| Specimen number | Load (N) | Flexural Strength (MPa) |
|-----------------|----------|-------------------------|
| 1 | 65.7 | 268.5 |
| 2 | 73.5 | 300.5 |
| 3 | 40.2 | 164.3 |
| 4 | 46.1 | 188.3 |
| 5 | 60.8 | 248.4 |
| 6 | 59.8 | 244.4 |
| 7 | 52.9 | 216.4 |
| 8 | 58.8 | 240.4 |
| 9 | 57.8 | 236.4 |
| 10 | 61.7 | 252.4 |
| 11 | 66.6 | 272.5 |
| 12 | 65.7 | 268.5 |
| 13 | 50.0 | 204.3 |
| 14 | 50.0 | 204.3 |
| 15 | 67.6 | 276.5 |
| 16 | 72.5 | 296.5 |
| 17 | 66.6 | 272.5 |
| 18 | 57.8 | 236.4 |
| 19 | 50.0 | 204.3 |
| 20 | 39.2 | 160.3 |

Group 7 (ES - dry)

| Specimen number | Load (N) | Flexural Strength (MPa) |
|-----------------|----------|-------------------------|
| 1 | 79.4 | 275.6 |
| 2 | 85.3 | 296.0 |
| 3 | 66.6 | 231.4 |
| 4 | 76.4 | 265.4 |
| 5 | 113.7 | 394.7 |
| 6 | 77.4 | 268.8 |
| 7 | 67.6 | 234.8 |
| 8 | 68.6 | 238.2 |
| 9 | 75.5 | 262.0 |
| 10 | 90.2 | 313.0 |
| 11 | 95.1 | 330.1 |
| 12 | 80.4 | 279.0 |
| 13 | 60.8 | 210.9 |
| 14 | 81.3 | 282.4 |
| 15 | 76.4 | 265.4 |
| 16 | 92.1 | 319.9 |
| 17 | 107.8 | 374.3 |
| 18 | 93.1 | 323.3 |
| 19 | 63.7 | 221.2 |
| 20 | 91.1 | 316.4 |

APPENDIX B
FRACTURE TOUGHNESS DATA (CHAPTER 4)

Group 1 (E1)

| Specimen number | c (μm) | c origin | KIC (MPa·m ^{1/2}) |
|-----------------|--------|----------|-----------------------------|
| 1 | 20 | CF | 1.5 |
| 2 | 95 | SF | 0.8 |
| 3 | 25 | SF | 1.3 |
| 4 | 50 | SF | 1.5 |
| 5 | 25 | SF | 1.5 |
| 6 | 50 | SF | 0.9 |
| 7 | 78 | CF | 0.9 |
| 8 | 90 | SF | 0.9 |
| 9 | 90 | SF | 0.8 |
| 10 | 500 | CF | 2.0 |
| 11 | 25 | SF | 1.5 |
| 12 | 50 | SF | 1.9 |
| 13 | 200 | CF | 1.4 |
| 14 | 220 | CF | 1.3 |
| 15 | 75 | SF | 0.9 |
| 16 | 200 | CF | 1.7 |
| 17 | 50 | SF | 1.1 |
| 18 | 25 | SF | 1.5 |
| 19 | 140 | SF | 1.5 |
| 20 | 185 | SF | 1.1 |

Type of fracture origins:

SF = surface flaw (void or crack);
 CF = corner flaw (void or crack).

Group 2 (E2)

| Specimen number | c (μm) | c origin | KIC (MPa·m ^{1/2}) |
|-----------------|--------|----------|-----------------------------|
| 1 | 150 | CF | 3.4 |
| 2 | 75 | CF | 3.0 |
| 3 | 170 | CF | 4.0 |
| 4 | 200 | CF | 3.9 |
| 5 | 85 | SF | 2.6 |
| 6 | 140 | SF | 3.5 |
| 7 | 170 | SF | 4.5 |
| 8 | 110 | CF | 2.5 |
| 9 | 150 | SF | 2.9 |
| 10 | 200 | SF | 4.7 |
| 11 | 230 | SF | 2.9 |
| 12 | 210 | SF | 4.7 |
| 13 | 220 | SF | 4.7 |
| 14 | 150 | CF | 2.7 |
| 15 | 15 | SF | 2.7 |
| 16 | 180 | SF | 3.5 |
| 17 | 220 | SF | 3.2 |
| 18 | 130 | SF | 3.2 |
| 19 | 130 | SF | 3.2 |
| 20 | 90 | SF | 2.9 |

Type of fracture origins:

SF = surface flaw (void or crack);
 CF = corner flaw (void or crack).

| Group 3 (ES) | | | | Group 4 (GV) | | | |
|-----------------|--------|----------|-----------------------------|-----------------|--------|----------|-----------------------------|
| Specimen number | c (μm) | c origin | KIC (MPa·m ^{1/2}) | Specimen number | c (μm) | c origin | KIC (MPa·m ^{1/2}) |
| 1 | 60 | CF | 3.3 | 1 | 60 | SF | 0.7 |
| 2 | 95 | SF | 3.0 | 2 | 60 | SF | 0.7 |
| 3 | 130 | SF | 3.5 | 3 | 30 | SF | 0.6 |
| 4 | 100 | SF | 2.3 | 4 | 100 | SF | 0.8 |
| 5 | 110 | SF | 3.4 | 5 | 90 | SF | 0.7 |
| 6 | 145 | SF | 3.3 | 6 | 100 | SF | 0.7 |
| 7 | 120 | SF | 4.0 | 7 | 90 | SF | 0.8 |
| 8 | 85 | CF | 2.8 | 8 | 110 | CF | 0.9 |
| 9 | 100 | SF | 3.0 | 9 | 70 | SF | 0.7 |
| 10 | 60 | SF | 3.0 | 10 | 70 | SF | 0.6 |
| 11 | 120 | SF | 2.9 | 11 | 80 | SF | 0.7 |
| 12 | 95 | SF | 2.9 | 12 | 100 | SF | 0.8 |
| 13 | 80 | CF | 2.6 | 13 | 155 | CF | 0.9 |
| 14 | 110 | SF | 3.3 | 14 | 80 | SF | 0.7 |
| 15 | 90 | SF | 3.1 | 15 | 120 | SF | 0.9 |
| 16 | 125 | SF | 3.0 | 16 | 90 | SF | 0.7 |
| 17 | 120 | SF | 2.7 | 17 | 80 | SF | 0.7 |
| 18 | 110 | SF | 3.4 | 18 | 180 | SF | 0.9 |
| 19 | 140 | CF | 4.1 | 19 | 140 | CF | 0.9 |
| 20 | 70 | SF | 2.7 | 20 | 70 | SF | 0.6 |

Type of fracture origins:

SF = surface flaw (void or crack);
 CF = corner flaw (void or crack).

Type of fracture origins:

SF = surface flaw (void or crack);
 CF = corner flaw (void or crack).

APPENDIX C
DYNAMIC CONTACT ANGLE (DCA) DATA (CHAPTER 5)

| N | Group 1 $\theta_a - \theta_r$ | Group 2 $\theta_a - \theta_r$ | Group 3 $\theta_a - \theta_r$ | Group 4 $\theta_a - \theta_r$ |
|----|----------------------------------|----------------------------------|----------------------------------|----------------------------------|
| 1 | 29.6 - 20.8 | 23.6 - 21.3 | 29.5 - 0 | 22.6 - 0 |
| 2 | 14.9 - 19.2 | 12.7 - 17.7 | 27.5 - 0 | 16.2 - 0 |
| 3 | 36.8 - 14.9 | 22.7 - 20.3 | 29.1 - 0 | 18.7 - 0 |
| 4 | 25.8 - 18.5 | 3.4 - 15.3 | 32.0 - 0 | 18.0 - 0 |
| 5 | 36.9 - 18.5 | 16.2 - 17.8 | 33.4 - 0 | 19.9 - 0 |
| 6 | 36.0 - 4.8 | 0 - 0 | 34.5 - 0 | 16.2 - 0 |
| 7 | 24.2 - 4.3 | 13.8 - 20.5 | 35.1 - 0 | 17.3 - 0 |
| 8 | 30.0 - 20.9 | 19.5 - 26.3 | 31.8 - 0 | 19.9 - 0 |
| 9 | 30.4 - 19.0 | 20.9 - 20.9 | 31.2 - 0 | 16.6 - 0 |
| 10 | 30.9 - 20.4 | 6.8 - 22.5 | 37.4 - 0 | 19.0 - 0 |

| N | Group 5 $\theta_a - \theta_r$ | Group 6 $\theta_a - \theta_r$ | Group 7 $\theta_a - \theta_r$ | Group 8 $\theta_a - \theta_r$ |
|----|----------------------------------|----------------------------------|----------------------------------|----------------------------------|
| 1 | 17.0 - 0 | 50.9 - 41.9 | 55.5 - 47.1 | 59.3 - 43.9 |
| 2 | 28.0 - 0 | 56.0 - 43.3 | 55.5 - 45.1 | 57.5 - 43.7 |
| 3 | 20.6 - 0 | 56.3 - 43.6 | 50.4 - 42.2 | 52.2 - 37.5 |
| 4 | 22.6 - 0 | 58.3 - 45.5 | 56.3 - 45.6 | 53.7 - 43.0 |
| 5 | 21.7 - 0 | 55.8 - 44.6 | 58.7 - 48.4 | 58.8 - 44.8 |
| 6 | 18.7 - 0 | 56.2 - 45.1 | 60.6 - 48.1 | 58.2 - 44.6 |
| 7 | 24.1 - 0 | 56.8 - 45.1 | 50.6 - 43.5 | 57.3 - 45.2 |
| 8 | 24.6 - 0 | 57.0 - 45.1 | 56.6 - 42.8 | 54.8 - 44.5 |
| 9 | 20.3 - 0 | 56.6 - 44.2 | 51.9 - 38.7 | 56.3 - 45.7 |
| 10 | 17.3 - 0 | 55.3 - 45.4 | 37.1 - 19.2 | 53.5 - 43.9 |

APPENDIX D
MICROTENSILE BOND STRENGTH AND APPARENT INTERFACIAL
FRACTURE TOUGHNESS (CHAPTER 6)

Group 1: E1:HF

| n | Bond Area (mm ²) | σ (MPa) | c (μm) | K _A (MPa·m ^{1/2}) | Failure mode | c origin |
|----|---------------------------------|------------|-----------|---|-----------------|----------|
| 1 | 1.03 | 30.4 | 79 | 0.38 | 2 | CF |
| 2 | 1.03 | 27.0 | 55 | 0.25 | 2 | SC |
| 3 | 1.03 | 26.3 | 107 | 0.33 | 2 | SC |
| 4 | 1.04 | 25.5 | 98 | 0.31 | 4 | SC |
| 5 | 1.04 | 37.6 | 77 | 0.41 | 4 | SCI |
| 6 | 1.01 | 25.4 | 49 | 0.22 | 5 | SC |
| 7 | 1.00 | 19.5 | 140 | 0.29 | 4 | SCI |
| 8 | 1.00 | 20.9 | 61 | 0.20 | 4 | SC |
| 9 | 1.00 | 27.7 | 74 | 0.29 | 4 | SCI |
| 10 | 1.04 | 37.0 | 77 | 0.41 | 4 | SCI |
| 11 | 1.03 | 30.4 | 79 | 0.38 | 2 | CF |
| 12 | 1.03 | 26.9 | 55 | 0.25 | 2 | SC |
| 13 | 1.04 | 23.8 | 91 | 0.28 | 4 | SCI |
| 14 | 1.03 | 26.0 | 105 | 0.33 | 2 | SC |
| 15 | 1.04 | 25.4 | 98 | 0.31 | 4 | SC |
| 16 | 1.02 | 23.9 | 91 | 0.28 | 4 | SCI |
| 17 | 1.01 | 26.0 | 49 | 0.22 | 5 | SC |
| 18 | 1.00 | 19.5 | 139 | 0.29 | 4 | SCI |
| 19 | 1.01 | 20.9 | 60 | 0.20 | 4 | SC |
| 20 | 1.00 | 27.7 | 71 | 0.29 | 4 | SCI |

Crack origin: SC: semicircular crack; SCI: indentation semicircular crack;
IF: internal flaw; CF: corner flaw

Group 2: E1:S

| n | Bond Area (mm ²) | σ (MPa) | c (μ m) | K_A (MPa \cdot m $^{1/2}$) | Failure mode | c origin |
|----|---------------------------------|-------------------|-----------------|------------------------------------|-----------------|----------|
| 1 | 1.00 | 28.4 | 77 | 0.31 | 5 | SC |
| 2 | 1.00 | 29.0 | 57 | 0.27 | 5 | SC |
| 3 | 1.00 | 14.1 | 103 | 0.17 | 3 | IF |
| 4 | 0.98 | 11.3 | 82 | 0.24 | 4 | SC |
| 5 | 1.00 | 17.3 | 62 | 0.17 | 4 | SC |
| 6 | 1.01 | 15.1 | 64 | 0.15 | 5 | SCI |
| 7 | 1.00 | 17.0 | 95 | 0.23 | 5 | CF |
| 8 | 1.03 | 24.3 | 85 | 0.28 | 4 | SC |
| 9 | 1.00 | 23.2 | 114 | 0.31 | 5 | SC |
| 10 | 1.00 | 28.4 | 77 | 0.31 | 5 | SC |
| 11 | 1.03 | 24.2 | 85 | 0.28 | 4 | SC |
| 12 | 1.00 | 29.1 | 57 | 0.27 | 5 | SC |
| 13 | 1.00 | 15.0 | 106 | 0.17 | 3 | IF |
| 14 | 0.99 | 10.4 | 79 | 0.24 | 4 | SC |
| 15 | 1.00 | 17.3 | 62 | 0.17 | 4 | SC |
| 16 | 1.02 | 15.0 | 65 | 0.15 | 5 | SCI |
| 17 | 1.00 | 17.1 | 95 | 0.23 | 5 | CF |
| 18 | 1.00 | 23.3 | 114 | 0.31 | 5 | SC |
| 19 | 1.03 | 34.4 | 50 | 0.30 | 5 | SC |
| 20 | 1.03 | 35.0 | 48 | 0.30 | 5 | SC |

Crack origin: SC: semicircular crack;
IF: internal flaw;

SCI: indentation semicircular crack;
CF: corner flaw

Group 3: E1:HF + S

| n | Bond Area (mm ²) | σ (MPa) | c (μm) | K _A (MPa·m ^½) | Failure mode | c origin |
|----|---------------------------------|------------|-----------|---|-----------------|----------|
| 1 | 1.02 | 20.7 | 77 | 0.23 | 2 | SC |
| 2 | 1.00 | 27.5 | 61 | 0.27 | 4 | SC |
| 3 | 0.99 | 31.1 | 95 | 0.38 | 2 | SC |
| 4 | 1.00 | 17.0 | 81 | 0.19 | 2 | SC |
| 5 | 1.00 | 24.2 | 92 | 0.29 | 4 | SC |
| 6 | 1.00 | 23.8 | 57 | 0.22 | 4 | SC |
| 7 | 1.01 | 32.0 | 100 | 0.40 | 2 | SC |
| 8 | 0.99 | 17.6 | 106 | 0.22 | 4 | SCI |
| 9 | 0.99 | 25.4 | 49 | 0.20 | 4 | SCI |
| 10 | 0.99 | 23.1 | 55 | 0.21 | 4 | SCI |
| 11 | 1.01 | 20.6 | 78 | 0.23 | 2 | SC |
| 12 | 1.00 | 27.5 | 60 | 0.27 | 4 | SC |
| 13 | 1.00 | 17.1 | 82 | 0.19 | 2 | SC |
| 14 | 0.99 | 17.5 | 105 | 0.22 | 4 | SCI |
| 15 | 1.00 | 24.2 | 91 | 0.29 | 4 | SC |
| 16 | 1.00 | 23.8 | 57 | 0.22 | 4 | SC |
| 17 | 0.99 | 30.0 | 97 | 0.40 | 2 | SC |
| 18 | 1.01 | 31.2 | 95 | 0.38 | 2 | SC |
| 19 | 1.00 | 23.4 | 50 | 0.20 | 4 | SCI |
| 20 | 0.99 | 23.1 | 52 | 0.21 | 4 | SCI |

Crack origin: SC: semicircular crack;
IF: internal flaw;

SCI: indentation semicircular crack;
CF: corner flaw

Group 4: E2:HF

| n | Bond Area (mm ²) | σ (MPa) | c (μ m) | K_A (MPa \cdot m $^{1/2}$) | Failure mode | c origin |
|----|---------------------------------|-------------------|-----------------|------------------------------------|-----------------|----------|
| 1 | 1.00 | 28.6 | 150 | 0.43 | 5 | SC |
| 2 | 1.00 | 38.1 | 92 | 0.45 | 5 | SCI |
| 3 | 1.02 | 18.5 | 131 | 0.26 | 2 | SC |
| 4 | 1.00 | 19.0 | 335 | 0.43 | 5 | SC |
| 5 | 1.00 | 39.3 | 120 | 0.53 | 4 | SC |
| 6 | 0.99 | 27.5 | 69 | 0.32 | 4 | CF |
| 7 | 1.03 | 34.1 | 60 | 0.33 | 5 | SCI |
| 8 | 1.03 | 30.4 | 122 | 0.42 | 4 | SCI |
| 9 | 1.02 | 41.8 | 72 | 0.44 | 5 | SC |
| 10 | 1.03 | 41.5 | 60 | 0.40 | 5 | SCI |
| 11 | 1.00 | 30.1 | 155 | 0.43 | 5 | SC |
| 12 | 1.00 | 38.1 | 92 | 0.45 | 5 | SCI |
| 13 | 1.00 | 20.5 | 330 | 0.43 | 5 | SC |
| 14 | 0.99 | 27.4 | 70 | 0.32 | 4 | CF |
| 15 | 1.03 | 34.0 | 60 | 0.33 | 5 | SCI |
| 16 | 1.03 | 18.4 | 130 | 0.26 | 2 | SC |
| 17 | 1.04 | 30.3 | 122 | 0.42 | 4 | SCI |
| 18 | 0.99 | 36.3 | 113 | 0.53 | 4 | SC |
| 19 | 1.03 | 41.9 | 72 | 0.44 | 5 | SC |
| 20 | 1.03 | 41.4 | 60 | 0.40 | 5 | SCI |

Crack origin: SC: semicircular crack; SCI: indentation semicircular crack;
IF: internal flaw; CF: corner flaw

Group 5: E2:S

| n | Bond Area (mm ²) | σ (MPa) | c (μm) | K_A (MPa \cdot m $^{1/2}$) | Failure mode | c origin |
|----|---------------------------------|-------------------|------------------------|------------------------------------|-----------------|----------|
| 1 | 0.98 | 5.1 | 415 | 0.15 | 2 | CF |
| 2 | 1.00 | 5.1 | 56 | 0.05 | 4 | SC |
| 3 | 1.01 | 5.9 | 112 | 0.08 | 2 | SC |
| 4 | 1.00 | 19.2 | 40 | 0.15 | 4 | SC |
| 5 | 0.99 | 4.2 | 79 | 0.05 | 2 | SC |
| 6 | 1.00 | 5.2 | 58 | 0.05 | 4 | SC |
| 7 | 1.00 | 16.3 | 55 | 0.15 | 4 | SC |
| 8 | 1.00 | 13.1 | 52 | 0.12 | 4 | SC |
| 9 | 1.02 | 19.1 | 122 | 0.26 | 4 | SC |
| 10 | 0.98 | 8.2 | 114 | 0.11 | 2 | SC |
| 11 | 1.02 | 18.0 | 81 | 0.20 | 4 | SC |
| 12 | 0.98 | 5.0 | 411 | 0.15 | 2 | CF |
| 13 | 1.00 | 5.9 | 111 | 0.08 | 2 | SC |
| 14 | 1.00 | 19.4 | 40 | 0.15 | 4 | SC |
| 15 | 1.00 | 4.2 | 79 | 0.05 | 2 | SC |
| 16 | 1.00 | 16.0 | 55 | 0.15 | 4 | SC |
| 17 | 1.00 | 13.0 | 52 | 0.12 | 4 | SC |
| 18 | 1.02 | 19.0 | 123 | 0.26 | 4 | SC |
| 19 | 0.98 | 8.3 | 115 | 0.11 | 2 | SC |
| 20 | 1.02 | 18.0 | 82 | 0.20 | 4 | SC |

Crack origin: SC: semicircular crack;
 IF: internal flaw; SCI: indentation semicircular crack;
 CF: corner flaw

Group 6: E2:HF + S

| n | Bond Area (mm ²) | σ (MPa) | c (μm) | K_A (MPa \cdot m $^{1/2}$) | Failure mode | c origin |
|----|---------------------------------|-------------------|------------------------|------------------------------------|-----------------|----------|
| 1 | 0.98 | 26.0 | 58 | 0.25 | 4 | SC |
| 2 | 1.01 | 29.8 | 67 | 0.30 | 4 | SC |
| 3 | 0.99 | 21.7 | 68 | 0.22 | 5 | SC |
| 4 | 0.98 | 22.9 | 57 | 0.22 | 4 | SC |
| 5 | 0.98 | 21.8 | 68 | 0.22 | 5 | SC |
| 6 | 0.99 | 37.4 | 71 | 0.39 | 5 | SC |
| 7 | 0.98 | 35.3 | 51 | 0.31 | 4 | SC |
| 8 | 1.01 | 30.2 | 79 | 0.33 | 5 | SC |
| 9 | 1.01 | 26.3 | 61 | 0.25 | 4 | SC |
| 10 | 1.01 | 30.0 | 67 | 0.30 | 4 | SC |
| 11 | 1.00 | 29.0 | 44 | 0.24 | 4 | SC |
| 12 | 0.98 | 26.0 | 57 | 0.25 | 4 | SC |
| 13 | 0.98 | 22.0 | 68 | 0.22 | 5 | SC |
| 14 | 1.00 | 23.0 | 58 | 0.22 | 4 | SC |
| 15 | 0.99 | 21.8 | 70 | 0.22 | 5 | SC |
| 16 | 0.98 | 37.4 | 71 | 0.39 | 5 | SC |
| 17 | 0.98 | 35.0 | 50 | 0.31 | 4 | SC |
| 18 | 1.01 | 30.0 | 80 | 0.33 | 5 | SC |
| 19 | 1.02 | 26.2 | 60 | 0.25 | 4 | SC |
| 20 | 1.01 | 29.0 | 45 | 0.24 | 4 | SC |

Crack origin: SC: semicircular crack;
 IF: internal flaw; SCI: indentation semicircular crack;
 CF: corner flaw

LIST OF REFERENCES

al Edris A, al Jabr A, Cooley RL, Barghi N (1990). SEM evaluation of etch patterns by three etchants on three porcelains. *J Prosthet Dent*, 64:734-739.

Alexander DJ (1990). Quantitative analysis of fracture surfaces using fractals. In: Quantitative Methods in Fractography. ASTM STP 1085, Philadelphia. pp. 39-51.

Anokye WK (1989). The effect of residual stress, processing and thermodynamic parameters on toughness of glass-metal seals. Ph.D. Dissertation, University of Florida.

Anstis GR, Chantikul P, Lawn BR, Marshall DB (1981). A critical evaluation of indentation techniques for measuring fracture toughness: I, direct crack measurements. *J Am Cer Soc*, 64:533-538.

Anusavice KJ (1983). Screening tests for metal-ceramic systems. In: McLean JW, ed. Dental Ceramics: Proceedings of the First International Symposium on Ceramics. Chicago, IL: Quintessence Publishing Co., pp. 371-414.

Anusavice KJ (1992). Degradability of dental ceramics. *Adv Dent Res*, 6:82-89.

Anusavice KJ (1996). Phillips' Science of Dental Materials. 10th ed. Philadelphia: W.B. Saunders.

Anusavice KJ, Dehoff PH, Fairhurst CW (1980). Comparative evaluation of ceramic-metal bond tests using finite element stress analysis. *J Dent Res*, 59:608-613.

Anusavice KJ, Gray A, Shen C (1991). Influence of initial flaw size on crack growth in air-tempered porcelain. *J Dent Res*, 70:131-136.

Anusavice KJ, Lee RB (1989). Effect of firing temperature and water exposure on crack propagation in unglazed porcelain. *J Dent Res*, 68:1075-1081.

Armstrong SR, Boyer DB, Keller JC (1998). Microtensile bond strength testing and failure analysis of two dentin adhesives. *Dent Mater*, 14:44-50.

Attal JP, Edard V, Degrange M (1990). Factors modifying the accuracy of free energy surface measured by contact angle method. *J Biomater Dent*, 5:143-155.

Bailey JH (1989). Porcelain-to-composite bond strengths using four organosilane materials. *J Prosthet Dent*, 61:174-177.

Ban S, Anusavice KJ (1990). Influence of test method on failure stress of brittle dental materials. *J Dent Res*, 69:1791-1799.

Berry T, Barghi N, Chung K (1999). Effect of water storage on the silanization in porcelain repair strength. *J Oral Rehabil*, 26:459-463.

Bouchaud JP, Bouchaud E, Lapasset G, Planes J (1993). *Phys Rev Ltrs*, 71:2240.

Bouschlicher MR, Reinhardt JW, Vargas MA (1997). Surface treatment techniques for resin composite repair. *Am J Dent*, 10:279-283.

Bowen RL (1963). Properties of silica-reinforced polymer for dental restorations. *J Am Dent Assoc*, 66:57-64.

Boyer HE, Gall TL, eds (1992). Metals Handbook Desk Edition. Metals Park, OH: American Society for Metals, pp. 35.16 - 35.20.

Callister WD (2000). Materials Science and Engineering: An Introduction. 5th ed. New York: John Wiley & Sons, Inc.

Cardoso PEC, Braga RR, Carrilho MRO (1998). Evaluation of micro-tensile, shear and tensile tests determining the bond strength of three adhesive systems. *Dent Mater*, 14:394-398.

Cattell MJ, Clarke RL, Lynch EJ (1997). The transverse strength, reliability and microstructural features of four dental ceramics – part 1. *J Dent*, 25:399-407.

Chadwick RG, Mason AG, Sharp W (1998). Attempted evaluation of three porcelain repair systems – what are we really testing? *J Oral Rehabil*, 25:610-615.

Chantikul P, Anstis GR, Lawn BR, Marshall DB (1981). A critical evaluation of indentation techniques for measuring fracture toughness: II, strength method. *J Am Cer Soc*, 64:539-543.

Chen JH, Matsumura H, Atsuta M (1998a). Effect of different etching periods on the bond strength of a composite resin to a machinable porcelain. *J Dent*, 26:53-58.

Chen JH, Matsumura H, Atsuta M (1998b). Effect of etchant, etching period, and silane priming on bond strength to porcelain of composite resin. *Oper Dent*, 23:250-257.

Chen Z, Mecholsky JJ Jr. (1993). Control of strength and toughness of ceramic/metal laminates using interface design. *J Mater Res*, 8:2362-2369.

Chen Z, Mecholsky JJ Jr., Joseph T, Beatty CL (1997). The fractal geometry of Si_3N_4 wear and fracture surfaces. *J Mater Sci*, 32: 6317-6323.

Claus H (1989). The structure and microstructure of dental porcelain in relationship to the firing conditions. *Int J Prosthodont*, 2: 376-384.

Coffey JP, Anusavice KJ, DeHoff PH, Lee RB, Hojjati B (1988). Influence of contraction mismatch and cooling rate on flexural failure of PFM systems. *J Dent Res*, 67:61-65.

DeHoff PH, Anusavice KJ, Hathcock PW (1982). An evaluation of the four-point flexural test for metal-ceramic bond strength. *J Dent Res*, 61:1066-1069.

DeHoff PH, Anusavice KJ, Wang Z (1995). Three-dimensional finite element analysis of the shear bond test. *Dent Mater*, 11:126-131.

DeHoff RT, Rhines FN (1968). Quantitative Microscopy. New York: McGraw-Hill.

Della Bona A, Anusavice KJ, Shen C (2000). Microtensile strength of composite bonded to hot-pressed ceramics. *J Adhesive Dent*, 2:305-313.

Della Bona A, Hill TJ, Mecholsky JJ Jr. (2001). The effect of contour angle on fractal dimension measurements for brittle materials. *J Mater Sci*, 36:2645-2650.

Della Bona A, Northeast SE (1994). Shear bond strength of resin bonded ceramic after different try-in procedures. *J Dent*, 22:103-107.

Della Bona A, van Noort R (1995). Shear versus tensile bond strength of resin composite bonded to ceramic. *J Dent Res*, 74:1591-1596.

Della Bona A, van Noort R (1998). Ceramic surface preparations for resin bonding: a SEM study. *Am J Dent*, 11:276-280.

Denry IL, Holloway JA, Rosenstiel SF (1998). Effect of ion exchange on the microstructure, strength, and thermal expansion behavior of leucite-reinforced porcelain. *J Dent Res*, 77:583-588.

Denry IL, Mackert JR Jr., Holloway JA, Rosenstiel SF (1996). Effect of cubic leucite stabilization on the flexural strength of feldspathic dental porcelain. *J Dent Res*, 75:1928-1935.

Diaz-Arnold AM, Aquilino SA (1989). An evaluation of the bond strengths of four organosilane materials in response to thermal stress. *J Prosthet Dent*, 62:257-260.

Drummond JL, King TJ, Bapna MS, Koperski RD (2000). Mechanical property evaluation of pressable restorative ceramics. *Dent Mater*, 16:226-233.

Eikenberg S, Shurtleff J (1996). Effect of hydration on bond strength of a silane-bonded composite to porcelain after seven months. *Gen Dent*, 44:58-61.

Faber KT, Evans AG (1983). Crack deflection processes - 1. Theory. *Acta Metall*, 31:565-576.

Fairhurst CW, Lockwood PE, Ringle RD, Thompson WO (1992). The effect of glaze on porcelain strength. *Dent Mater*, 8:203-207.

Fréchette VD (1990). Failure Analysis of Brittle Materials. Westerville, OH: American Ceramic Society.

Freiman SW, Hench LL (1972). Effect of crystallization on the mechanical properties of $\text{Li}_2\text{O}\text{-SiO}_2$ glass-ceramics. *J Am Cer Soc*, 55:86-90.

Giordano RA, Pelleiter L, Campbell S, Pober R (1995). Flexural strength of an infused ceramic, glass ceramic, and feldspathic porcelain. *J Prosthet Dent*, 73:411-418.

Griffith AA (1920). The phenomena of rupture and flow in solids. *Philos Trans R Soc (London)*, 221:163-198.

Healey JT, Mecholsky JJ Jr. (1984). Scanning electron microscopy techniques and their application to failure analysis of brittle materials. In: Mecholsky JJ Jr., Powell SR Jr., eds. *Fractography of Ceramic and Metal Failures*, ASTM STP 827. Philadelphia, PA: American Society for Testing and Materials, pp.157-181.

Hertzberg RW (1996). Deformation and Fracture Mechanics of Engineering Materials. 4th ed. New York: J. Wiley & Sons.

Hill TJ, Della Bona A, Mecholsky JJ Jr. (2001). Establishing a protocol for measurements of fractal dimension in brittle materials. *J Mater Sci*, 36:2651-2657.

Hill TJ, Mecholsky JJ Jr., Anusavice KJ (2000). Fractal analysis of toughening behavior in $3\text{BaO}\text{-}5\text{SiO}_2$ glass-ceramics. *J Am Cer Soc*, 83:545-552.

Höland W, Schweiger M, Frank M, Rheinberger V (2000). A comparison of the microstructure and properties of the IPS Empress 2 and the IPS Empress glass-ceramics. *J Biomed Mater Res*, 53:297-303.

Hooshmand T, Daw R, van Noort R, Short RD (2001). XPS analysis of the surface of leucite-reinforced feldspathic ceramics. *Dent Mater*, 17:1-6.

Horn HR (1983). Porcelain laminate veneers bonded to etched enamel. *Dent Clin North Am*, 27:671-684.

Howard CV, Reed MG (1998). Unbiased Stereology: Three-Dimensional Measurement in Microscopy. Oxford, UK: BIOS Scientific Publishers.

Hussain MA, Bradford EW, Charlton G (1979). Effect of etching on the strength of a luminous porcelain jacket crown. *Br Dent J*, 147:89-90.

International Organization for Standardization (1995). ISO 6872: Dental Ceramics, 2nd ed. Geneva: The Organization.

Irwin GR (1957). Analysis of stresses and strains near the end of crack transversing a plate. *J Appl Mech*, 24:361-364.

Jardel V, Degrange M, Picard B, Derrien G (1999a). Correlation of topography to bond strength of etched ceramic. *Int J Prosthodont*, 12:59-64.

Jardel V, Degrange M, Picard B, Derrien G (1999b). Surface energy of etched ceramic. *Int J Prosthodont*, 12:415-418.

Johnson CA (1983). Fracture statics of multiple flaw distribution. In: Bradt RC, Evans AG, Hasselman DPH, Lange FF, eds. Fracture Mechanics of Ceramics, Vol. 5, Surface Flaws, Statics, and Microcracking. New York, NY: Plenum Press, pp. 365-386.

Jones DW (1985). Development of dental ceramics: an historical perspective. *Dent Clin North Am*, 29:621-644.

Jung Y-G, Wuttiphhan S, Peterson IM, Lawn BR (1999). Damage modes in dental layer structures. *J Dent Res*, 78:887-897.

Kamada K, Yoshida K, Atsuta M (1998). Effect of ceramic surface treatments on the bond of four resin luting agents to a ceramic material. *J Prosthet Dent*, 79:508-513.

Kato H, Matsumura H, Tanaka T, Atsuta M (1996). Bond strength and durability of porcelain bonding systems. *J Prosthet Dent*, 75:163-168.

Kelly JR (1995). Perspectives on strength. *Dent Mater*, 11:103-110.

Kelly JR, Campbell SD, Bowen HK (1989). Fracture-surface analysis of dental ceramics. *J Prosthet Dent*, 62:536-541.

Kelly JR, Giordano R, Pober R, Cima MJ (1990). Fracture surface analysis of dental ceramics: clinically failed restorations. *Int J Prosthodont*, 3:430-440.

Kingery WD, Bowen HK, Uhlmann DR (1976). Introduction to Ceramics. 2nd ed. New York: Wiley.

Kitasako Y, Burrow MF, Nikaido T, Harada N, Inokoshi S, Yamada T, *et al.* (1995). Shear and tensile bond testing for resin cement evaluation. *Dent Mater*, 11:298-304.

Kulawansa DM, Jensen LC, Langford SC, Dickinson JT, Watanabe Y (1994). Scanning tunneling microscope observations in the mirror region of silicate glass fracture surfaces. *J Mat Res*, 9:476-485.

Kupiec KA, Wuertz KM, Barkmeier WW, Wilwerding TM (1996). Evaluation of porcelain surface treatments and agents for composite-to-porcelain repair. *J Prosthet Dent*, 76:119-124.

Lawn BR, Lee SK, Peterson IM, Wuttiphant S (1998). Model of strength degradation from Hertzian contact damage in tough ceramics. *J Am Ceram Soc*, 81:1509-1520.

Lawn BR, Padture NP, Cai H, Guiberteau F (1994). Making ceramics "ductile". *Science*, 263(5150):1114-1116.

Lee LH (1975). Adhesion Science and Technology. American Chemical Society. New York: Plenum Press.

Leibrock A, Degenhart M, Behr M, Rosentritt M, Handel G (1999). In vitro study of the effect of thermo- and load-cycling on the bond strength of porcelain repair systems. *J Oral Rehabil*, 26:130-137.

Lu, R, Harcourt JK, Tyas MJ, Alexander B (1992). An investigation of the composite resin/porcelain interface. *Aust Dent J*, 37:12-19.

Luthy H, Dong JK, Wohlwend A, Scharer P (1993). Effects of veneering and glazing on the strength of heat-pressed ceramics. *Schweizer Monatsschrift für Zahnmedizin*, 103:1257-1260.

Mackert JR Jr., Butts MB, Fairhurst CW (1986). The effect of the leucite transformation on dental porcelain expansion. *Dent Mater*, 2:32-36.

Mackert JR Jr., Evans AL (1991). Effect of cooling rate on leucite volume fraction in dental porcelains. *J Dent Res*, 70:137-139.

Mandelbrot BB (1982). The Fractal Geometry of Nature. San Francisco: W. H. Freeman & Co.

Mandelbrot BB, Passoja DE, Pauley AJ (1984). Fractal character of metals. *Nature*, 308:721-722.

Marshall DB, Lawn BR (1985). Indentation of Brittle Materials (ASTM Committee E-4 on Metallography. Int Metallographic Soc: Microindentation Techniques in

Materials Science and Engineering). Philadelphia: ASTM Special Technical Publication, pp. 26-46.

McCabe JF, Carrick TE (1986). A statistical approach to the mechanical testing of dental materials. *Dent Mater* 2:139-142.

Mecholsky JJ Jr. (1981). Toughening in glass ceramics through microstructural design. In: Bradt RC, Hasselman DPH, Lange FF, eds. Fracture Mechanics of Ceramics. New York: Plenum Press, Vol. 8, pp. 165-180.

Mecholsky JJ Jr. (1993). Quantitative fracture surface analysis of glass materials. In: Simmons CJ, El-Bayoumi O, eds. Experimental Techniques of Glass Science. Westerville, OH: American Ceramic Society, pp. 483-520.

Mecholsky JJ Jr. (1995a). Fractography: determining the sites of fracture initiation. *Dent Mater* 11:113-116.

Mecholsky JJ Jr. (1995b). Fracture mechanics principles. *Dent Mater*, 11:111-112.

Mecholsky JJ Jr. (1996). Fractography, fracture mechanics, and fractal geometry: An integration. In: Varner JR, Frechette VD, Quinn GD, eds. Fractography of Glasses and Ceramics III. Westerville, OH: American Ceramic Society, pp. 385-393.

Mecholsky JJ Jr., Barker LM (1984). A chevron-notched specimen for fracture toughness measurements of ceramic-metal interfaces. ASTM STP 855: 324-336.

Mecholsky JJ Jr., Freiman SW (1991). Relationship between fractal geometry and fractography. *J Am Ceram Soc*, 74:3136-3138.

Mecholsky JJ Jr., Freiman SW, Rice RW (1978). Fractographic analysis of ceramics. In: Strauss BM, Cullen WH, eds. Fractography in Failure Analysis (ASTM STP 645). Philadelphia: American Society for Testing and Materials, pp. 363-379.

Mecholsky JJ Jr., Mackin TJ, Passoja DE (1988). Self-similar crack propagation in brittle materials. In: Frechette VC, Varner J, eds. Advances in Ceramics, Vol 22: Fractography of Glasses and Ceramics. Westerville: Am Cer Soc, pp. 127-134.

Mecholsky JJ Jr., Passoja DE, Feinberg-Ringel KS (1989). Quantitative analysis of brittle fracture surfaces using fractal geometry. *J Am Ceram Soc*, 72:60-65.

Mecholsky JJ Jr., Plaia JR (1992). Fractal analysis on fracture surfaces of glass using replication techniques. *J Non-Cryst Solids*, 146:249-255.

Nakajima M, Sano H, Urabe I, Tagami J, Pashley DH (2000). Bond strengths of single-bottle dentin adhesives to caries-affected dentin. *Oper Dent*, 25:2-10.

Pameijer CH, Louw NP, Fischer D (1996). Repairing fractured porcelain: how surface preparation affects shear force resistance. *J Am Dent Assoc*, 127:203-209.

Panighi M, G'Sell C (1993). Physico-chemical study of dental surfaces and mechanisms of composite adhesion. *J Biomater Dent*, 8:61-70.

Pashley DH, Carvalho RM, Sano H, Nakajima M, Yoshiyama M, Shono Y, et al. (1999). The microtensile bond test: a review. *J Adhes Dent*, 1:299-309.

Pashley DH, Sano H, Ciucchi B, Yoshiyama M, Carvalho RM (1995). Adhesion testing of dentin bonding agents: a review. *Dent Mater*, 11:117-125.

Peterson IM, Pajares A, Lawn BR, Thompson VP, Rekow ED (1998a). Mechanical characterization of dental ceramics by Hertzian contacts. *J Dent Res*, 77:589-602.

Peterson IM, Wuttiphap S, Lawn BR, Chyung K (1998b). Role of microstructure on contact damage and strength degradation of micaceous glass-ceramics. *Dent Mater*, 14:80-89.

Phoenix RD, Shen C (1995). Characterization of treated porcelain surfaces via dynamic contact angle analysis. *Int J Prosthodont*, 8:187-194.

Phrukkanon S, Burrow MF, Tyas MJ (1998a). Effect of cross-sectional surface area on bond strengths between resin and dentin. *Dent Mater*, 14:120-128.

Phrukkanon S, Burrow MF, Tyas MJ (1998b). The influence of cross-sectional shape and surface area on the microtensile bond test. *Dent Mater*, 14:212-221.

Phrukkanon S, Burrow MF, Tyas MJ (1999). The effect of dentine location and tubule orientation on the bond strengths between resin and dentine. *J Dent*, 27:265-74.

Piche PW, O'Brien WJ, Groh CL, Boenke KM (1994). Leucite content of selected dental porcelains. *J Biomed Mater Res*, 28:603-609.

Plueddemann, EP (1991). *Silane Coupling Agents*. New York: Plenum Press.

Pratt RC, Burgess JO, Schwartz RS, Smith JH (1989). Evaluation of bond strength of six porcelain repair systems. *J Prosthet Dent*, 62:11-13.

Rahaman MN (1995). *Ceramic Processing and Sintering*. New York: Marcel Dekker, Inc.

Randall PN (1966). Plain strain crack toughness testing of high strength metallic materials. In: Brown WF Jr., Strawley JE, eds. *ASTM STP 410*. Philadelphia: Am Soc Test Mater, pp. 88-126.

Rice RW (1984). Ceramic fracture features, observations, mechanisms, and uses. In: Mecholsky JJ Jr., Powell SR Jr., eds. *Fractography of Ceramic and Metal Failures*, ASTM STP 827. Philadelphia, PA: American Society for Testing and Materials, pp. 5-103.

Rice RW (1988). Perspective on fractography. In: Frechette VC, Varner J, eds. *Advances in Ceramics, Vol 22: Fractography of Glasses and Ceramics*. Westerville, OH: American Ceramic Society, pp. 127-134.

Ritter JE (1995a). Critique of test methods for lifetime predictions. *Dent Mater*, 11:147-151.

Ritter JE (1995b). Predicting lifetimes of materials and material structures. *Dent Mater*, 11: 142-146.

Roulet JF, Söderholm KJ, Longmate J (1995). Effects of treatment and storage conditions on ceramic/composite bond strength. *J Dent Res*, 74:381-387.

Russ JC (1994). *Fractal Surfaces*. New York, NY: Plenum Press.

Sano H, Shono T, Sonoda H, Takatsu T, Ciucchi B, Carvalho R, Pashley D (1994). Relationship between surface area for adhesion and tensile bond strength-Evaluation of a micro-tensile bond test. *Dent Mater*, 10: 236-240.

Sano H, Yoshikawa T, Pereira PN, Kanemura N, Morigami M, Tagami J, et al. (1999). Long-term durability of dentin bonds made with a self-etching primer, in vivo. *J Dent Res*, 78:906-911.

Sato K, Matsumura H, Atsuta M (1999). Effect of three-liquid bonding agents on bond strength to a machine-milled ceramic material. *J Oral Rehabil*, 26:570-574.

Scherrer SS, Denry IL, Wiskott HW (1998). Comparison of three fracture toughness testing techniques using a dental glass and a dental ceramic. *Dent Mater*, 14:246-255.

Scherrer SS, Kelly JR, Quinn GD, Xu K (1999). Fracture toughness (K_{IC}) of a dental porcelain determined by fractographic analysis. *Dent Mater*, 15:342-348.

Schroder ME (1999). Work of Adhesion of a Sessile Drop to a Clean Surface. *J Colloid Interface Sci*, 213:602-605.

Schreiner RF, Chappell RP, Glaros AG, Eick JD (1998). Microtensile testing of dentin adhesives. *Dent Mater*, 14:194-201.

Sheth J, Jensen M, Tolliver D (1988). Effect of surface treatment on etched porcelain bond strength to enamel. *Dent Mater*, 4:328-337.

Shono Y, Ogawa T, Terashita M, Carvalho RM, Pashley EL, Pashley DH (1999a). Regional measurement of resin-dentin bonding as an array. *J Dent Res*, 78:699-705.

Shono Y, Terashita M, Shimada J, Kozono Y, Carvalho RM, Russell CM, *et al.* (1999b). Durability of resin-dentin bonds. *J Adhesive Dent*, 1:211-218.

Sudsangiam S, van Noort R (1999). Do dentin bond strength tests serve a useful purpose? *J Adhesive Dent*, 1:57-67.

Tam LE, Pilliar RM (1993). Fracture toughness of dentin/resin-composite adhesive interfaces. *J Dent Res*, 72:953-959.

Tanumihارja M, Burrow MF, Tyas MJ (2000). Microtensile bond strengths of seven dentin adhesive systems. *Dent Mater*, 16:180-187.

Thompson GA (2000). Influence of relative layer height and testing method on the failure mode and origin in a bilayered dental ceramic composite. *Dent Mater*, 16:235-243.

Thompson JY, Anusavice KJ, Naman A, Morris HF (1994). Fracture surface characterization of clinically failed all-ceramics crowns. *J Dent Res*, 73:1824-1832.

Thompson JY (1995). Characterization of mechanical behavior based on microstructural phenomena in $\text{Li}_2\text{O}\bullet 2\text{SiO}_2$ glass ceramics. Ph.D. Dissertation, University of Florida.

Tsai YL, Mecholsky JJ Jr. (1991). Fractal fracture of single crystal silicon. *J Mater Res*, 6:1248-1263.

Tsai YL, Petsche PE, Anusavice KJ, Yang MC (1998). Influence of glass-ceramic thickness on Hertzian and bulk fracture mechanisms. *Int J Prosthodont*, 11:27-32.

Van Noort R, Cardew GE, Howard IC, Noroozi S (1991). The effect of local interfacial geometry on the measurement of the tensile bond strength to dentin. *J Dent Res*, 70:889-893.

Van Noort R, Noroozi S, Howard IC, Cardew G (1989). A critique of bond strength measurements. *J Dent*, 17: 61-67.

Versluis A, Tantbirojn D, Douglas WH (1997). Why do shear bond tests pull out dentin? *J Dent Res*, 76:1298-1307.

Wakabayashi N, Anusavice KJ (2000). Crack initiation modes in bilayered alumina/porcelain disks as a function of core/veneer thickness ratio and supporting substrate stiffness. *J Dent Res*, 79(6):1398-1404.

Weibull W (1939). A statistical theory of the strength of materials. *Ing Vetensk Akad Proc*, 151:1-45.

Wenzel RN (1936). Resistance of solid surfaces to wetting by water. *Ind Eng Chem* 28:988-994.

West JK, Mecholsky JJ Jr., Hench LL (1999). The application of fractal and quantum geometry to brittle fracture. *J Non-Cryst Solids*, 260: 99-108.

White SN, Caputo AA, Li ZC, Zhao XY (1996). Modulus of rupture of the Procera All-Ceramic System. *J Esthet Dent*, 8:120-126.

Wu CC, Freiman SW, Rice RW, Mecholsky JJ Jr. (1978). Microstructural aspects of crack propagation in ceramics. *J Mater Sci*, 13:2659-2670.

Wuttiphant S, Lawn BR, Padture NP (1996). Crack suppression in strongly-bonded homogeneous/heterogeneous laminates: a study on glass/glass ceramic bilayers. *J Am Cer Soc*, 79:634-640.

Yoshikawa T, Sano H, Burrow MF, Tagami J, Pashley DH (1999). Effects of dentin depth and cavity configuration on bond strength. *J Dent Res*, 78:898-905.

Zisman WA (1964). Relation of the equilibrium contact angle to liquid and solid constitution. *Advan Chem Ser*, 43:1-51.

BIOGRAPHICAL SKETCH

Alvaro Della Bona was born in Soledade, Rio Grande do Sul (RS), Brazil, on September 15, 1965. After high school he was admitted to the Dental College, at the University of Passo Fundo (UPF), Passo Fundo, RS, Brazil, in 1983 receiving a Doctor of Dental Surgery (D.D.S.) degree in 1987. While working as a dentist in private practice in Soledade, RS, Brazil, he received a scholarship from the Rotary Foundation to attend the Preceptorship program in Restorative Dentistry: Esthetics and Occlusion, at the University of Texas Health Science Center at San Antonio (UTHSCSA), Texas, U.S.A., in 1990. Dr. Della Bona moved to Sheffield, England, to pursue further studies at the University of Sheffield, School of Clinical Dentistry, where he received the Master of Medical Science (MMedSci) degree in Restorative Dentistry in 1994. He returned to Brazil to work in private practice, as specialist in restorative dentistry, and as Associate Professor and Research Coordinator at three Universities: UPF; Pontifical Catholic University at Porto Alegre, RS, Brazil; and Brazilian Lutheran University at Canoas, RS, Brazil. In 1996, he was honored with a Postgraduate Visiting Fellowship award from the International Association for Dental Research (IADR) and the University of Otago, Department of Restorative Dentistry, Dunedin, New Zealand, to study the composition and microstructure of dental ceramics. He returned to Brazil, in 1997, to continue his work at the dental practice and at the universities until August 1998 when he was admitted to the graduate program at the University of Florida. Dr. Della Bona and his wife Carla B. Scheffer, a practicing attorney, enjoy a beautiful daughter, Izadora. Upon

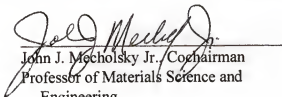
receiving his Doctor of Philosophy degree, Dr. Della Bona will resume working in Brazil as a Professor and Research Coordinator at the Dental College at UPF.

I certify that I have read this study and that in my opinion it conforms to acceptable standards of scholarly presentation and is fully adequate, in scope and quality, as a dissertation for the degree of Doctor of Philosophy.



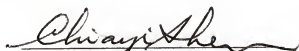
Kenneth J. Anusavice, Chairman
Professor of Materials Science and
Engineering

I certify that I have read this study and that in my opinion it conforms to acceptable standards of scholarly presentation and is fully adequate, in scope and quality, as a dissertation for the degree of Doctor of Philosophy.



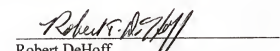
John J. Mecholsky Jr. Cochairman
Professor of Materials Science and
Engineering

I certify that I have read this study and that in my opinion it conforms to acceptable standards of scholarly presentation and is fully adequate, in scope and quality, as a dissertation for the degree of Doctor of Philosophy.



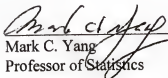
Chiayi Shen
Associate Professor of Materials Science
and Engineering

I certify that I have read this study and that in my opinion it conforms to acceptable standards of scholarly presentation and is fully adequate, in scope and quality, as a dissertation for the degree of Doctor of Philosophy.



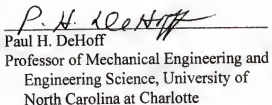
Robert DeHoff
Professor of Materials Science and
Engineering

I certify that I have read this study and that in my opinion it conforms to acceptable standards of scholarly presentation and is fully adequate, in scope and quality, as a dissertation for the degree of Doctor of Philosophy.



Mark C. Yang
Professor of Statistics

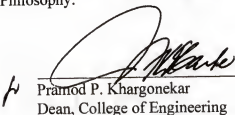
I certify that I have read this study and that in my opinion it conforms to acceptable standards of scholarly presentation and is fully adequate, in scope and quality, as a dissertation for the degree of Doctor of Philosophy.



Paul H. DeHoff
Professor of Mechanical Engineering and
Engineering Science, University of
North Carolina at Charlotte

This dissertation was submitted to the Graduate Faculty of the College of Engineering and to the Graduate School and was accepted as partial fulfillment of the requirements for the degree of Doctor of Philosophy.

August 2001



Pramod P. Khargonekar
Dean, College of Engineering

Winfred M. Phillips
Dean, Graduate School